

THESIS

THE EFFECTS OF SCOUR ON THE FLOW FIELD AT A BENDWAY WEIR

Submitted by

Mason Garfield

Department of Civil and Environmental Engineering

In partial fulfillment of the requirements

For the Degree of Master of Science

Colorado State University

Fort Collins, Colorado

Summer 2019

Master's Committee:

Advisor: Robert Ettema

Christopher Thornton

Ellen Wohl

Copyright by Mason Garfield 2019

All Rights Reserved

ABSTRACT

THE EFFECTS OF SCOUR ON THE FLOW FIELD AT A BENDWAY WEIR

Bendway weirs (BW) are rock structures commonly used for controlling the thalweg location in alluvial channels, especially bends. Although there are many studies analyzing the effect of BWs on bend flow fields, there is little known about the effects of scour on the modified flow field. Many physical and numerical models of BWs use a fixed bed with the existing river bathymetry, assuming that the effects of scour are negligible. This study analyzed the effects of the scour on the flow field using SRH-2D, a 2-dimensional numerical model solving the full St. Venant equation (also termed the dynamic wave equation). In addition, the study used small scale and large scale hydraulic models and a 3-dimensional numerical model, FLOW-3D, to validate and calibrate the 2-D model. Using FLOW-3D, the 3-dimensional flow field was used to identify areas where SRH-2D was accurate and where it was lacking. The small scale hydraulic model was used to determine the effect of streamwise blockage on scour using plates.

Results from the small scale hydraulic model indicate that when the degree of streamwise blockage (L/B where L is the width of the plate and B is the width of the flume) and submergence (Y/H where Y is the flow depth and H is the height of the plate) remained the same, but the acute angle to the flume wall varied (α), the maximum scour depth did not change significantly. Accordingly, the scour morphology from the tests with $\alpha = 90^\circ$ could be applied to tests with $\alpha = 30^\circ$ and 60° using the 2-D model. When comparing the flow field using SRH-2D to FLOW-3D, it was found that the maximum depth-averaged velocity was closer to FLOW-

3D's when $Y/H = 1.25$ than when $Y/H = 2.0$. This finding likely results from the greater effect of blockage directing the flow around the BW than the deeper case, where the flow has a higher vertical velocity over the top of the BW. The 2-D model cannot take this into account, leading to error.

The pre- and post-scour maximum velocity magnitude and locations were compared to determine the effect of scour on the flow field using the 2-D model. A deep flow depth ($Y/H = 2.0$) and a shallower flow depth ($Y/H = 1.25$) were run for different BW orientations, ($\alpha = 30^\circ$, 60° , and 90°) to determine the applicability of the effect of scour on the flow field. The analysis found that, when $Y/H = 2.0$, the difference in the maximum velocity magnitude and location between pre-and post-scour were fairly negligible for all orientations, whereas when $Y/H = 1.25$, the effects of the scour on the flow field were more prominent. Overall it was found that the scour morphology is important to take into consideration for a fixed bed numerical or physical model when analyzing flow depths slightly overtopping the BW, but has little effect when the flow is twice the size of the BW.

ACKNOWLEDGEMENTS

First and foremost I thank my advisor, Dr. Robert Ettema for his guidance and support throughout my studies at CSU. His tireless effort with this project has been greatly appreciated. I would also like to thank my other committee members, Dr. Christopher Thornton and Dr. Ellen Wohl for contributing their time and expertise.

I also thank all of my colleagues at the Engineering Research Center, and especially Taylor Hogan and Seth Seifken for their support throughout my research. I also thank my colleagues at Ayres Associates for their encouragement and knowledge which has helped me in my studies.

I thank my mom and dad for their immeasurable support throughout my graduate studies at CSU and throughout my career.

Lastly I thank my aunt, uncle, and cousins because without them I never would have made it to Colorado.

TABLE OF CONTENTS

ABSTRACT.....	ii
ACKNOWLEDGEMENTS.....	iv
LIST OF TABLES.....	vii
LIST OF FIGURES.....	ix
CHAPTER 1. INTRODUCTION & OBJECTIVES	1
1.1 Introduction.....	1
1.2 Objectives.....	2
CHAPTER 2. BACKGROUND.....	3
2.1 Flow Field and its Effects on Scour	3
2.2 Degree of Streamwise Blockage	6
2.3 BW Submergence.....	8
2.4 Effects of scour on the flow field.....	8
2.5. 2-Dimensional Modeling.....	9
2.6. 3-Dimensional Modeling.....	11
CHAPTER 3. METHODS	13
3.1. Large Flume	13
3.1.1 Processing of LiDAR.....	20
3.1.2 Scour Hole Geometry	20
3.2 Small Flume	21
3.2.1 Flume Layout.....	22
3.2.2 Plates Used in Study	24
3.2.3 Sand Used in Study.....	24
3.2.4 Small Flume Experimental Procedure.....	30
3.3. SRH-2D.....	32
3.3.1 Assumptions/Simplifications.....	32
3.3.2 Model Setup.....	32
3.2.3 Boundary Conditions.....	33
3.2.4 Boundary Sensitivity Analysis	33
3.2.5 Manning’s n Sensitivity Analysis.....	36
3.2.6 Mesh Setup	38
3.2.7 Mesh Sizing	40
3.2.8 Time Step.....	43
3.2.9 Convergence/Accuracy of Model.....	45
3.2.10 Turbulence model.....	45
3.2.11 Use of smooth BW	49
3.4 Flow 3D.....	51
3.4.1 Model Setup.....	51
3.4.2 Mesh Independence	53
3.5 Experimental Program.....	54
CHAPTER 4: RESULTS & ANALYSIS	57
4.1 Small Scale Flume.....	57
4.1.1 Effects of Degree of Streamwise Blockage on the Flow Field and Scour	57

4.1.2 Effects of a flood hydrograph on a BW's stability	60
4.1.3 Discussion of Plate Experiments	61
4.2 Flow 3-D	62
4.2.1 Comparison of FLOW-3D Results to the Hydraulic Model.....	62
4.2.2 Comparison of FLOW-3D Depth Average Velocity to SRH-2D Depth Average Velocity	65
4.2.2 Vertical Velocity Component.....	71
4.3 Effects of Scour on Flow Parameters when $\alpha = 30^\circ, 60^\circ,$ and 90°	72
4.3.1 Effect of Scour on Velocity Field when $Y/H = 1.25$ and $2.0, \alpha = 30^\circ$	74
4.3.2 Effect of Scour on Maximum Velocity when $Y/H = 1.25$ and $2.0, \alpha = 30^\circ$	82
4.3.3 Effect of Scour on Unit Discharge when $Y/H = 1.25$ and $2.0, \alpha = 30^\circ$	84
4.3.4 Effect of Scour on Velocity Field when $Y/H = 1.25$ and $2.0, \alpha = 60^\circ$	86
4.3.5 Effect of Scour on Maximum Velocity when $Y/H = 1.25$ and $2.0, \alpha = 60^\circ$	94
4.3.6 Effect of Scour on Unit Discharge when $Y/H = 1.25$ and $2.0, \alpha = 60^\circ$	96
4.3.7 Effect of Scour on Velocity Field when $Y/H = 1.25$ and $2.0, \alpha = 90^\circ$	98
4.3.8 Effects of Scour on the Maximum Velocity when $Y/H = 1.25$ and $2.0, \alpha = 90^\circ$	106
4.3.9 Effect of Scour on Unit Discharge when $Y/H = 1.25$ and $2.0, \alpha = 90^\circ$	108
4.3.10 Discussion of Scour Effects on Velocity Field.....	110
4.3.11 Sources of Error.....	113
CHAPTER 5. CONCLUSIONS AND RECOMMENDATIONS	114
5.1 Conclusions	114
5.2 Recommendations	116
REFERENCES	118
APPENDIX A. VELOCITY VECTORS.....	123
APPENDIX B. UNIT DISCHARGE.....	129

LIST OF TABLES

Table 1. Calculated data used to determine the flow values for $Y/H=1.25$ (a) and $Y/H=2$ (b)	29
Table 2. RMSE between the large-scale flume depth average velocity data and FLOW-3D depth average velocity data for fine, medium, and coarse size mesh when $Y/H = 1.25$ and 2.0	40
Table 3. The RMSE comparing parabolic to the $k - \epsilon$ turbulence model for $Y/H = 1.25$ and 2.0	45
Table 4. The RMSE comparing $Ct = 0.3$ to $Ct = 0.9$ for $Y/H = 1.25$ and 2.0	48
Table 5. The RMSE between the velocity magnitudes of Flow-3D and the large scale flume (RMSE _L) at the locations indicated in Fig. 36	54
Table 6. The experimental program of the physical and numerical models. Note that in the Test ID, (2) denotes the use of the 2-dimensional numerical model, (3) denotes the use of the 3-dimensional numerical model, (L) denotes the use of the large scale flume, and (S) denotes the use of the small flume	56
Table 7. The average velocity percent difference between pre-scour and post-scour at sub-cross sections, indicated in Fig. 49 when $Y/H = 1.25$ (a positive difference indicates a decrease between pre-scour and post scour conditions and vice versa)	80
Table 8. The average velocity percent difference between pre-scour and post-scour at sub-cross sections, indicated in Fig. 49 when $Y/H = 2.0$ (a positive difference indicates a decrease between pre-scour and post scour conditions and vice versa)	80
Table 9. The average unit discharge percent difference between pre- and post-scour conditions at sub-cross sections indicated in Fig. 49 when $Y/H = 1.25$ (a positive difference indicates a decrease between pre-scour and post scour conditions and vice versa)	85
Table 10. The average unit discharge percent difference between pre- and post-scour conditions at sub-cross sections indicated in Fig. 49 when $Y/H = 1.25$ (a positive difference indicates a decrease between pre-scour and post scour conditions and vice versa)	86
Table 11. The average velocity percent difference between pre- and post-scour at sub-cross sections with locations indicated in Fig. 55 conditions when $Y/H = 1.25$ (a positive difference indicates a decrease between pre-scour and post scour conditions and vice versa)	92
Table 12. The average velocity percent difference between pre- and post-scour at sub-cross sections with locations indicated in Fig. 55 conditions when $Y/H = 2.0$ (a positive difference indicates a decrease between pre-scour and post scour conditions and vice versa)	92
Table 13. The average unit discharge percent difference between pre-scour and post-scour conditions at sub-cross sections with locations indicated in Fig. 55 when $Y/H = 1.25$ (a positive difference indicates a decrease between pre-scour and post scour conditions and vice versa)	98
Table 14. The average unit discharge percent difference between pre-scour and post-scour conditions at sub-cross sections with locations indicated in Fig. 55 when $Y/H = 2.0$ (a positive difference indicates a decrease between pre-scour and post scour conditions and vice versa)	98

Table 15. The average velocity percent difference between the pre- and post-scour conditions at sub-cross sections indicated in Fig. 61 when $Y/H = 1.25$ (a positive increase indicates the decrease in post-scour conditions and vice versa)	104
Table 16. The average velocity percent difference between the pre- and post-scour conditions at sub-cross sections indicated in Fig. 61 when $Y/H = 2.0$ (a positive increase indicates the decrease in post-scour conditions and vice versa).....	104
Table 17. The average unit discharge percent difference between the pre- and post-scour conditions at sub-cross sections indicated in Fig. 61 when $Y/H = 1.25$ (a positive increase indicates the decrease in post-scour conditions and vice versa).....	109
Table 18. The average unit discharge percent difference between the pre- and post-scour conditions at sub-cross sections indicated in Fig. 61 when $Y/H = 2.0$ (a positive increase indicates the decrease in post-scour conditions and vice versa).....	110
Table 19. The percent difference in average velocity across the sub cross sections between the pre-scour and post scour when $Y/H = 1.25$ for $\alpha = 30^\circ, 60^\circ,$ and 90°	111
Table 20. Summary of the percent difference in average velocity across the sub cross sections when $Y/H = 2.0$ for $\alpha = 30^\circ, 60^\circ,$ and 90°	111
Table 21. Summary of the difference in unit discharge between the pre- and post-scour conditions across the sub cross sections for $Y/H = 1.25$ when $\alpha = 30^\circ, 60^\circ,$ and 90° (a positive difference indicates that the pre-scour was larger and vice versa)	111
Table 22. Summary of the difference in unit discharge between the pre- and post-scour conditions across the sub cross sections for $Y/H = 2.0$ when $\alpha = 30^\circ, 60^\circ,$ and 90° (a positive difference indicates that the pre-scour was larger and vice versa)	112
Table 23. The percent difference in maximum velocity (V_{max}), maximum velocity lateral distance from the crest (Y_{max}), and maximum velocity stream wise distance from the crest (X_{max}) between the pre- and post-scour when $Y/H = 1.25$ (a positive value indicates pre-scour was larger and vice versa).....	113
Table 24. The percent difference in maximum velocity (V_{max}), maximum velocity lateral distance from the crest (Y_{max}), and maximum velocity stream wise distance from the crest (X_{max}) between the pre- and post-scour when $Y/H = 2.0$ (a positive value indicates that pre-scour was larger and vice versa)	113

LIST OF FIGURES

Fig. 1. The flow microstructures surrounding an abutment (Kwan 1984).....	4
Fig. 2. The complicated flow around spill-through abutments, displaying the regions of scour (Ettema et al. 2010).....	4
Fig. 3. The equilibrium scour hole bathymetry for rock barbs under different submergence conditions, with SB1 being unsubmerged and SB2 to SB7 were submerged and increasing in flow depth, where the white square indicates the location of maximum scour (Papanicolaou et al. 2018)	6
Fig. 4. Maximum scour depth versus abutment alignment, β , for the exposed wing-wall column, pictured right, from Ettema et al.'s (2010) study.....	8
Fig. 5. The plan layout of CSU's Tarbela (Large) flume.....	13
Fig. 6. Plan and front view of the BW within the sand pit in the flume	14
Fig. 7. The sieve analysis of the material used in the sand recess depicted in Fig. 5	15
Fig. 8. Topcon-TLS LiDAR with operator, scanning flume bed and BW before experiments....	19
Fig. 9. A closer-up view of the BW being assembled in the flume. As noted above, the average diameter of the rock used to form the BW was 0.15 m (6 in).....	19
Fig. 10. The BW during the Y/H=1.25 test, slowly filling up the flume.....	20
Fig. 11. The scour morphology of the sand bed, obtained from the $\alpha = 90^\circ$ tests LiDAR data when: (a) Y/H = 1.25 and (b) Y/H = 2.0. The blue line indicates the region where the scour occurred.....	21
Fig. 12. The 8in-wide (0.20m) flume used for the study	23
Fig. 13. Horizontal baffles installed at the flume inlet to ensure fully developed flow within the flume	23
Fig. 14. The rocks added just downstream of the baffles	24
Fig. 15. The flume with a sand bed.....	25
Fig. 16. Example of a plate test in progress	31
Fig. 17. The point gage used to measure the scour depths	31
Fig. 18. The locations of the cross sections where the velocity from the extended inlet and outlet were compared to the original inlet and outlet.....	34
Fig. 19. Comparing velocity and depth after extending the upstream and downstream boundary conditions by about 40 m when Y/H = 1.25 at the maximum velocity cross section depicted in Fig. 18	35
Fig. 20. Comparing velocity and depth after extending the upstream and downstream boundary conditions by about 40 m when Y/H = 2.0 at the maximum velocity cross section depicted in Fig. 18.....	35
Fig. 21. The locations of the comparison between the hydraulic model and SRH-2D depth-average velocity for: (a) Y/H = 1.25 and (b) Y/H = 2.0	37

Fig. 22. The general cross section locations where the 2-D model was compared to the 3-D model for $Y/H = 1.25$ and 2.0 , $\alpha = 90^\circ$	37
Fig. 23. The Manning's n values assign to the sand, BW, concrete bottom, and walls for $Y/H = 1.25$ and 2.0 . Note that "s" indicates the shallow flow ($Y/H = 1.25$) and "d" indicates the deeper flow ($Y/H = 2.0$)	38
Fig. 24. Example mesh. Note the fine mesh used in the contracted section where the velocity is greatest	39
Fig. 25. Mesh elevation versus the LiDAR elevation at the Crest cross section when $Y/H = 1.25$	41
Fig. 26. Mesh elevation versus the LiDAR elevation at the Scour Hole cross section when $Y/H = 1.25$	41
Fig. 27. Mesh elevation versus the LiDAR elevation at the Crest cross section when $Y/H = 2.0$	42
Fig. 28. Mesh elevation versus the LiDAR elevation at the Scour Hole cross section when $Y/H = 2.0$	42
Fig. 29. The velocity vectors when $Y/H = 1.25$: (a) fine mesh size and (b) medium mesh size. The red arrows indicate the center of the eddy from the crest of the BW	43
Fig. 30. The location of the points (blue dots) in the wake of the BW where FLOW-3D DAV was compared to SRH-2D DAV using the $k-\epsilon$ and parabolic turbulence models	46
Fig. 31. The velocity vectors when $Y/H = 1.25$: (a) parabolic turbulence model; (b) $k - \epsilon$ turbulence model.....	47
Fig. 32. The velocity vectors when $Y/H = 1.25$ using the parabolic turbulence model: (a) $Ct = 0.3$; (b) $Ct = 0.9$	48
Fig. 33. Comparison of velocity and depth of smooth BW (created in AutoCAD) vs rough (actual) BW when $Y/H = 2.0$ at the "crest" cross-section	50
Fig. 34. Comparison of velocity and depth of smooth BW (created in AutoCAD) vs rough (actual) BW when $Y/H = 1.25$ at the "crest" cross-section	50
Fig. 35. The roughness values, k_s used in the large flume for FLOW-3D.....	52
Fig. 36. The locations (in plan view), indicated by the black dots where the large scale flume velocity magnitude data was compared to the velocity magnitude found in FLOW-3D. Note that the velocity was taken at multiple depths	54
Fig. 37. The scour depth at each plate (BW) for varying orientation when $Y/H = 1.25$ and 2.0 . The bed thickness was 0.10 m (0.33 ft)	58
Fig. 38. Overhead views of scour at the plates used to simulate (approximately) bendway weirs: (a) $Y/H = 1.25$, $\alpha = 30^\circ$; (b) $Y/H = 2.0$, $\alpha = 30^\circ$; (c) $Y/H = 1.25$, $\alpha = 60^\circ$; (d) $Y/H = 2.0$, $\alpha = 60^\circ$; (e) $Y/H = 1.25$, $\alpha = 90^\circ$; and, (f) $Y/H = 2.0$, $\alpha = 90^\circ$. The black sand is magnetite (denser and finer than the main sand), and indicator of locations of greater shear stress on the bed	60
Fig. 39. Shown here is the time development of scour at a plate ($\alpha = 90^\circ$) as the flow stage increased from essentially a baseflow state to a deeper flow associated with the rising limb of a flow hydrograph.....	61

Fig. 40. The location of ADV velocity data that was compared to FLOW-3D velocity magnitude at multiple depth per point at: (a) $Y/H = 1.25$ and (b) $Y/H = 2.0$	63
Fig. 41. Comparison of FLOW-3D velocity magnitude to the velocity magnitude of the physical model data: (a) $Y/H = 1.25, \alpha = 90^\circ$; and, (b) $Y/H = 2.0, \alpha = 90^\circ$. Here, “Crest” and “D/S Crest” indicates the streamwise location of the comparison as indicated in Fig. 40	64
Fig. 42. The flume layout used in the 2D and 3D numerical models, and for the large flume. Indicated are the flow direction, the locations of the left and right walls and the BW. The transects labeled “Crest,” “Calibration Points,” “Scour Hole,” and “Max Velocity” are the locations of comparison of difference between 3-D and 2-D numerical models and the physical model.....	67
Fig. 43. Flow lines (with velocity contours) at and below the water surface using FLOW-3D: (a) $Y/H = 1.25, \alpha = 90^\circ$; and, (b) $Y/H = 2, \alpha = 90^\circ$	68
Fig. 44. FLOW-3D generated velocity vectors in profile view (over vertical plane) at the downstream end of the BW: (a) $Y/H = 1.25, \alpha = 90^\circ$; and, (b) $Y/H = 2, \alpha = 90^\circ$	69
Fig. 45. Comparison of FLOW-3D depth-averaged velocity to SRH-2D depth averaged velocity with “BW” indicating the lateral location of the BW, “calibration points” indicating the location of where SRH-2D depth-averaged velocity was calibrated, “scour hole” indicating the velocity cross section at the max depth of the scour hole, “max velocity” indicating the velocity cross section across the maximum velocity, and “crest” indicating the velocity across the crest: (a) $Y/H = 1.25, \alpha = 90^\circ$; and, (b) $Y/H = 2, \alpha = 90^\circ$	70
Fig. 46. The locations of the maximum depth averaged velocities from SRH-2D and FLOW-3D: (a) $Y/H = 1.25, \alpha = 90^\circ$; and, (b) $Y/H = 2.0, \alpha = 90^\circ$	71
Fig. 47. Equally distributed streamlines with z-velocity contours when $\alpha = 90^\circ$: (a) $Y/H = 1.25$ and (b) $Y/H = 2.0$. Note the larger velocity upstream of the crest, indicated with the red oval and relatedly, the wider spacing of the streamlines between $Y/H = 1.25$ than $Y/H = 2.0$	72
Fig. 48. A schematic of the flow around the BW, where the vena contracta indicates the region of maximum velocity. Note that this schematic doesn’t account for the turbulence in the wake of the BW	74
Fig. 49. The approximate locations of the cross sections where data was collected when $Y/H = 1.25$ and 2.0 . Shown here are the positions of the four cross-sections along which velocity and unit discharge distributions were determined	77
Fig. 50. Velocity distribution when $Y/H = 1.25$ experiment along the four cross-sections indicated in Fig. 49: (a) pre-scour; and; (b) post-scour. Notes: the cross-section labelled “Upstream of BW” is the “Section upstream of BW” cross-section; “Crest” is the “BW crest” cross-section, “BW” is the “BW center” cross-section; “max velocity” refers to the “max-velocity section” cross-section; and, “scour” refers to the “scour-hole section” cross-section in Fig. 49	78
Fig. 51. Velocity magnitude distribution when $Y/H = 2.0$ along the four cross-sections indicated in Fig. 49: (a) pre-scour; and; (b) post-scour	79

Fig. 52. Depth-average velocity magnitude difference between the pre-scour and post-scour conditions for: (a) $Y/H = 1.25$; and; (b) $Y/H = 2.0$. Red (positive) indicates a decrease between pre- and post-scour and blue (negative) indicates an increase between pre- and post-scour	81
Fig. 53. The location (X_{max} and Y_{max}) and magnitude of the maximum velocity (V_{max}) for $Y/H = 1.25$; (a) pre-scour, (b) post-scour	83
Fig. 54. The location (X_{max} and Y_{max}) and magnitude of the maximum velocity (V_{max}) for $Y/H = 2.0$; (a) pre-scour, (b) post-scour	84
Fig. 55. The approximate locations of the cross sections where data were collected when $Y/H = 1.25$ and 2.0 . Shown here are the positions of the four cross-sections along which velocity and unit discharge distributions were determined	89
Fig. 56. Depth average velocity distribution when $Y/H = 1.25$ along the four cross-sections indicated in Fig. 55: (a) pre-scour; and; (b) post-scour	90
Fig. 57. Depth average velocity distribution when $Y/H = 2.0$ along the four cross-sections indicated in Fig. 55: (a) pre-scour; and; (b) post-scour	91
Fig. 58. Depth-average velocity magnitude difference between the pre-scour and post-scour conditions for: (a) $Y/H = 1.25$; and; (b) $Y/H = 2.0$. Red (positive) indicates a decrease between pre- and post-scour and blue (negative) indicates an increase between pre- and post-scour	93
Fig. 59. The location (X_{max} and Y_{max}) and magnitude of the maximum velocity (V_{max}) for $Y/H = 1.25$; (a) pre-scour, (b) post-scour	95
Fig. 60. The location (X_{max} and Y_{max}) and magnitude of the maximum velocity (V_{max}) for $Y/H = 2.0$; (a) pre-scour, (b) post-scour	96
Fig. 61. The approximate locations of the cross sections where data was collected when $Y/H = 1.25$ and 2.0 . Shown here are the positions of the four cross-sections along which velocity and unit discharge distributions were determined	101
Fig. 62. Depth average velocity distribution when $Y/H = 1.25$ along the four cross-sections indicated in Fig. 61: (a) pre-scour; and; (b) post-scour	102
Fig. 63. Depth average velocity distribution when $Y/H = 2.0$ along the four cross-sections indicated in Fig. 61: (a) pre-scour; and; (b) post-scour	103
Fig. 64. Depth-average velocity magnitude difference between the pre-scour and post-scour conditions for: (a) $Y/H = 1.25$; and; (b) $Y/H = 2.0$. Red (positive) indicates a decrease between pre- and post-scour and blue (negative) indicates an increase between pre- and post-scour	105
Fig. 65. The location (X_{max} and Y_{max}) and magnitude of the maximum velocity (V_{max}) for $Y/H = 1.25$; (a) pre-scour, (b) post-scour	107
Fig. 66. The location (X_{max} and Y_{max}) and magnitude of the maximum velocity (V_{max}) for $Y/H = 2.0$; (a) pre-scour, (b) post-scour	108
Fig. 67. Plan views of depth-averaged velocity vectors, $Y/H = 1.25$, $Q = 87\text{cfs}$ and $\alpha = 90^\circ$: (a) pre-scour; and, (b) post-scour	123
Fig. 68. Plan views of depth-averaged velocity vectors, $Y/H = 2.0$, $Q = 128\text{cfs}$, and $\alpha = 90^\circ$: (a) pre-scour; and, (b) post-scour	124

Fig. 69. Plan views of depth-averaged velocity vectors, $Y/H = 1.25$, $Q = 87\text{cfs}$, 128cfs , and $\alpha = 60^\circ$: (a) pre-scour; and, (b) post-scour	125
Fig. 70. Plan views of depth-averaged velocity vectors, $Y/H = 2.0$, $Q = 128\text{cfs}$, and $\alpha = 60^\circ$: (a) pre-scour; and, (b) post-scour	126
Fig. 71. Plan views of depth-averaged velocity vectors, $Y/H = 1.25$, $Q = 128\text{cfs}$, and $\alpha = 90^\circ$: (a) pre-scour; and, (b) post-scour	127
Fig. 72. Plan views of depth-averaged velocity vectors, $Y/H = 2.0$, $Q = 128\text{cfs}$, and $\alpha = 90^\circ$: (a) pre-scour; and, (b) post-scour	128
Fig. 73. Unit discharge distribution when $Y/H = 1.25$ and $\alpha = 30^\circ$ along the four cross-sections indicated in Fig. 49: (a) pre-scour; and; (b) post-scour	129
Fig. 74. Unit discharge distribution when $Y/H = 2.0$ and $\alpha = 30^\circ$ along the four cross-sections indicated in Fig. 49: (a) pre-scour; and; (b) post-scour	130
Fig. 75. Unit discharge distribution when $Y/H = 1.25$ and $\alpha = 60^\circ$ along the four cross-sections indicated in Fig. 55: (a) pre-scour; and; (b) post-scour	130
Fig. 76. Unit discharge distribution when $Y/H = 2.0$ and $\alpha = 60^\circ$ along the four cross-sections indicated in in Fig. 55: (a) pre-scour; and; (b) post-scour	130
Fig. 77. Unit discharge distribution when $Y/H = 1.25$ and $\alpha = 90^\circ$ along the four cross-sections indicated in Fig. 61: (a) pre-scour; and; (b) post-scour	130
Fig. 78. Unit discharge distribution when $Y/H = 2.0$ and $\alpha = 90^\circ$ along the four cross-sections indicated in Fig. 61: (a) pre-scour; and; (b) post-scour	130

CHAPTER 1. INTRODUCTION & OBJECTIVES

1.1 Introduction

Bendway weirs (BW) are rock structures whose crests typically are well below the water surface associated with bankfull flow in an alluvial channel bend and project upstream into the approach flow. BWs were originally developed to disrupt the effects of secondary currents in channel bends, and to push the channel thalweg away from the channel's outer bank, thereby aiding towboat navigation along river channels. More recently, they have been used for bank-protection purposes due to the decreased velocities that may occur between BWs and because BW visibility is reduced during bank-full flows. By reducing flow velocities along the outerbank, it is anticipated that BWs should reduce the erosion of the outer bank. In addition to preventing bank erosion, the BWs can provide a habitat for benthic organisms within the rocks of the structure and in the wake of the BW where deposition of organic material can provide a food source (Kinzli & Thornton, 2010).

Whereas previous hydraulic and numerical models of BWs have used rigid-bed conditions, this study evaluates the extent to which scour of the alluvial bed at a BW affects the flow field at a single BW and, therefore, how scour will influence BW performance in modifying flow conditions. This study is the first investigation of this issue.

Although it is known that the flow field around a BW is 3-dimensional (3D), 2-dimensional (2-D, depth-averaged flow) models are quite often used to simulate flow in alluvial channels; e.g., at bridge waterways. However, relatively little is known about the reliability of 2-D models used in this regard. What is known is that the flow field at a BW is highly 3D. Not only are there lateral eddies due to the lateral contraction, but there also are vertical eddies due to

the flow overtopping a BW. These eddies complicate the flow field (e.g. Abad et al. 2008).

1.2 Objectives

This study had the following objectives:

1. Determine how scour influences the flow field at single BW. This objective involved the use of a 2-D (depth-averaged flow) numerical model (SRH-2D) to simulate flow around a single BW set at three orientations (30°, 60° and 90°) on a flat bed and then on a bed adjusted for scour around a BW;
2. In support of Objective 1, determine whether and how BW orientation influences scour depth and morphology. This objective entailed laboratory flume experiments done with a small-scale flume;
3. Show, in a preliminary manner, how the rising or dropping stage of a flow hydrograph may affect scour development at a BW. This objective involved conducting a demonstration experiment using a small flume and a simplified (flat plate) version of a BW; and,
4. Ascertain the error associated with using a 2-D model to obtain velocity data in comparison with velocity data obtained using a 3D model. This objective involved using a 3-D model (FLOW-3D) to illuminate areas where the flow around a BW is likely to differ from the flow field indicated using SRH-2D.

CHAPTER 2. BACKGROUND

2.1 Flow Field and its Effects on Scour

In recent years, the complexities of the flow field at rock structures like BWs have been studied using numerical and hydraulic models. It is common knowledge (Julien & Duncan 2003, Abad et al. 2008, and Kinzli and Thornton 2010) that BW presence modifies the flow field in a channel bend. A BW does so by disrupting the high velocity region of flow near the outer bank and the helical motion of flow around the bend (e.g., Abad et al. 2008). The pattern and strength of the helical motion varies with flow conditions, but in general the presence of BWs breaks this flow pattern into two opposite direction zones, where the original helical motion is counteracted or disrupted by BW presence (Julien & Duncan 2003). As this study focuses on the flow field at a single BW, it is to be understood that, using a 2-D numerical model (SRH-2D), some of the complexity of the flow field around a BW will not be replicated.

Flow around abutments, a structure somewhat akin to a BW, has been extensively studied due to their importance to stability of a bridge waterway. Therefore, some useful insight is to be gained from abutment studies. Although abutments usually are not overtopped (unlike flow at a BW), the flow field at an abutment is similar to the BW's. The full, 3-dimensional flow field is comprised of the main core flow (of contracted flow), the wake region, and the shear layer region. The turbulent structures within these flow regions is the back eddy, primary vortex, secondary vortices and wake vortices as Fig. 1 depicts (Kwan 1984). SRH-2D, being a depth-averaged model, does not simulate the primary vortex and secondary vortices Fig. 1 shows. However, major eddies and parts of the wake vortices associated with flow separation from a

boundary can be simulated using SRH-2D, because they are persistent, recirculating flow features.

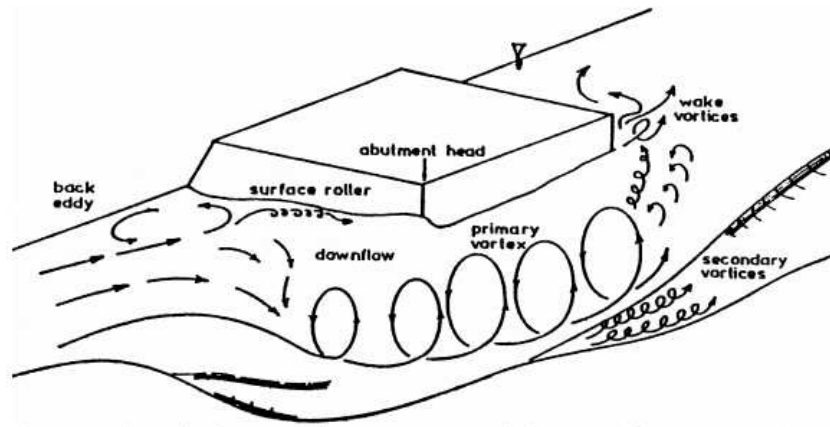


Fig. 1. The flow microstructures surrounding an abutment (Kwan 1984)

The turbulent flow structures will influence the region(s) of scour surrounding the flow field as Fig. 2 depicts. For example the turbulent structures within the flow field can cause scour at the corners of the abutments (Ettema et al. 2010).

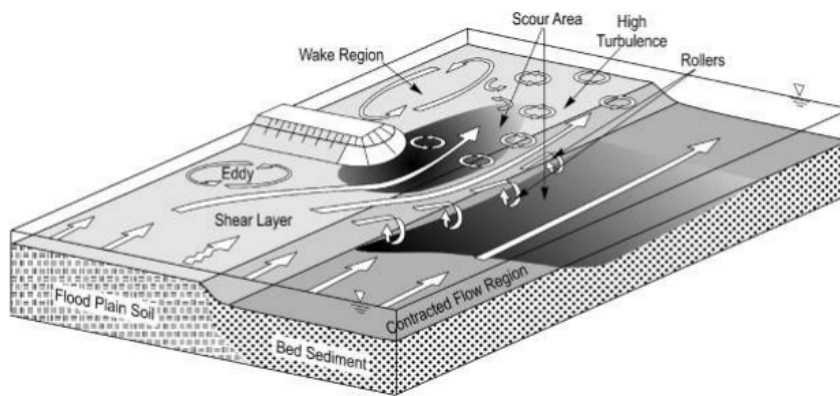


Fig. 2. The complicated flow around spill-through abutments, displaying the regions of scour (Ettema et al. 2010)

When the rock structures are overtopped (i.e., BW, rock vane, barb), the flow field becomes more complex than that for the typical abutment. Jia et al. (2009), for example, found that an overtopped BW creates a high pressure zone in the front of the BW and a low pressure zone in its wake, thus slowing and dividing the approaching flow, and forcing more flow towards

the tips of the BW and increasing the velocity of flow around a BW tip. When a BW is angled upstream, the low pressure zone is located closer to the outer bank and the high pressure zone is located toward the inner bank, or the tip of the weir so now the over topping flow is pushed towards the inner bank (Jia et al. 2009).

Although greatest scour occurs close to the tip of a rock structure like BWs, Papanicolaou et al. (2018) and others have found that even when a barb was fully submerged, the maximum velocity did not occur at the barb tip, but rather slightly downstream of it. Their data are from an analysis of the scour around barbs or slope crested structures (Fig. 3) using experimental data and a large eddy simulation (LES) turbulence model. Their analysis indicates that scour occurs mainly due to the vortices close to the bed, and is controlled by the primary vortex, similar to scour at abutments, rather than the maximum velocity (Fig. 1).

The large eddy simulation (LES) results obtained by Papanicolaou et al. (2018) indicate four main vortices before and after scouring including the primary vortex upstream of the bar, the corner vortex close to the barb and the lateral flume wall, a detached shear layer on top of the crest of the barb, and a trailing vortex behind the downstream end of the barb. The primary vortex and corner vortex are common flow features near lateral structures in streams and are caused by the flow separation at the barb (Bressan et al 2011; Koken 2011; Koken & Constantinescu 2008; and Teruzzi et al 2009). Although the primary vortex starts upstream of the barb, it eventually wraps around the tip and extends downstream. The LES results showed that the mechanism which drives scouring of gravel around the fully submerged barb is driven by the fluid energy from the contraction, transferring to the primary vortex and scours the bed through the secondary vortices over time. This is the same process as observed for unsubmerged structures, as Kwan (1984) suggested. Jamieson et al. (2011), who measured 3-dimensional flow

around a wing dike installed in the Missouri River, also found a relationship between the vertically oriented vortex cores and local scour. Therefore, this study likely will see scour in front of and behind the simulated BW, and the maximum velocity will be a relatively short distance downstream of the tip.

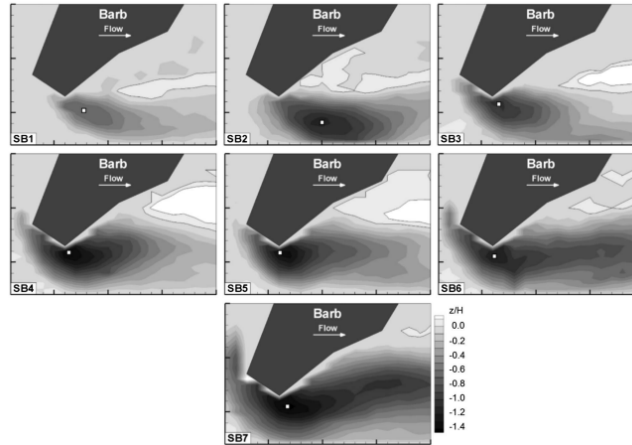


Fig. 3. The equilibrium scour hole bathymetry for rock barbs under different submergence conditions, with SB1 being unsubmerged and SB2 to SB7 were submerged and increasing in flow depth, where the white square indicates the location of maximum scour (Papanicolaou et al. 2018)

The maximum velocity found within the contraction may occur primarily under lower stages. Abad et al. (2008) found that the increase in surface velocity in the wake of the BWs becomes much higher under bankfull stage and the maximum velocity in the channel shifts outward toward the outer bank. Therefore, under larger flows the BW become less effective, due to the decreased influence of the BW on the flow and the channel with BWs will act closer to a channel without them. It is likely that within this study, under the deeper flow depth condition ($Y/H = 2.0$), the scour will have a lesser effect on the flow field of the BW than the shallower flow depth ($Y/H = 1.25$), which is a less prevalent feature than the BW.

2.2 Degree of Streamwise Blockage

The degree of streamwise blockage (L/B) for a given flow depth, where L is the projected length of the BW and B is the flume width, has been shown to affect the maximum scour depth (Ettema et al. 2010; Hemmati et al. 2016). It can be assumed that the mechanisms driving the

scour around a submerged rock structure are similar to those driving the scour around abutments, as indeed Papanicolaou et al. (2018) suggest. Therefore, the testing conducted with exposed pile supported wing wall abutments conducted by Ettema et al., (2010), which found that the orientation angle did not affect the maximum scour depth significantly (Fig. 4), should be able to be applied to this study to a certain extent. Due to the exposed piles, the flow field will change as compared to a wing-wall abutment without the exposed piles, so more investigation needs to be performed. Also abutment alignment did not appreciably affect the ratio of the maximum depth incorporating scour (Y_{\max}) to the critical flow depth where mobilization will occur (Y_c) for the range of abutment layouts investigated when there was scour of the main-channel bed. The variations in Y_{\max}/Y_c were well within the amplitude variation of a dune (Ettema et al., 2010).

Although many studies analyze the effects of the contraction ratio on the scour around abutments set at constant orientation angles (e.g., Ballio et al 2009; Sturm 2006; Sturm & Janjua 1994), few studies analyze the effects of structure orientation at a steady opening ratio (streamwise length of the structure to channel width (L/B)). Kuhnle et al. (2002) analyzed local scour at three different angles around spur dikes using two different contraction ratios, but focused more on the scour-related effects of spur-dike orientation angles using different flow rates on the scour. Although there is some relation between stream barbs that have the same degree of streamwise blockage (contraction ratio), but different orientation angles and the maximum scour depth and volume of scour, the flow rates and depths are not exactly the same. Another study by Hemmati et al. (2016) used contraction ratios of 0.2, 0.3, and 0.4 for rock barbs set at 60° , 75° , and 90° . For part of their study, they analyzed the effect of orientation angle as well as crest slope of the BW on the maximum scour depth, keeping the contraction ratio constant and found that there was not a large difference between the BW orientation angles, with

the same contraction ratio. However, their findings are not entirely clear and do not include shallower angles than 60° . Therefore, more investigation into the effects of the orientation angle holding the streamwise blockage constant will be presented in Section 4.1.

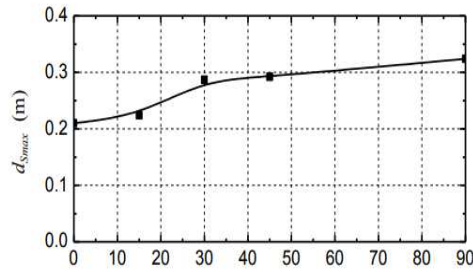


Fig. 4. Maximum scour depth versus abutment alignment, β , for the exposed wing-wall column, pictured right, from Ettema et al.'s (2010) study

2.3 BW Submergence

The term, $\frac{Y_0}{H}$, expresses the relative submergence of a BW, and has been used to characterize the influence flow depth, Y_0 , in terms of the crest height, H . This term has been used by Papanicolaou et al. 2018 in terms of approaching flow depth to barb crest height with values ranging from 0.98 to 2.53. They found that the submergence impacts time-average mean flow characteristics and turbulence structures around the barb and therefore the degree of submergence affects the maximum scour depth. Another study, (Abad et al. 2007) analyzed different flow stages over BWs and indicate how the velocity field changed, but did not discuss the effects of the submergence with and without scour. Therefore, the present study gives useful insights regarding scour effects on flow submergence.

2.4 Effects of scour on the flow field

Many studies have investigated the flow field around riverine rock structures under fixed and mobile bed conditions (e.g., Jia et al. 2009, Abad et al. 2008, Kinzli and Thornton 2009,

Papanicolaou et al. 2018), but little is known about how scour affects the flow field surrounding a BW. For example, Papanicolaou et al. (2018) investigated the scour around a slope crested structure on a gravel bed and how submergence affects the magnitude of scour. A fixed bed pre and post scour condition is investigated, but only for a submergence ratio of 2.53 (fully submerged). Consequently, none of these studies have included the effects of scour on the flow field.

The impact of scour is important because BWs are designed using the existing bed, but due to an increase in blockage, scour will occur, and could impact the results of the design. This study takes a first stab at determining the effects of scour on the flow field using a 2-D model.

2.5. 2-Dimensional Modeling

There are several two-dimensional (2-D) numerical models commonly used by engineering practitioners and researchers. The most common 2-D models used for river engineering determine the depth-averaged velocity in the downstream and transverse directions. These models perform quite well for reaches with large-aspect-ratio flows; i.e., where the depth is much smaller than the width and there is little velocity in the vertical direction. In these flow fields, the flow is distinctly 2-D, such as flows in large aspect-ratio channels marked by bends, islands and many hydraulic structures. For such flows, a 2-D model reflects the main flow variables, notably flow depth, water surface elevation, velocity, and bed-shear stress. A 2-dimensional model was chosen to compare pre-scour and post-scour conditions due to its short computation times and use in previous studies designing rock structures such as Elhakeem & Papanicolaou (2016), who designed and installed rock barbs using a 2-D model.

Because the study is analyzing flow around a BW, the 2-D model SRH-2D was chosen due to its use of the St. Venant Equations, which are based on the 2-D Dynamic Wave equations

(Lai 2009). The St. Venant equations were derived from the more general Navier Stokes equations, adapting the latter equations for describing shallow-water flow conditions, assuming that the flow is hydrostatic. The full St. Venant equations include the advective terms, which are important when a fluid contracts; meaning essentially that there is a large gradient of velocity within the downstream and transverse directions.

The following forms of the St. Venant equations are discretized for SRH-2D:

$$\frac{\partial h}{\partial t} + \frac{\partial hU}{\partial x} + \frac{\partial hU}{\partial x} = e \quad (2.1)$$

$$\frac{\partial hU}{\partial t} + \frac{\partial hUU}{\partial x} + \frac{\partial hVU}{\partial y} = \frac{\partial hT_{xx}}{\partial x} + \frac{\partial hT_{xy}}{\partial y} - gh \frac{\partial z}{\partial x} - \frac{\tau_{bx}}{\rho} + D_{xx} + D_{xy} \quad (2.2)$$

$$\frac{\partial hV}{\partial t} + \frac{\partial hUV}{\partial x} + \frac{\partial hVV}{\partial y} = \frac{\partial hT_{xy}}{\partial x} + \frac{\partial hT_{yy}}{\partial y} - gh \frac{\partial z}{\partial y} - \frac{\tau_{by}}{\rho} + D_{yx} + D_{yy} \quad (2.3)$$

Here, Eq. (2.1) expresses flow continuity; Eq. (2.2) is the depth-averaged momentum equation of flow in the x- direction; and, Eq. (2.3) is the depth-averaged momentum equation of flow in the y-direction. In the above equations, z is the water surface elevation, t is the time, U and V are the depth-averaged velocities in the x and y directions, respectively, T_{xx} , T_{xy} , and T_{yy} are depth-averaged turbulent stresses, D_{xx} , D_{xy} , D_{yx} , and D_{yy} are dispersion terms which arise from depth averaging, and τ_{bx} and τ_{by} are the bed shear stresses due to friction in the x and y directions, respectively (Lai 2009).

To solve the equations, the turbulence stresses are approximated using the following expressions:

$$T_{xx} = 2(\nu + \nu_t) \frac{\partial U}{\partial x} - \frac{2}{3} k \quad (2.4)$$

$$T_{xy} = (\nu + \nu_t) \left(\frac{\partial U}{\partial y} - \frac{\partial V}{\partial x} \right) \quad (2.5)$$

$$T_{xy} = (\nu + \nu_t) \left(\frac{\partial U}{\partial y} - \frac{\partial V}{\partial x} \right) \quad (2.6)$$

Here ν is the kinematic viscosity of the water, ν_t is turbulent eddy viscosity and k is turbulent kinematic energy. The depth-averaged zero equation parabolic turbulence model solves for flow's kinematic viscosity using;

$$\nu_t = C_t u_* h \quad (2.7)$$

Where C_t is a constant that ranges from 0.3 to 0.7, and u_* is the frictional velocity of flow.

The two equation, k-e turbulence model was also considered within this study.

Comparing it to the parabolic turbulence model found no significant difference as Section 3.3.11 explains. The parabolic model was chosen for the present study, as it was more convenient to use.

2.6. 3-Dimensional Modeling

The use of 3-dimensional (3-D) numerical models has become more common as computing times, and discretization techniques have improved. The commercial software FLOW-3D was selected as the 3-D numerical model, owing to its wide professional and academic use. Many in-stream structure studies have been performed using FLOW-3D (Scurlock et al. 2015, Abad et al. 2008, Schwartz et al. 2004) and, more specifically, it has been used for analysis in various BW studies (Scurlock et al. 2015 and Abad et al. 2008). FLOW-3D solves the 3-D nonhydrostatic Reynolds Averaged Navier-Stokes (RANS) equations using a finite volume or finite difference method to solve them in a fixed Eulerian rectangular grid (Flow Science 2005). Free surfaces are defined using the Volume of Fluid (VOF) method (Hirt & Nichols 1981) and complex geometries are modeled using the area/volume obstacle representation method (FAVOR) method (Hirt 1985). The FAVOR method is especially useful when there are abrupt

changes in geometry, allowing for easier computations, such as the presence of BWs (Scurlock et al 2015). The continuity and momentum equations of the fluid fraction are found using the FAVOR function, and the finite volume or finite difference method is used as the discretization technique to solve each equation (Fadaei-Kermani & Barani 2014). Advections are discretized using a first order explicit equation (Flow Science 2005).

The Renormalized Group (RNG), $k - \epsilon$ turbulence model was chosen with a compromise between computing time and accuracy (Scurlock et al. 2015) and due to its accuracy near walls and in flows with rapid distortions, such as in the wake of BWs (Yakhot & Smith 1992). The RNG model is considered more accurate than the normal $k - \epsilon$ model, where the ϵ equation is limited in flows with large rates of deformation (Versteeg & Malalasekera, 2007). The RNG $k - \epsilon$ model removes the effects of small scale turbulence by representing their effects in terms of larger scale motions and a modified viscosity (Versteeg & Malalasekera 2007). According to Scurlock et al. (2015) the RNG $k - \epsilon$ turbulence model produces acceptable agreement with flow field data from hydraulic models of bends with BWs.

CHAPTER 3. METHODS

This study's methods involved multiple approaches to gain insight into the effect of scour on the flow field. First, initial ADV and LiDAR data were obtained from CSU's large-scale flume. To investigate the effects of submergence on scour, a small flume was used to determine the maximum scour depth. Next, the velocity field from the 2D model was compared to that from the 3D model to determine the accuracy of the 2-D model. Once it was determined that the 2D model provided accurate results, the model was used to determine the effects of scour on the flow field.

3.1. Large Flume

The large 6.1 m (20 ft)-wide, 54.9 m (180 ft)-long flume (Fig. 5) at CSU's Engineering Research Center was used to test BWs oriented at 90 degrees for $Y/H = 1.25$ and 2.0 (Fig. 6). The BWs were formed of 0.2 m (6 in) rock and were 0.6 m (2 ft) tall so that multiple stacks of the rocks could be used. The side slopes of each BW were chosen to be 1.5H:1.0V, which was based on the submerged repose angle for the rocks used and is a typical value (Scurlock et al. 2012). With a larger weir side slope angle, higher local pressure and more vertical flow divide the approach flow, forcing more flow around the weir tip. Hence, by increasing the side slope angle to the submerged repose angle, the BW will be as effective as possible (Julien & Duncan 2003).

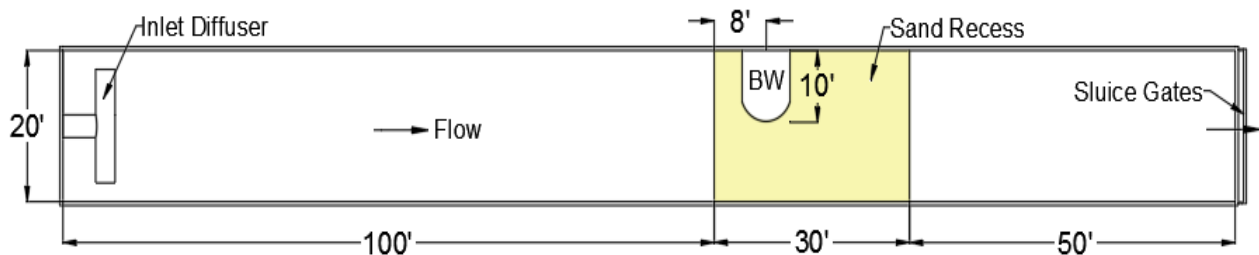


Fig. 5. The plan layout of CSU's Tarbela (Large) flume

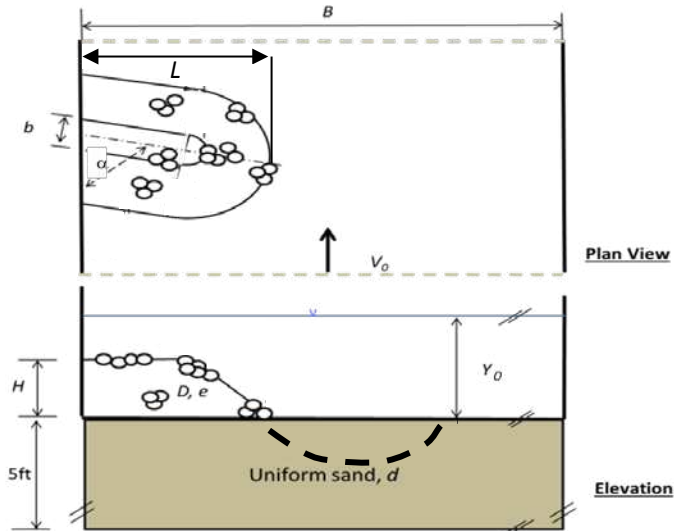


Fig. 6. Plan and front view of the BW within the sand pit in the flume. The dashed line indicates the post-scour condition

The BWs were chosen to have a contraction ratio, $L/B = 0.5$, to promote worst case scenario scour (refer to Fig. 6). The BWs were placed in sand with a $d_{50} = 0.8\text{mm}$ and a coefficient of uniformity = 3 (Fig. 7). To determine the flow at which the most scour would occur for a given flow depth ($Y/H = 1.25$ and 2.0), the following section describes the procedure used, which sought to determine the velocity that leads to a ratio of bed shear stress to critical shear stress of 1.

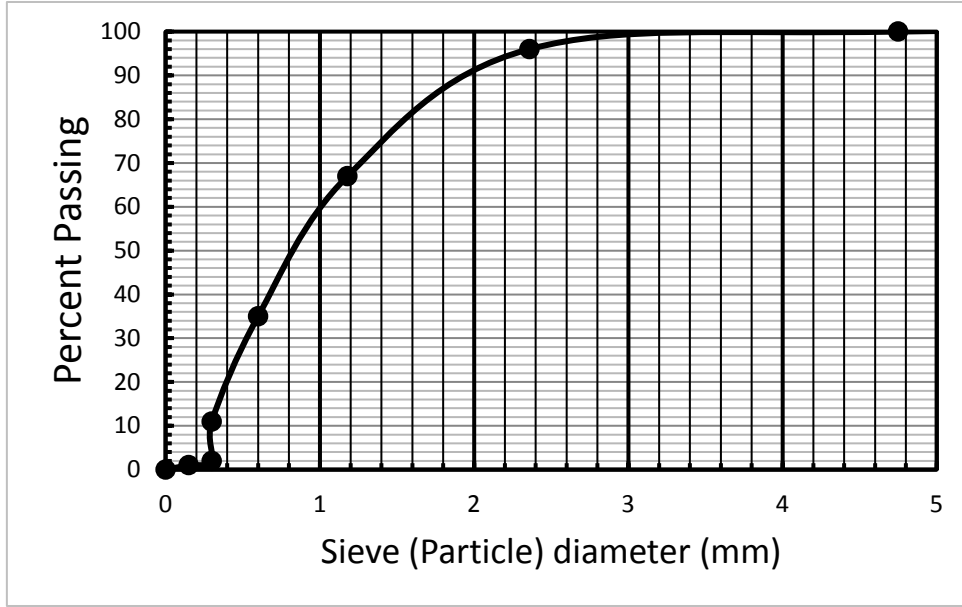


Fig. 7. The sieve analysis of the material used in the sand recess depicted in Fig. 5

To determine the flow at which sediment motion occurs the following equations were used:

The median diameter of the bed sediment was $d = 0.82$ mm. Thus, the critical value of bed shear stress (τ_c) associated with bed sediment incipient motion was estimated using the following equation:

$$\frac{d}{\nu} \sqrt{0.11 \left(\frac{\gamma_s}{\gamma} - 1 \right) g d} = 1.34 \frac{d}{\nu} \sqrt{d} = 1.34 \frac{d^{1.5}}{\nu} = 1.33 \frac{2.35 \times 10^{-5}}{1.30 \times 10^{-6}} = 24.0 \quad (3.1)$$

With $d = 0.82$ mm, from the Shields diagram, erring slightly on conservative side, given the somewhat non-uniformity of sediment, and using $\theta_c = 0.033$, gives

$$\tau_c = \theta_c (\gamma_s - \gamma) d = (0.032)(2.65 - 1.0)(9.81 \times 10^3)(0.82 \times 10^{-3}) = 0.43 \text{ Nm}^{-2} \quad (3.2)$$

To determine the ratio of bed shear stress to critical shear stress for when $Y/H = 1.25$, an iterative sequence of calculations was used:

With $Q = 87$ cfs ($2.46 \text{ m}^3/\text{s}$),

Flow area, $A = 20(2.5) = 50$ ft; wetted perimeter, $P = 20 + 2.5 + 2.5 = 25$ ft (7.6 m); hydraulic radius, $R = A/P = 50/25 = 2.0$ ft or 0.60 m

$$\text{Bulk Velocity, } U = \frac{87}{(50)} = 1.74 \text{ ft/s} = 0.52 \text{ m/s} \quad (3.3)$$

$$\text{Reynolds number, } R_e = \frac{U(4R)}{\nu} = \frac{(0.52 \frac{\text{m}}{\text{s}})(4)(0.60 \text{ m})}{1.3 \times 10^{-6} \frac{\text{m}^2}{\text{s}}} = 0.96 \times 10^6 \quad (3.4)$$

Here ν is the kinematic viscosity, such that:

$$\frac{k}{4R} = \frac{1.0 \times 10^{-3} \text{ m}}{4(0.60 \text{ m})} = 4.2 \times 10^{-4} \quad (3.5)$$

Where k is the grain-roughness height.

From the Moody diagram for flow resistance, the friction factor, $f = 0.013$. To find the shear velocity, u_* :

$$u_* = U \sqrt{\frac{f}{8}} = 0.52 \sqrt{\frac{0.013}{8}} = 2.10 \times 10^{-2} \text{ m/s} \quad (3.6)$$

The bed shear stress, τ_0 was estimated as

$$\tau_0 = \rho u_*^2 = (10^3)(2.10 \times 10^{-2})^2 = 0.44 \text{ Nm}^{-2} \quad (3.7)$$

The ratio of bed shear stress to critical shear stress was:

$$\frac{\tau_0}{\tau_c} = \frac{0.44}{0.43} = 1.02 \quad (3.8)$$

Therefore, this discharge was considered appropriate for the experiment.

Now for when $Y/H=4.0$, with, assume, $Q = 125$ cfs, $A = 20(4.0) = 80$ ft; $P = 20 + 4.0 + 4.0 = 28$ ft; $R = A/P = 80\text{ft}^2/28 \text{ ft} = 2.86$ ft or 0.86 m:

$$U = \frac{125 \text{ cfs}}{80 \text{ ft}^2} = 1.56 \text{ ft/s} = 0.47 \text{ m/s} \quad (3.9)$$

$$Re = \frac{U(4R)}{\nu} = \frac{(0.47)(4)(0.86)}{1.3 \times 10^{-6}} = 1.24 \times 10^6 \quad (3.10)$$

$$\frac{k}{4R} = \frac{1.0 \times 10^{-3}}{4(0.86)} = 2.9 \times 10^{-4} \quad (3.11)$$

From the Moody diagram, $f = 0.0155$ and:

$$u_* = U \sqrt{\frac{f}{8}} = 0.47 \text{ m/s} \sqrt{\frac{0.0155}{8}} = 2.30 \times 10^{-2} \text{ m} \quad (3.12)$$

$$\tau_0 = \rho u_*^2 = (10^3)(2.30 \times 10^{-2})^2 = 0.53 \text{ Nm}^{-2} \quad (3.13)$$

$$\frac{\tau_0}{\tau_c} = \frac{\tau_0}{0.43} = 1.02 \quad (3.14)$$

So

$$\tau_0 = 1.02(0.43) = 0.439 \quad (3.15)$$

And

$$u_* = \sqrt{\frac{\tau_0}{\rho}} = \sqrt{\frac{0.44}{10^3}} = 0.21 \times 10^{-2} \text{ m/s} \quad (3.16)$$

With $f = 0.0155$;

$$U = u_* \sqrt{\frac{8}{f}} = 0.21 \times 10^{-2} \left(\frac{8}{0.0155} \right)^{0.5} = 0.48 \text{ m/s} = 1.60 \text{ ft/s} \quad (3.17)$$

To check that check that the Re found previously matches the Re found from the velocity:

$$Re = \frac{U(4R)}{\nu} = \frac{(0.48)(4)(0.86)}{1.3 \times 10^{-6}} = 1.27 \times 10^6 \quad (3.18)$$

Hence, the value $f = 0.0155$ was assessed as being appropriate.

Thus:

$$Q = UA = 1.60(80) = 127.6 \text{ cfs} = 128.0 \text{ cfs} \left(3.62 \frac{\text{m}^3}{\text{s}} \right) \quad (3.19)$$

With the flow values known, the following procedure was used to perform the scour experiments within the large scale flume:

1. The flume bed and BW (Fig. 8) were LiDAR scanned prior to the experiment. The LiDAR, instrument, a Topcon LTS, was positioned in two locations, either side of the flume, along the centerline axis of the BW. These positions give scans of the top and the front of the BW. Fig. 8 shows the LiDAR positioned at one side of the flume.
2. The flume was filled slowly to above the target depth of 0.8m (2.5ft or 1.25H). Fig. 10 shows the flume filling.
3. Then the flume's gates were gradually opened (to lower flow depth) and the flow rate increased until target flow discharge magnitude was reached. Then the gates were gradually and slowly opened until the target water depth was attained. The "official" timing of the experiment then began.
4. 3-D velocity values were then obtained using ADV.
5. The flow condition was held for two hours. The discharge was gradually decreased and the gates opened so that the flume could slowly drain. The overall duration of experiments with flow capable of developing a local scour was estimated to be about 2 hours.
6. Water in the scour region had to be removed using a suspended suction pump. This step entailed partially draining water from the sediment recess.
7. The sediment recess and BW were LiDAR scanned from both sides of the sediment recess.



Fig. 8. Topcon-TLS LiDAR with operator, scanning flume bed and BW before experiments



Fig. 9. A closer-up view of the BW being assembled in the flume. As noted above, the average diameter of the rock used to form the BW was 0.15 m (6 in)



Fig. 10. The BW during the $Y/H = 1.25$ test, slowly filling up the flume

3.1.1 Processing of LiDAR

First the LiDAR data scanned from the Tarbela flume were processed using Magnet Collage. The LiDAR data were filtered so that there was a maximum of 2 cm (0.8 in) difference between each point using CloudCompare. The scatter data were then edited so that the wall and any excess points were deleted.

3.1.2 Scour Hole Geometry

After performing the experiments with the large-scale flume mentioned above, where the sand reached equilibrium scour, the bed was scanned using LiDAR, which enabled the scour morphology in Fig. 11a&b to be obtained. Scour when $Y/H = 1.25$ was significantly more substantial when $Y/H = 2.0$, where the maximum scour depth is 0.18 m (0.60 ft) and 0.067 m (0.22 ft) when $Y/H = 1.25$ and 2.0. The scour hole geometries for both experiments indicate that the scour starts upstream of the tip of the BW and wraps its way around the tip as it works its way downstream. This same trend was observed by Papanicolaou et al. (2018), where the scour hole started slightly upstream and wrapped around the BW, likely caused by the primary vortex.

The results from the LES show that the mechanism which drives scouring of gravel around the fully submerged barb is driven by the fluid energy from the contraction, transferring to the primary vortex and scouring the bed through the secondary vortices over time, which is the same process as unsubmerged structures such as abutment (Papanicolaou et al. 2018).

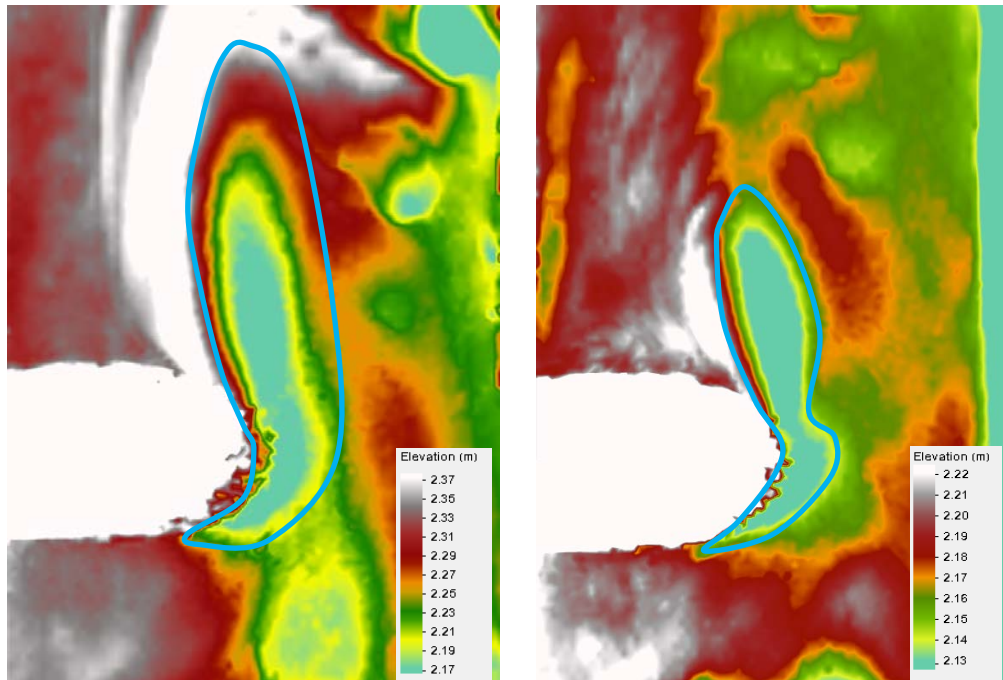


Fig. 11. The scour morphology of the sand bed, obtained from the $\alpha = 90^\circ$ tests LiDAR data when: (a) $Y/H = 1.25$ and (b) $Y/H = 2.0$. The blue line indicates the region where the scour occurred

3.2 Small Flume

CSU's 0.2 m (8 in)-wide flume was used to assess the effects of blockage on scour. This analysis had to be performed because of a lack of data from the Tarbela flume experiment due to the failure of the flume's valve during the experiments. The scour data from the Tarbela flume that were available were the $\alpha = 90^\circ$ $Y/H = 1.25$ and $Y/H = 2.0$ experiments where Y is the flow depth, and H is the BW depth. In order to analyze the $\alpha = 30^\circ$ and 60° experiments using SRH 2D, assumptions about scour depths had to be made due to the lack of Lidar data. One important

assumption that was made and which was the reasoning for the plate experiments was that if the streamwise effect of blockage (projected BW length, L/B) remained the same, the maximum scour depth would remain approximately equal between the 30°, 60°, and 90° experiments. This assumption arose from the NCHRP 24-20 report (Ettema et al. 2010), which found this to be the case for bridge abutments. Thin plates were chosen to ensure the focus of the effects of blockage on scour, rather than roughness and BW width.

3.2.1 Flume Layout

The experiments used a re-circulating Plexiglas-wall flume that was 9.70 m (31.8 ft) long, 0.20 m (8 in) wide and 0.36 m (14 in) deep (Fig. 12). A series of horizontal baffles was installed at the flume's inlet, to ensure the flow entering the flume was uniformly distributed and free of large turbulence structures, as shown in Fig. 13. The flow entered the flume sufficiently upstream of the location of the plates so that the flow developed the velocity profile typical of fully developed turbulent flow. Rocks were added (Fig. 14) after the baffles to reduce the amount of scour of the sand and ensure the logarithmic velocity profile was met.



Fig. 12. The 8in-wide (0.20m) flume used for the study

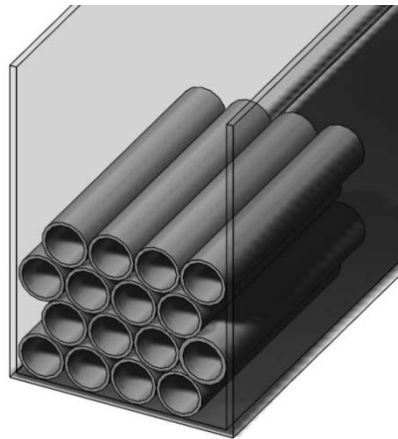


Fig. 13. Horizontal baffles installed at the flume inlet to ensure fully developed flow within the flume

Flow rate was measured through an orifice plate connected to the pump operation on the flume. The orifice plate was used to measure flow rate due to its restriction of the flow, causing a reduction of pressure. Thus, a pressure differential, Δh , was measured and converted into a discharge using an equation specific to the orifice plate, Eq 3-7. Average velocity could then be calculated based on the flow area;

$$Q = 0.228 \Delta h^{0.503} \quad (3.20)$$

Where Q is flow rate in cubic feet per second (cfs) and Δh was the pressure difference in feet.



Fig. 14. The rocks added just downstream of the baffles

3.2.2 Plates Used in Study

The thin, 2-dimensional plates were chosen to perform this analysis, which investigated the effect of blockage on the flow field. The plates were placed at the halfway point of the sand to ensure that they were sufficiently downstream of the rocks so that there would be a fully developed turbulent flow, velocity profile. The plates were 5.1cm (2in) tall (H) and were designed so that the width (L) was equal to half of the flume. The flow depth was determined to be 6cm, 2.5in (Y/H = 1.25) and 10cm, 4in (Y/H = 2.0).

3.2.3 Sand Used in Study

Fine sand was used the bed material with $d = d_{50}$ of 0.26mm, as this sand was already in the flume. The ratio of bed shear stress to critical shear stress was held constant at 0.8 for all experiments (Y/H = 1.25 and Y/H = 2.0 at 30°, 60°, and 90°). These experiments aimed to

compare the magnitude of each scour depth to each experiment in order to deny or confirm the assumption that with the same amount of streamwise blockage, the maximum scour depth will remain the same. Accordingly, scaling down from the Tarbela flume to dimensions of the 8in-wide flume was not a concern.



Fig. 15. The flume with a sand bed

To compare the scour depths of both cases ($Y/H = 1.25$ and $Y/H = 2.0$), the ratio of bed shear stress to critical shear stress (τ_o/τ_c) was held constant at 0.8, so that clearwater scour occurred.

To find the critical shear stress, the following equation from Julien (2010) was used;

$$\tau_{*c} \approx 0.3e^{-\frac{d_*}{3}} + 0.06 \tan \phi \left(1 - e^{-\frac{d_*}{20}} \right) \quad (3.21)$$

Where the dimensionless particle diameter, d_* was found using;

$$d_* = d_s \left(\frac{(G - 1)g}{v_m^2} \right)^{\frac{1}{3}} \quad (3.22)$$

And;

$$\tau_{*c} = \frac{\tau_c}{(\gamma_s - \gamma_m)d_s} \quad (3.23)$$

And;

$$\tau_c = \tau_{*c}((\gamma_s - \gamma_m)d_s) \quad (3.24)$$

The flow rate was estimate using:

$$Q = V(wh) \quad (3.25)$$

Where w was the flume width, h was the flow depth, and V was the velocity

where;

$$V = \sqrt{\left(\frac{8}{f}\right) \left(\frac{\tau_o}{\rho}\right)} \quad (3.26)$$

f (Darcy Weisbach friction factor) was estimated from the Moody diagram, using d/R

($d = d_{50}$ and $R =$ hydraulic radius) and $Re = \frac{VR}{\nu}$, and $\rho = 1.94 \frac{\text{slugs}}{\text{ft}^3}$, and $\tau_o = \gamma RS_f$ where S_f was assumed to equal S_o , where R is the hydraulic radius, and γ is the unit weight of water (9810 Nm^{-3}).

The bed shear stress was determined by finding a bed slope (S_o) so that $\frac{\tau_o}{\tau_c} = 0.8$. To find the correct values of velocity, an initial velocity value was plugged into Re to find a value of f . The values of f and τ_o were then plugged into Eq. (3.24) and solved iteratively; if the calculated velocity matched the assumed velocity then the velocity value was chosen correctly.

Lastly, the flow (Q) could be calculated using;

$$Q = VA = V(Wh) \quad (3.27)$$

An example calculation ensues for $Y/H = 2.0$.

First the critical shear stress was found;

$$\tau_{*c} \approx 0.3e^{-\frac{d_*}{3}} + 0.06 \tan \phi (1 - e^{-\frac{d_*}{20}}) \quad (3.28)$$

$$d_* = 0.00026 \text{ m} \left(\frac{(2.65 - 1) * 9.81 \frac{\text{m}}{\text{s}^2}}{\left(1 \times 10^{-6} \frac{\text{m}^2}{\text{s}}\right)^2} \right)^{\frac{1}{3}} = 6.58 \quad (3.29)$$

$$\tau_{*c} \approx 0.3e^{-\frac{6.58}{3}} + 0.06 \tan(32) \left(1 - e^{-\frac{6.58}{20}}\right) = 0.044 \quad (3.30)$$

$$\tau_c = 0.044x \left(62.4 \frac{\text{lb}}{\text{ft}^3} x 2.65 - 62.4 \frac{\text{lb}}{\text{ft}^3}\right) x 0.00085 \text{ ft} = 0.0039 \frac{\text{lb}}{\text{ft}^2} \quad (3.31)$$

Next the bed shear stress was found using a bedslope so that $\frac{\tau_o}{\tau_c} = 0.8$;

$$\tau_o = \gamma R S_o \quad (3.32)$$

$$R = \frac{\left(\frac{8.19 \text{ in}}{12}\right) \left(\frac{4 \text{ in}}{12}\right)}{\left(\frac{8.19 \text{ in}}{12}\right) + 2 \left(\frac{4 \text{ in}}{12}\right)} = 0.17 \text{ ft} \quad (3.33)$$

$$\tau_o = 62.4 \frac{\text{lb}}{\text{ft}^3} x 0.17 \text{ ft} x 0.0003 = 0.0032 \frac{\text{lb}}{\text{ft}^2} \left(0.15 \frac{\text{N}}{\text{m}^2}\right) \quad (3.34)$$

Next the Reynolds Number and relative roughness were found in order to determine the friction factor;

A value of 0.59 ft/s was chosen for the first iteration making R_e and relative roughness;

$$R_e = \frac{0.59 \frac{\text{ft}}{\text{s}} x 0.17 \text{ ft}}{1.06 x 10^{-5} \frac{\text{ft}^2}{\text{s}}} = 9384 \quad (3.35)$$

$$\frac{d}{R} = \frac{8.5 x 10^{-4} \text{ ft}}{0.17 \text{ ft}} = 0.0051 \quad (3.36)$$

From the Moody Diagram a friction factor value (f) of 0.038 was found. The velocity was then found plugging this value of f of into equation (3.26);

$$V = \sqrt{\left(\frac{8}{0.038}\right) \left(\frac{0.0032 \frac{\text{lb}}{\text{ft}^2}}{1.94 \frac{\text{slugs}}{\text{ft}^3}}\right)} = 0.59 \frac{\text{ft}}{\text{s}} \quad (3.37)$$

Therefore, this assumption of velocity was valid and the flow calculations can proceed;

$$Q = 0.59 \frac{\text{ft}}{\text{s}} \times 0.682 \text{ ft} \times 0.33 \text{ ft} = 0.133 \frac{\text{ft}^3}{\text{s}} \left(0.0038 \frac{\text{m}^3}{\text{s}} \right) \quad (3.38)$$

The calculations are summarized in the tables below.

Table 1. Calculated data used to determine the flow values for Y/H = 1.25 (a) and Y/H = 2.0 (b)

Y/H = 1.25	
d ₅₀ (mm)	0.26
w (m, ft)	0.21, 0.68
h (m, ft)	0.06, 0.21
S ₀	0.00039
R (m, ft)	0.040, 0.13
τ ₀ (Pa, psf)	0.15, 0.0032
τ _c (Pa, psf)	0.19, 0.0039
τ ₀ /τ _c	0.814
Relative Roughness	0.0066
Re	6833
f	0.041
V assumed (m/s, ft/s)	0.17, 0.56
V calculated (m/s, ft/s)	0.17, 0.56
Q (cms, cfs)	0.002, 0.080

Y/H = 2.0	
d ₅₀ (mm)	0.26
w (m, ft)	0.21, 0.68
h (m, ft)	0.10, 0.33
S ₀	0.0003
R (m, ft)	0.052, 0.17
τ ₀ (Pa, psf)	0.15, 0.0032
τ _c (Pa, psf)	0.19, 0.0039
τ ₀ /τ _c	0.82
Relative Roughness	0.0051
Re	9384
f	0.038
V assumed (m/s, ft/s)	0.18, 0.59
V calculated (m/s, ft/s)	0.18, 0.59
Q (cms, cfs)	0.004, 0.13

3.2.4 Small Flume Experimental Procedure

Pieces of metal were cut for the 30°, 60°, and 90° experiments so that the same amount of streamwise blockage occurred (half of the flume). The slope of the flume was adjusted depending on the experiment ($S_o = 0.00039$ for $Y/H = 1.25$ and $S_o = 0.0003$ for $Y/H = 2.0$). The initial bed elevation was then measured using the point gage (Fig. 17).

The flume was gradually filled up with water by slowly increasing the speed of the pump, and adjusting the downstream gate height to ensure that the sand did not scour before the plate was placed in. The speed of the pump and the gate height were adjusted until the target flow value and depth were reached for both the $Y/H = 1.25$ and $Y/H = 2.0$ experiments. The flow was determined using equation 1, plugging the change of head into it using determined by difference in monometers.

Once the flow and depth were at the correct values, the plate was then placed into flow for the experiments at $\alpha = 30^\circ, 60^\circ$, and 90° , ensuring that the same amount of streamwise blockage occurred for all experiments. This step imitated natural conditions, where a BW is designed to be already submerged under base flow, rather than starting from a dry bed. For the angled experiments this was done by measuring the distance from the tip to the right wall.

To determine the amount of time needed to reach an equilibrium depth of scour, the experiments with $Y/H = 1.25$ and 2.0 , with the plates at $\alpha = 90^\circ$, were left to run for 30 and 60 minutes and the max scour depths then were compared. It was determined that it took about 30 minutes to reach equilibrium for these two experiments, as there was little difference in maximum scour depths after 30 and 60 minutes. For $\alpha = 30^\circ$ and $\alpha = 60^\circ$ experiments, the flume was left to run for 30 minutes (to reach equilibrium). After 30 minutes, the water was gradually

drained to ensure no further scour of the sand bed. The maximum scour depths were then measured to the thousandth using a point-gage.



Fig. 16. Example of a plate test in progress



Fig. 17. The point gage used to measure the scour depths

3.3. SRH-2D

SRH-2D was used to determine the effect of scour on the velocity field. To use the model accurately, calibration had to be performed, as well as multiple sensitivity analyses. The parameters used and the methods for the calibration of the parameters are outlined in the subsequent sections.

3.3.1 Assumptions/Simplifications

In order to use the 2-D model, several key assumptions were made. The first assumption being the scour for $\alpha = 90^\circ$ for both degrees of submergence could be applied to $\alpha = 30^\circ$ and $\alpha = 60^\circ$ due to a lack of hydraulic model data. A detailed summary of the testing of this assumption is found in Section 4.1. Another key assumption was that “smooth” BWs created in AutoCAD could be used for $\alpha = 30^\circ$ and $\alpha = 60^\circ$ due to a lack of hydraulic model data. A detailed summary of the testing of this assumption is found in Section 3.2.11.

It was also assumed that the flow depth at the outlet was constant. Although the concrete was the bottom surface upstream and downstream of the sand recess within the large flume, it was assumed that the material downstream of the BW was sand (in reality, it was concrete) because the sand from the scour hole was deposited well downstream of the sand recess.

3.3.2 Model Setup

To run the simulation, SMS requires a mesh, boundary conditions, monitor points, and materials, where Manning’s roughness values are assigned. The flume was assigned a patch mesh type and the area surrounding the BW was assigned a paving mesh type. The sand and the BW were assigned a Manning’s roughness value, set differently for each flow depth and found performing a sensitivity analysis. Similarly, the time step was determined using a sensitivity analysis for each flow depth. Four boundary conditions are used (left and right wall, inlet, and outlet) to run the experiment. The model was run for one hour with subcritical flow, a parabolic

turbulence model, and an output frequency of 0.25 hours. Monitor points, where model parameter outputs were found, were placed upstream of the BW and within the region of maximum velocity. The parameters that were calibrated using $\alpha = 90^\circ$ when $Y/H = 1.25$ and 2.0 were used for $\alpha = 30^\circ$ and $\alpha = 60^\circ$. A detailed description of the reasoning behind each parameter chosen is presented in the subsequent sections.

3.2.3 Boundary Conditions

As the stipulation of the boundary conditions influences the model's accuracy, care was taken, especially when considering the location of the inlet and outlet boundary conditions. The model was run with an inlet at a constant discharge ($Q = 2.46$ cms or 87 cfs when $Y/H = 1.25$ and 3.62 cms or 128 cfs when $Y/H = 2.0$), and a conveyance distribution of flow. The outlet also had a subcritical flow with a constant water surface elevation. At the left and right edges of the model, wall boundary conditions were used, where the no slip boundary starts. The wall BCs were assigned a 2 mm roughness height, based on the roughness of the concrete within the flume. Two monitor lines were used to ensure the flow in was equal to the flow out.

3.2.4 Boundary Sensitivity Analysis

If the inlet and outlet boundary conditions were placed too close to the BW, inaccuracies may arise. Because it takes time for the flow to fully develop, if the inlet is placed too close to the BW, the velocity values obtained could all be inaccurate. Likewise, if the outlet BC are placed too close to the BW, where eddies occur, large errors in the calculations could occur because the flow entering the outlet BCs are assumed to have no velocity gradients. Versteeg & Malalasekera (2007), recommend an outlet location much greater than 10 widths of the obstruction. In this case, the BW width is 3.1 m (10 ft), so the outlet should be located greater than 30.5 m (100 ft) away from the BW.

The upstream and downstream boundary conditions were extended about 40 m (131 ft) for both experiments ($Y/H = 1.25$ and 2.0). It was found that by increasing the inlet and outlet boundary conditions, the average decrease in velocity was 9.4% when $Y/H = 1.25$ and 1.6% when $Y/H = 2.0$ after comparing the extended inlet and outlet to the original inlet and outlet locations at the upstream, crest, maximum scour and maximum velocity cross sections, as indicated in Fig. 18. Consequently, when increasing the distance to the inlet and outlet locations, the velocity results were not significantly impacted ($>10\%$).

Fig. 19 and Fig. 20 show that at the maximum velocity cross section, which was the cross section of concern, the values of depth and velocity do not change substantially between the velocity and the depth for $Y/H = 1.25$ and 2.0 .

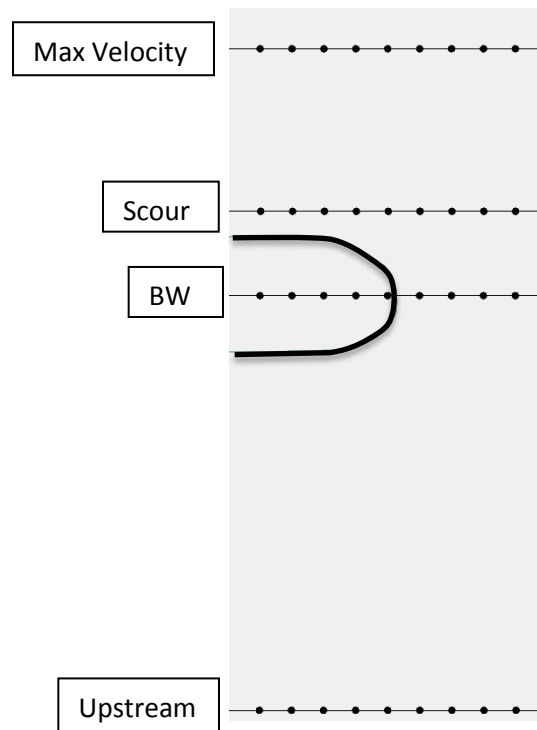


Fig. 18. The locations of the cross sections where the velocity from the extended inlet and outlet were compared to the original inlet and outlet

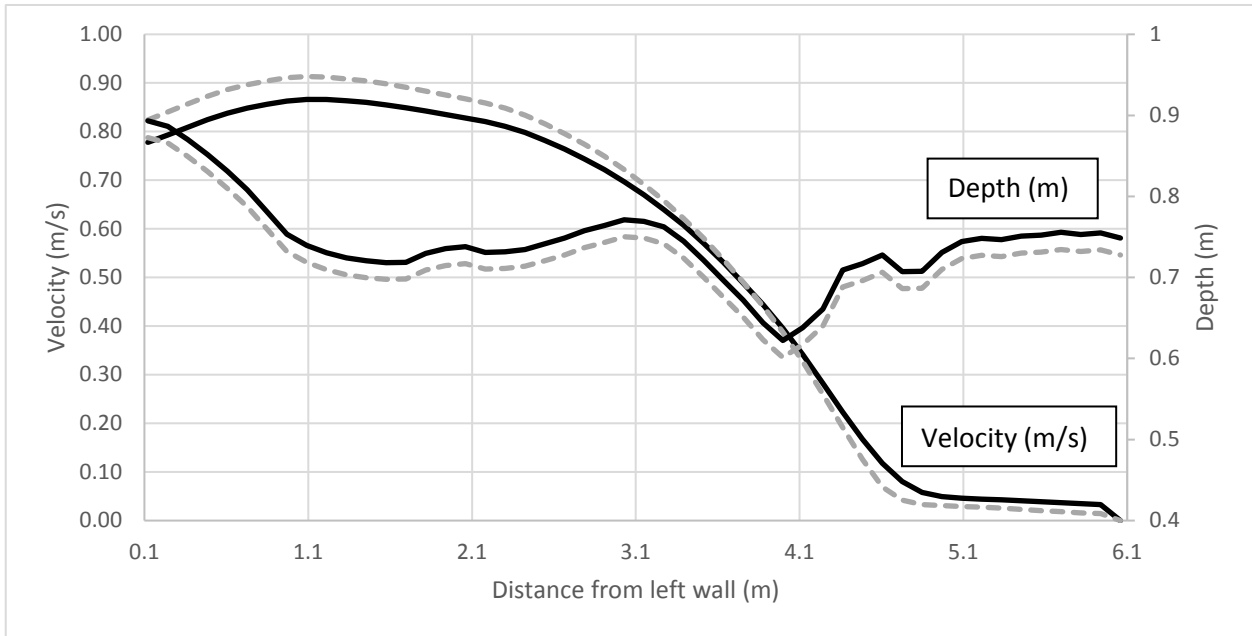


Fig. 19. Comparing velocity and depth after extending the upstream and downstream boundary conditions by about 40 m when $Y/H = 1.25$ at the maximum velocity cross section depicted in Fig. 18

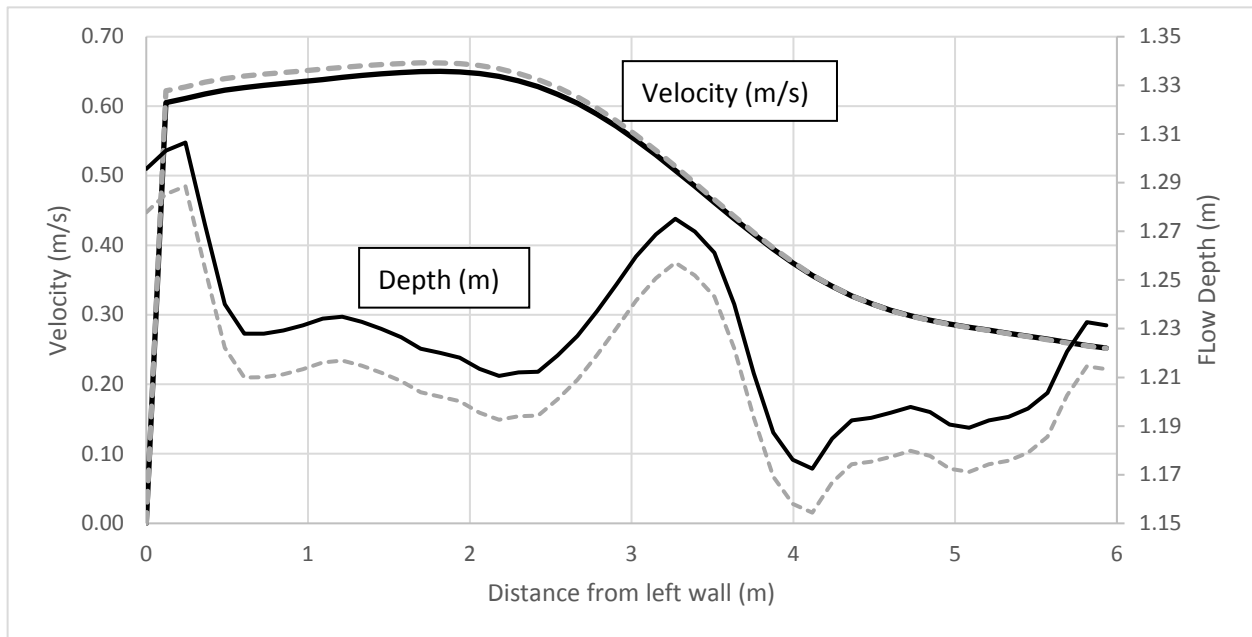


Fig. 20. Comparing velocity and depth after extending the upstream and downstream boundary conditions by about 40 m when $Y/H = 2.0$ at the maximum velocity cross section depicted in Fig. 18

3.2.5 Manning's n Sensitivity Analysis

Observation points were used to calibrate the model. From the hydraulic model, the lateral and downstream velocities at 0.6 of the flow depth were used to calibrate the model at the locations depicted in in Fig. 21. Therefore, it was assumed that the velocities within the contracted region and on/near the crest were close to logarithmic in their vertical distribution. The domain within SRH-2D was then rotated to 90 degrees to make it easier to input the prototype angles. The concrete, BW, and sand were assigned Manning's n values. The concrete was assigned a constant value of 0.02, in accordance with practical values (Chow 1959). To calibrate the model to prototype values at locations indicated in Fig. 21, with insights from FLOW-3D, where the locations that were compared indicated in Fig. 22 the Manning's n value was adjusted until the Root Mean Square Error (RMSE) was its lowest value.

The large scale flume RMSE, $RMSE_L$ and the 3-D model RMSE, $RMSE_{3D}$ were defined as:

$$RMSE_L = \sqrt{\sum_{i=1}^n \frac{(DAV_L - DAV_{2D})^2}{n}} \text{ and } RMSE_{3D} = \sqrt{\sum_{i=1}^n \frac{(DAV_{3D} - DAV_{2D})^2}{n}} \quad (3.39)$$

where DAV_L was the depth average velocity of the large scale flume and DAV_{3D} was the depth average velocity from FLOW-3D.

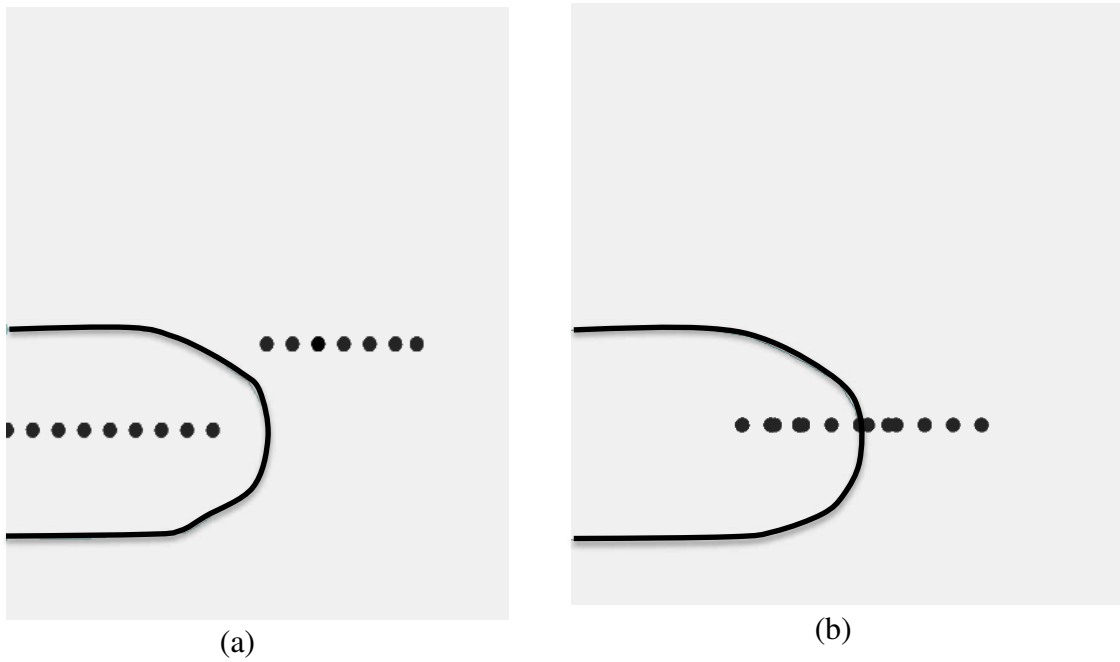


Fig. 21. The locations of the comparison between the hydraulic model and SRH-2D depth-average velocity for: (a) $Y/H = 1.25$ and (b) $Y/H = 2.0$

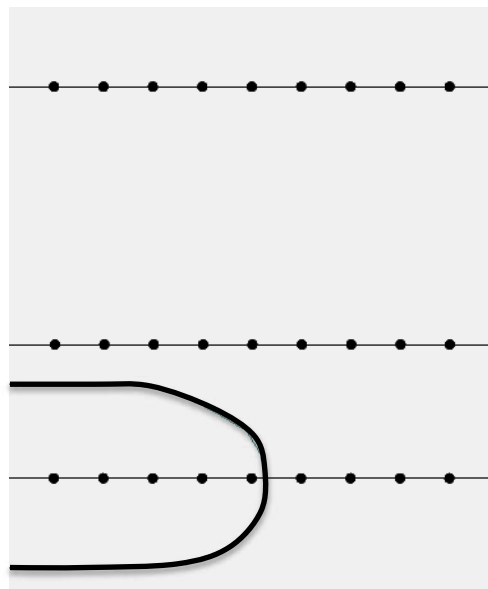


Fig. 22. The general cross section locations where the 2-D model was compared to the 3-D model for $Y/H = 1.25$ and 2.0 , $\alpha = 90^\circ$

After analysis, taking into consideration the large flume RMSE ($RMSE_L$) and FLOW-3D RMSE ($RMSE_{3D}$), when $Y/H = 1.25$ the Manning's n values were 0.032 and 0.07 for the sand

and BW (Fig. 23), with $RMSE_L = 0.047$ m/s and $RMSE_{3D} = 0.085$ m/s. When $Y/H = 2.0$ the Manning's n values were 0.046 and 0.13 for the sand and the BW (Fig. 23), respectively, with $RMSE_L = 0.072$ m/s and $RMSE_{3D} = 0.057$ m/s.

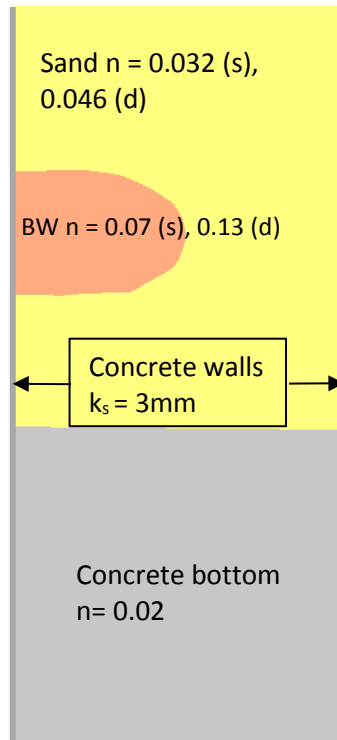


Fig. 23. The Manning's n values assign to the sand, BW, concrete bottom, and walls for $Y/H = 1.25$ and 2.0 . Note that "s" indicates the shallow flow ($Y/H = 1.25$) and "d" indicates the deeper flow ($Y/H = 2.0$)

3.2.6 Mesh Setup

SMS allows for an unstructured mesh, so either quadrilateral or equilateral triangular mesh element shapes can be used. However, the quadrilateral shaped mesh elements were used whenever possible due to a reduction of elements, thus decreasing the number of total elements used. This was because a quadrilateral element covers more area than triangular elements and a quadrilateral element can maintain good interior angles while still having high resolution in one direction, thus making the elements more numerically stable (Lai 2008). The mesh surrounding the BW was composed of triangular elements due to the irregularity of the BW. Upstream and

downstream of the BW, quadrilateral mesh was used as Fig. 24 displays. To ensure that each mesh for all experiments allowed for quality results, the mesh quality command within SMS was used, where the maximum interior angle allowed was 10° , the maximum interior angle allowed was 130° , the maximum element area change was set at 50% and the maximum amount of connecting elements allowed was 8. If any of these criteria were not met, the consequence would be evident on the mesh. Each mesh varied slightly in the total amount of mesh elements, but the total amount of mesh elements used when $Y/H = 1.25$ for $\alpha = 90^\circ$ was 34,680 and $Y/H = 1.25$ for $\alpha = 90^\circ$ was 34,853.

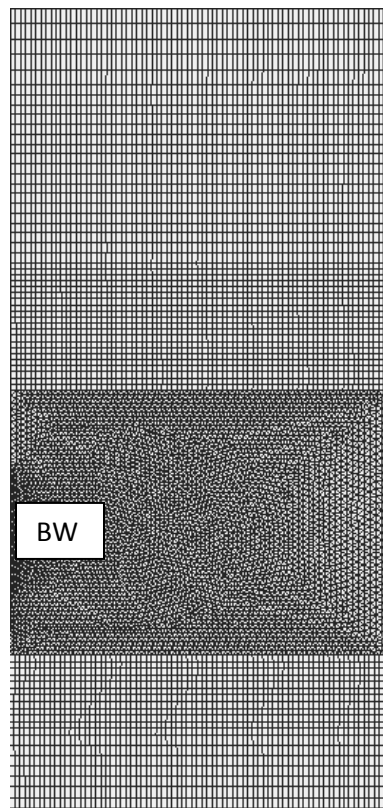


Fig. 24. Example mesh. Note the fine mesh used in the contracted section where the velocity is greatest

3.2.7 Mesh Sizing

The approach to mesh sizing was to first check for grid size independence. For grid independence, three average sizes of mesh were created, with the baseline based on the approximate d_{50} of the rocks used for the study (15 cm, 6 in). The simulations used for the baseline experiment was when $Y/H = 1.25$ and 2.0 , $\alpha = 90^\circ$ due to physical model data available to verify the results. Average mesh size finer (0.09 m, 3.54 in) and coarser (0.18 m, 7.1 in) for both flow depths, than the baseline mesh (0.14 m, 5.5 in) were used to determine if there was a significant change in velocity values between them. RMSE was used to compare each mesh size depth average velocity values to the values obtained from the large-scale flume ($RMSE_L$) ADV data and depth average velocity from FLOW-3D ($RMSE_{3D}$). As displayed in Table 2, the $RMSE_L$ and $RMSE_{3D}$ did not change significantly between each mesh size ($RMSE \leq 0.005$ m/s). Therefore, the medium mesh size was used.

Table 2. RMSE between the large-scale flume depth average velocity data and FLOW-3D depth average velocity data for fine, medium, and coarse size mesh when $Y/H = 1.25$ and 2.0

	Y/H = 1.25			Y/H = 2.0		
	Fine (m/s)	Medium (m/s)	Coarse (m/s)	Fine (m/s)	Medium (m/s)	Coarse (m/s)
$RMSE_L$	0.052	0.047	0.053	0.071	0.071	0.076
$RMSE_{3D}$	0.086	0.085	0.087	0.059	0.057	0.054

To check if the mesh selected (based on the mesh independence study) accurately represented the geometry of the study area, the mesh elevation was compared to LiDAR elevations. The cross-sections, Crest and Scour Hole were chosen to determine the precision of the mesh elevation as compared to the LiDAR elevations for $Y/H = 1.25$ and 2.0 because the elevation changes the most within these cross sections. Fig. 25 through Fig. 28 displays that there were not any areas of concern between the LiDAR and the mesh elevations for $Y/H = 1.25$ and 2.0 .

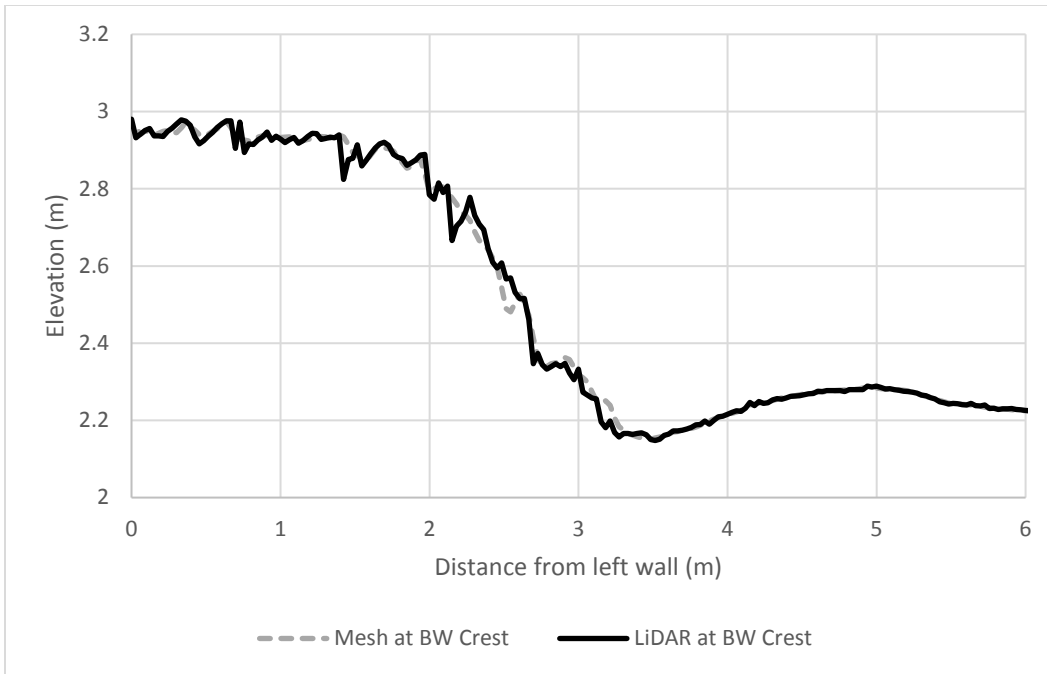


Fig. 25. Mesh elevation versus the LiDAR elevation at the Crest cross section when $Y/H = 1.25$

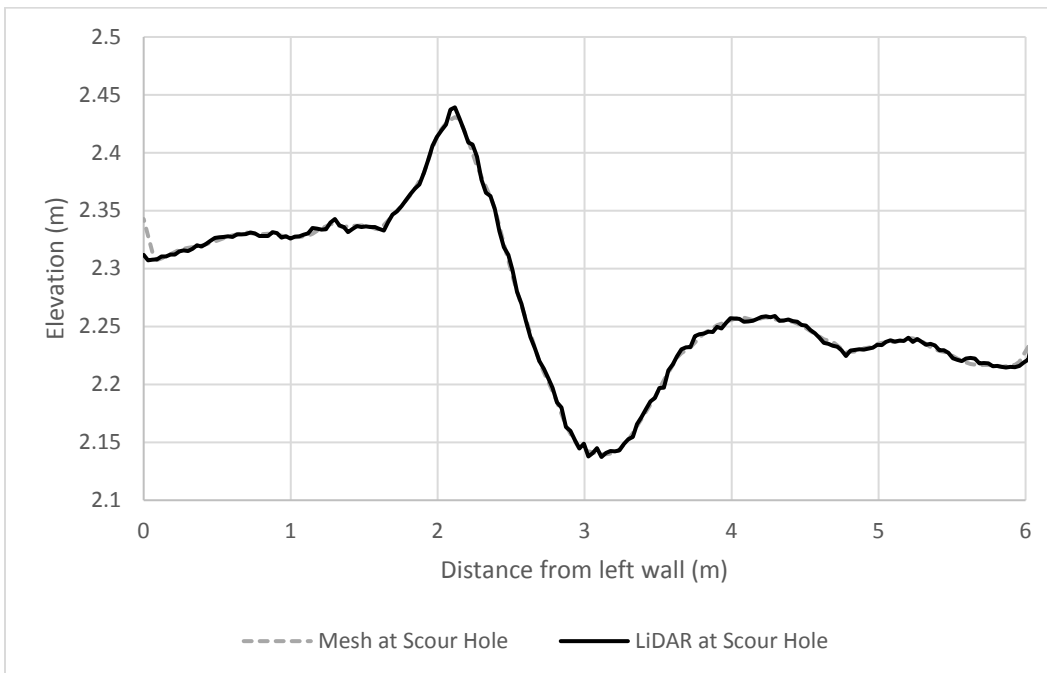


Fig. 26. Mesh elevation versus the LiDAR elevation at the Scour Hole cross section when $Y/H = 1.25$

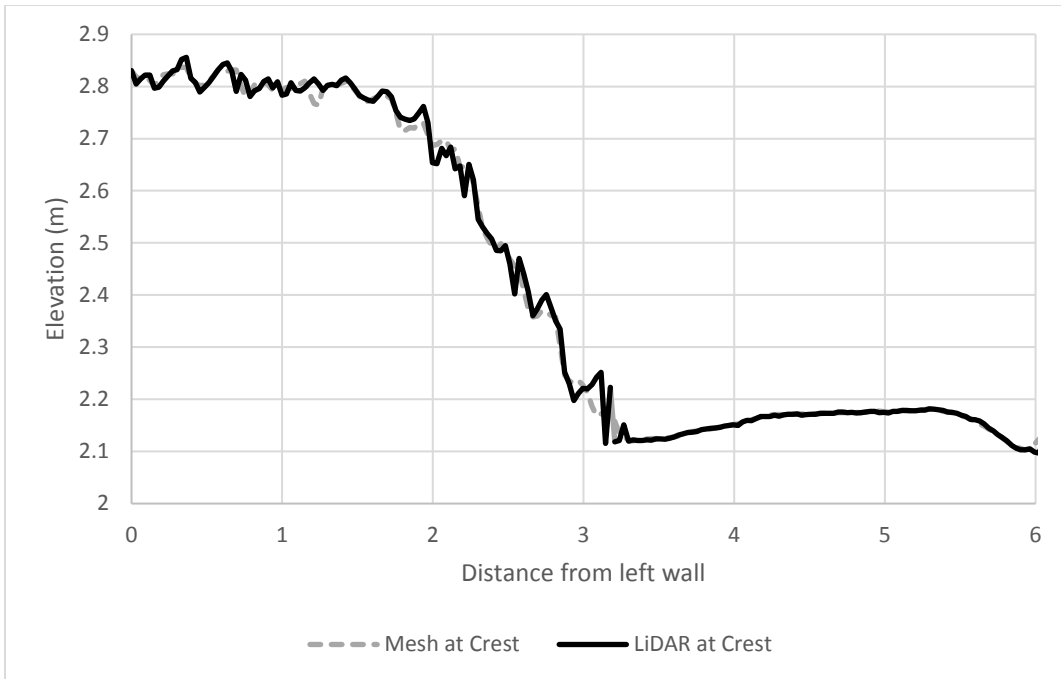


Fig. 27. Mesh elevation versus the LiDAR elevation at the Crest cross section when $Y/H = 2.0$

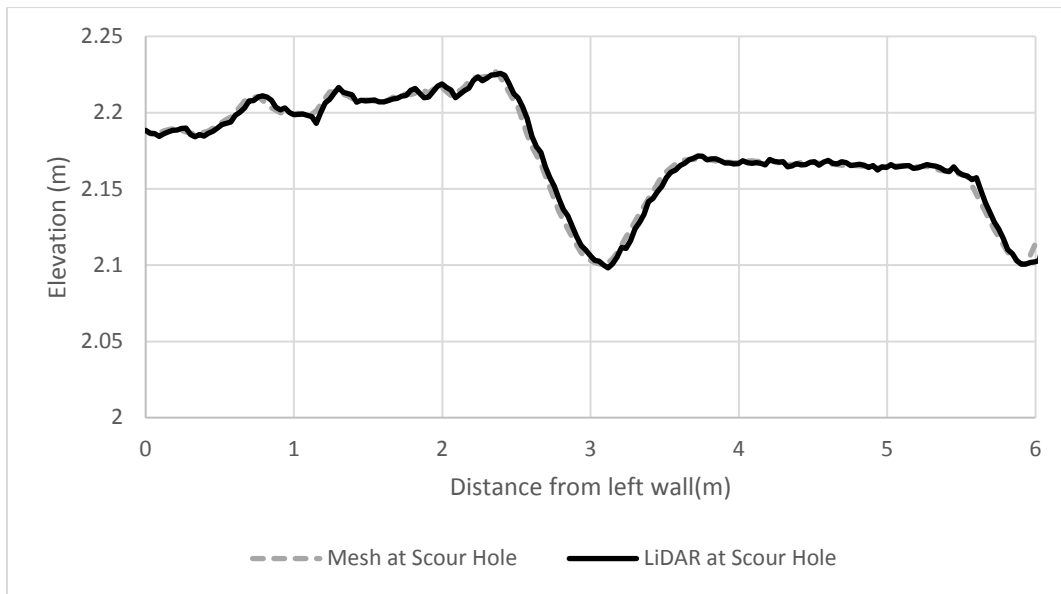


Fig. 28. Mesh elevation versus the LiDAR elevation at the Scour Hole cross section when $Y/H = 2.0$

Another important consideration was to determine if the mesh size was small enough so that the eddying motion in the wake of the BW was being captured. As can be seen in Fig. 29a&b, both the fine and coarse meshes capture eddying occurring when $Y/H = 1.25$. It was interesting to note that the center of the eddy moves upstream slightly (about 1.05m, 3.4ft) when using the coarser mesh. When $Y/H = 2.0$, no eddying occurred at any mesh size.

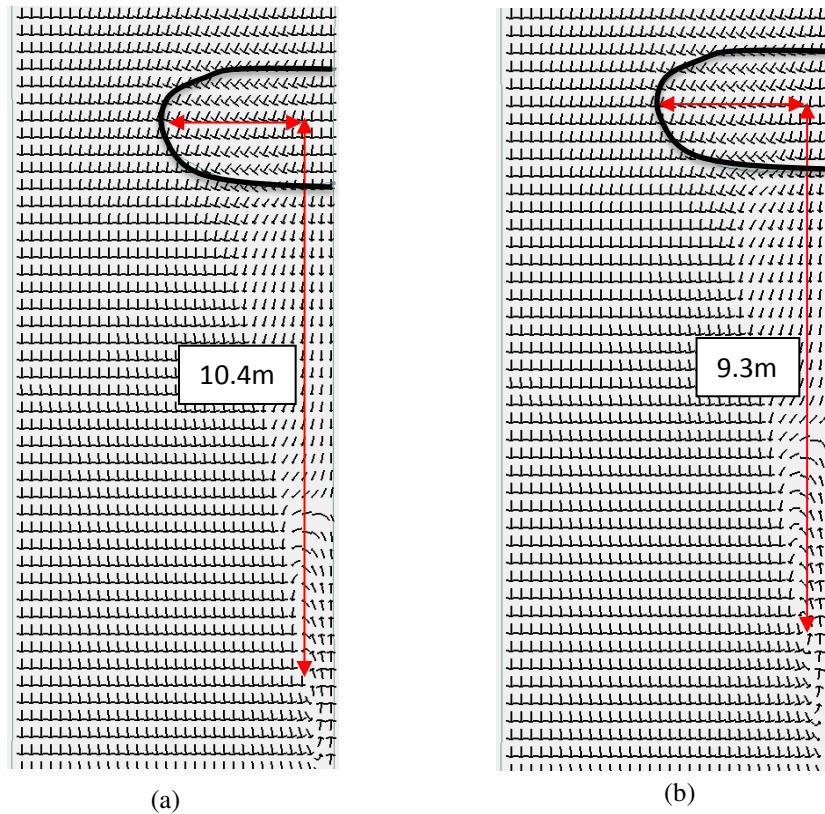


Fig. 29. The velocity vectors when $Y/H = 1.25$: (a) fine mesh size and (b) medium mesh size. The red arrows indicate the center of the eddy from the crest of the BW

3.2.8 Time Step

The time step was determined based off the Courant-Friedrichs-Lewy (CFL) condition ($\frac{u\Delta t}{\Delta x} \leq 1$). Although stability was not affected by the time step due to the implicit scheme, the CFL number can indicate the accuracy of a solution (Piotrowski 2010). If the Courant number is large, even though the solution will be stable, the solution will be smeared since data are being

obtained from the cells upstream of the cell where the calculations were occurring. Using an implicit scheme, CFL values less than 5 have been successfully used (Bates et al. 1998).

Once the CFL conditions were determined, a sensitivity analysis was performed based on of the advective CFL condition ($\frac{u\Delta t}{\Delta x} \leq 1$) as well as the gravitational CFL condition ($\frac{\sqrt{gh}\Delta t}{\Delta x} \leq 1$). The advective CFL condition yielded a minimum time step (TS) of 0.06 s when $Y/H = 1.25$ and 0.08 s when $Y/H = 2.0$ for the baseline condition when $\alpha = 90^\circ$ using SMS's dataset toolbox Coastal tool. The gravitational CFL condition yielded a minimum TS of 0.02 s when $Y/H = 1.25$ and 0.01 s when $Y/H = 2.0$. To prove time step independence, a TS of 0.2 s was used as the upper value of time steps.

Each time step value was compared to the depth average velocity values from the large scale flume and FLOW-3D. When $Y/H = 1.25$, using the gravity CFL condition (TS = 0.02 s) $RMSE_L = 0.052$ m/s and $RMSE_{3D} = 0.079$ m/s; using the Advective CFL condition (TS = 0.06 s) $RMSE_L = 0.048$ m/s and $RMSE_{3D} = 0.085$ m/s; and when the TS = 0.2 s $RMSE_L = 0.049$ m/s and $RMSE_{3D} = 0.085$ m/s.

When $Y/H = 2.0$ using the gravity CFL condition (TS = 0.01 s) $RMSE_L = 0.071$ m/s and $RMSE_{3D} = 0.057$ m/s; using the Advective CFL condition (TS = 0.08 s) $RMSE_L = 0.071$ m/s and $RMSE_{3D} = 0.057$ m/s; and when TS = 0.2 s $RMSE_L = 0.071$ m/s and $RMSE_{3D} = 0.057$ m/s.

Due to the low difference in RMSE values (<0.009 m/s) between the different time steps at the shallow ($Y/H = 1.25$) and deeper flow depths ($Y/H = 2.0$), it was determined that a TS = 0.06 s and TS = 0.08 s when $Y/H = 0.08$ s when $Y/H = 1.25$ and 2.0, respectively.

3.2.9 Convergence/Accuracy of Model

To check the convergence of the models, first output files from the monitor lines containing the flow data were analyzed so that the flow into the first monitor line was equal to the flow out of the second monitor line. Once these values were equal to one another the values from the observation points output file were analyzed so that the velocity values between the last and second to last time increment did not change greater than 0.0003 m/s, as was used by Zey (2017) in a study analyzing the effects of contraction on the flow field using SRH-2D. If these changes in velocity were greater than this prescribed value, then the simulation run time was increased. In the end, a run time of 1 hour was found to not change the velocity values significantly.

3.2.10 Turbulence model

To model the turbulence correctly, particularly within the wake of the BW, the two available turbulence models, the two equation $k - \epsilon$ and the zero equation parabolic turbulence models were compared. The depth average velocity of the 2-D model was first compared to the hydraulic model ($RMSE_L$) and the depth average velocity from FLOW-3D ($RMSE_{3D}$) in the regions indicated in Fig. 21 and Fig. 22. As Table 3 indicates, the difference in RMSE between the parabolic and $k - \epsilon$ turbulence models is not significant (>0.008 m/s) when comparing the models around the areas of interest in the flume.

Table 3. The RMSE comparing parabolic to the $k - \epsilon$ turbulence model for $Y/H = 1.25$ and 2.0

	Y/H = 1.25		Y/H = 2.0	
	Parabolic (m/s)	$k - \epsilon$ (m/s)	Parabolic (m/s)	$k - \epsilon$ (m/s)
$RMSE_L$	0.047	0.047	0.071	0.069
$RMSE_{3D}$	0.085	0.079	0.057	0.050

Because most of the turbulence within the model was within the wake of the BW, to get an in depth look at the performance of the turbulence models, 90 points were selected in the wake of the BW to compare SRH-2D to FLOW-3D in the locations indicated in Fig. 30. When $Y/H = 1.25$ the $RMSE_{3D}$ was determined to be 0.133 m/s and 0.136 m/s when using the parabolic and $k - \epsilon$ turbulence model, respectively. Therefore it was determined that the parabolic turbulence model could be used because there wasn't a significant difference between it and the $k - \epsilon$ turbulence model, despite Lai (2010) suggesting to use the $k - \epsilon$ turbulence model in simulations where significant flow separation occurs, which occurs in the wake of the BW in this study.



Fig. 30. The location of the points (blue dots) in the wake of the BW where FLOW-3D DAV was compared to SRH-2D DAV using the $k-\epsilon$ and parabolic turbulence models

It was also interesting to note that after comparing the eddying region, using velocity vectors within SMS, the position of the center of the eddy changed by about 2.0 m when $Y/H = 1.25$, so that the $k - \epsilon$ turbulence model was centered more upstream as Fig. 31 indicates. As mentioned in Section 3.2.7, when $Y/H = 2.0$, SRH-2D does not find any eddying in the wake of the BW.

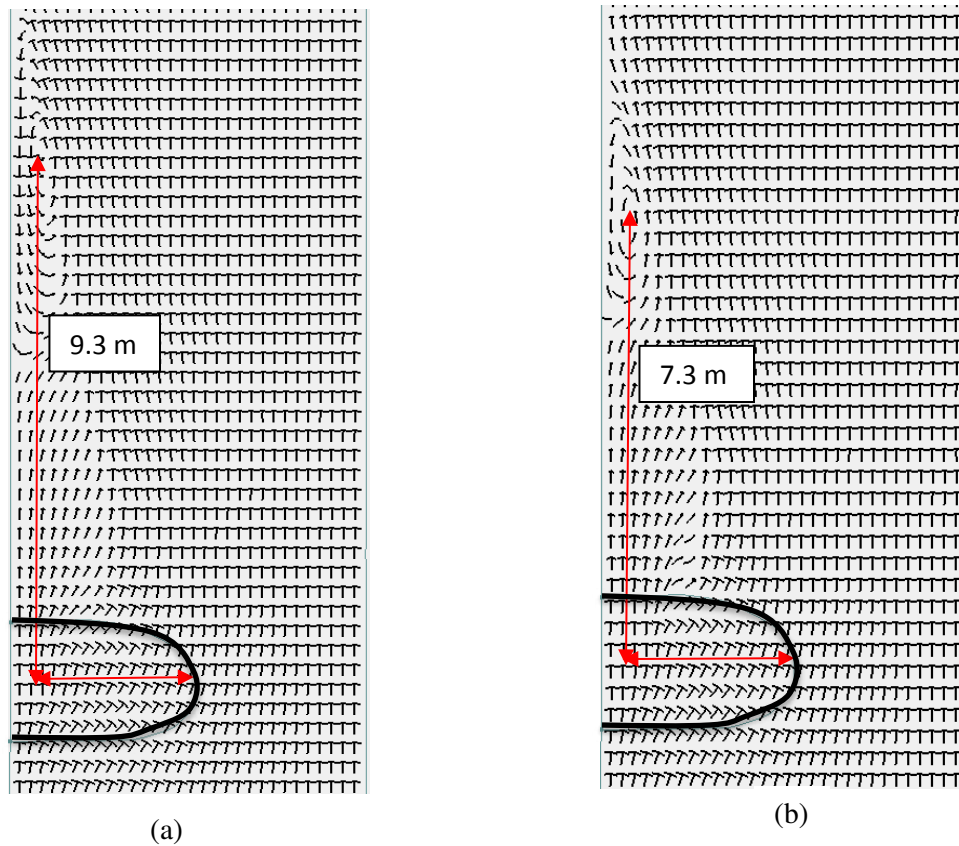


Fig. 31. The velocity vectors when $Y/H = 1.25$: (a) parabolic turbulence model; (b) $k - \epsilon$ turbulence model

Because the parabolic turbulence model was now being selected, another simple independence study was performed to determine an approximate C_t value, which was used to find the turbulent viscosity for the parabolic turbulence model. The recommended flume value of 0.3 (Zey 2017) was compared to 0.9, which was on the upper range of recommended values used, for both submergence ratios. Again, for both flow depths ($Y/H = 1.25$ and 2.0) the $RMSE_L$ and $RMSE_{3D}$ were found comparing SRH-2D DAV to the large scale flume and FLOW-3D DAV. The results are summarized in Table 4 where it was determined that there was not a significant (≤ 0.008 m/s) change between $C_t = 0.3$ and 0.9. It is worthy to note that the difference between $C_t = 0.3$ and $C_t = 0.9$ when $Y/H = 1.25$ was larger than when $Y/H = 2.0$ due

to the more turbulence, and thus more variation in velocity found within the wake of the BW when $Y/H = 1.25$.

Table 4. The RMSE comparing $C_t = 0.3$ to $C_t = 0.9$ for $Y/H = 1.25$ and 2.0

	$Y/H = 1.25$		$Y/H = 2.0$	
	$C_t = 0.3$ (m/s)	$C_t = 0.9$ (m/s)	$C_t = 0.3$ (m/s)	$C_t = 0.3$ (m/s)
RMSE _L	0.048	0.056	0.071	0.071
RMSE _{3D}	0.085	0.091	0.057	0.057

Similar to the comparison of the $k - \epsilon$ and the parabolic turbulence model, the location of the center of the eddy changed between when $C_t = 0.3$ and $C_t = 0.9$. As Fig. 32 displays, when $C_t = 0.3$, the center of the eddy was 3.8m downstream of when $C_t = 0.9$. Again, when $Y/H = 2.0$, SRH-2D did not detect any eddying.

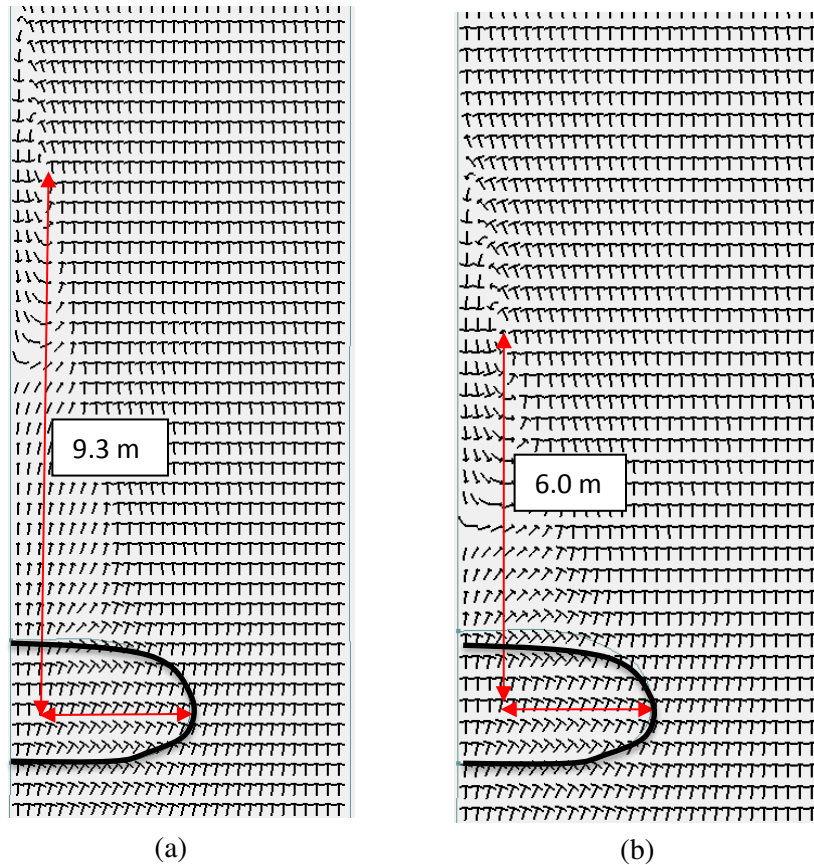


Fig. 32. The velocity vectors when $Y/H = 1.25$ using the parabolic turbulence model: (a) $C_t = 0.3$; (b) $C_t = 0.9$

3.2.11 Use of smooth BW

To test $\alpha = 30^\circ$ and 60° for both submergence ratios, BWs created using CAD had to be implemented due to a lack of information from the hydraulic model. To ensure accuracy, the benchmark experiments, where $\alpha = 90^\circ$ and $Y/H = 1.25$ and 2.0 were used to compare the experiments where the BWs were created in CAD, or “smooth” experiments to the actual LiDAR scanned BWs, or “rough” experiments. First the RMSEs were compared to FLOW-3D DAV and the ADV data from the large-scale flume experiments.

When $Y/H = 1.25$ for the smooth BW, $RMSE_L = 0.063$ m/s and $RMSE_{3D} = 0.081$ m/s and for the rough BW, $RMSE_L = 0.048$ m/s and $RMSE_{3D} = 0.085$ m/s. When $Y/H = 2.0$ for the smooth BW, $RMSE_L = 0.068$ m/s and $RMSE_{3D} = 0.053$ m/s and for the rough BW, $RMSE_L = 0.071$ m/s and $RMSE_{3D} = 0.056$ m/s. The absolute percent difference between the “smooth” and the “rough” BWs when $Y/H = 1.25$ was 9.37% and when $Y/H = 2.0$, the absolute percent difference was 1.60%. The velocities for smooth and rough BWs and commensurate flow depths were also plotted along the “crest” cross section for both $Y/H = 1.25$ and 2.0 in Fig. 34 and Fig. 33 respectively. When $Y/H = 1.25$ (Fig. 34) there was a more significant difference in velocity magnitude between the smooth and the rough BW, more so than when $Y/H = 2.0$ (Fig. 34). However, the percent difference was reasonable between the smooth and rough BWs ($< 10\%$) when $Y/H = 1.25$, so the smooth BWs were used when $\alpha = 30^\circ$ and 60° for $Y/H = 1.25$ and 2.0 .

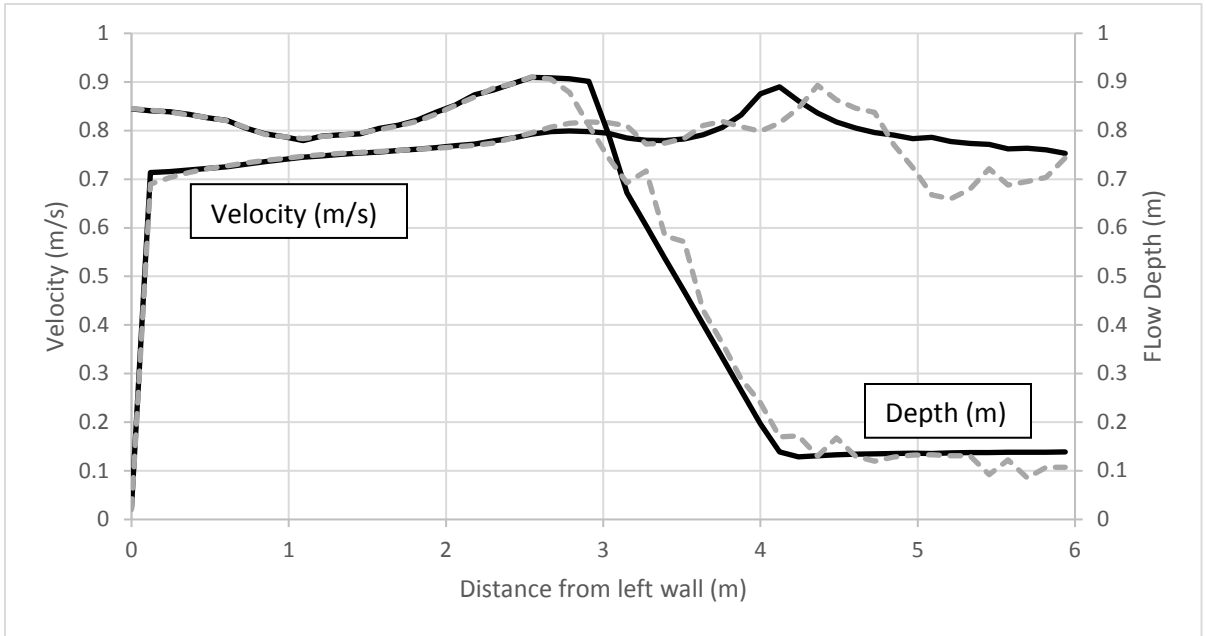


Fig. 33. Comparison of velocity and depth of the smooth BW (black) vs rough (dashed) BW when $Y/H = 1.25$ at the “crest” cross-section

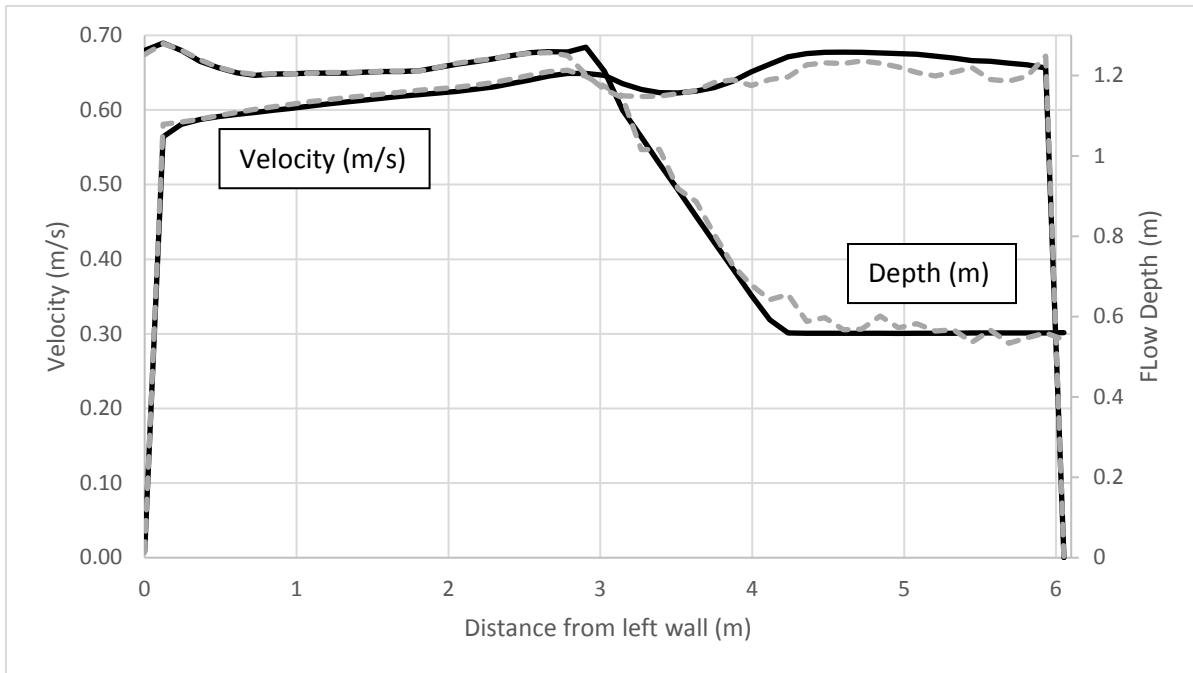


Fig. 34. Comparison of velocity and depth of the smooth BW (black) vs rough (dashed) BW when $Y/H = 2.0$ at the “crest” cross-section

3.4 Flow 3D

FLOW-3D (3-D model) was used as a tool to determine the areas where SRH-2D performed well (replicating flows with suitable accuracy), and where it was lacking in accuracy.

3.4.1 Model Setup

The same LiDAR data used when $Y/H = 1.25$ and 2.0 , $\alpha = 90^\circ$ in the 2-D model were used in the 3-D model so that an accurate comparison to the 2-D model could be made. To get the Lidar data to a reasonable size, the existing Lidar was filtered to 2 cm (0.8 in). These points were then imported to AutoCAD Civil 3D where the point cloud was converted to a surface. This surface was then placed into a positive coordinate system and rotated so that it was facing about 90 degrees (the flume walls weren't straight). The surface elevation was then adjusted so that the elevation values were positive and so that the lowest point was at zero elevation to make the meshing easier within FLOW-3D. The surface was then extruded into two components, the sand and the concrete so that the roughness values could be assigned in FLOW-3D. The roughness height values (k_s) were shown in Fig. 35 where sand was assigned a roughness, $k_s = 3.9$ mm, which was based on $2d_{90}$ (Julien 2010). The flume's cement bottom was set at $k_s = 2$ mm and the cement walls were set at $k_s = 3$ mm (Chow 1959). The BW received the same roughness as the sand, because the mesh elements captured the roughness elements of the BW, so adding roughness less than the height of the 6in rock would not do anything, and adding a roughness height greater than the rock provides unrealistic conditions. Also, according to Seifken (2019), who created design equations for rock vanes using FLOW-3D, the effects of rock vane resistance to flow were characterized by the blockage caused by the rock vanes, rather than their roughness. It was assumed that everything downstream of the concrete was sand, due to the excess of sand deposited in this area as the sand was scoured surrounding the BW. Walls were also created

using the region and extrude commands within AutoCAD Civil 3D so that roughness could also be assigned to them within FLOW-3D.

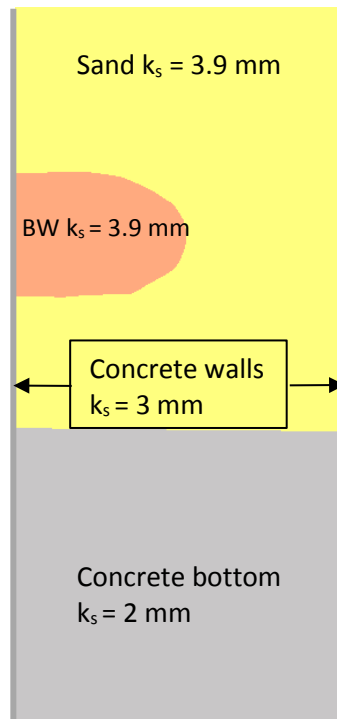


Fig. 35. The roughness values, k_s used in the large flume for FLOW-3D

Mesh dimensions of $x = 0.08$ m (0.26 ft), $x = 0.08$ m (0.26 ft), and $z = 0.04$ m (0.13ft) were selected from about 30 m upstream of the BW to just upstream of the BW. To capture accurate results, around the BW a mesh size of $y = 0.054$ m (0.18 ft), $x = 0.054$ m (0.18 ft), and $z = 0.025$ m (0.08 ft) slightly upstream and about 30 m (98.4 ft) downstream of the BW was chosen to accurately represent the BW's rock and the pitch of the scour hole.

For each of the experiments, the model was run until a steady state condition of flow was established, which was defined as less than a 1% global deviation in total mass, total fluid energy, mass-averaged mean kinetic energy, mass-averaged mean turbulent energy, and mass-averaged turbulent dissipation over a 60-second interval.

A maximum turbulent mixing length (MTML) of 0.027 m was chosen, in accordance with the recommended technique of 7% of the length scale (*FLOW-3D User's Manual* 2008).

The flow depth over the BW as well as the height of the BW were taken into account so that the length scale was the average of these two values and the maximum turbulent mixing length was 7% of this value. It was assumed that there was less turbulence when $Y/H = 2.0$ than when $Y/H = 1.25$, so the MTML determined using the flow depth over the BW when $Y/H = 1.25$ was used for $Y/H = 2.0$.

3.4.2 Mesh Independence

Similar to the 2-D model, three mesh sizes were compared to ensure mesh independence, or that the mesh size did not contribute to significant truncation error within the 3-D model. The mesh size from the end of the concrete to the downstream end of the flume (Fig. 35) of the fine mesh was; x: 0.040 m (0.13 ft), y: 0.040 m (0.13 ft), z: 0.020 m (0.066 ft) with 16.7 million cells, the medium mesh was; x: 0.054 m (0.18 ft), y: 0.054 m (0.18 ft), z: 0.025 m (0.082 ft) with 9.0 million cells, and the coarse mesh was x: 0.074 m (0.24 ft), y: 0.074 m (0.24 ft), z: 0.035 m (0.11 ft) with 3.4 million cells. Each mesh size's velocity magnitude was compared to the large scale flume's velocity magnitude at the locations indicated in Fig. 36. From Table 5 it can be determined that an insignificant change (<0.01 m/s) occurred between each mesh size and therefore the medium mesh size was used with considerations of accuracy and computing time.

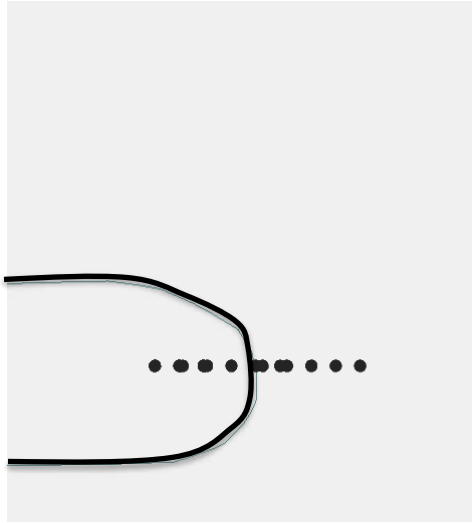


Fig. 36. The locations (in plan view), indicated by the black dots where the large scale flume velocity magnitude data was compared to the velocity magnitude found in FLOW-3D. Note that the velocity was taken at multiple depths

Table 5. The RMSE between the velocity magnitudes of Flow-3D and the large scale flume (RMSE_L) at the locations indicated in Fig. 36

	Fine (m/s)	Medium (m/s)	Coarse (m/s)
RMSE _L	0.137	0.142	0.135

3.5 Experimental Program

The program of numerical and hydraulic-model experiments was designed to display the effects of scour, where pre- and post-scour conditions were compared, on the flow field with a range of orientations and flow depths, while keeping the degree of streamwise blockage the same. The experiments performed included a large-scale physical model experiment (L) to obtain scour morphology using LiDAR and 3-dimensional velocity values from the ADV. All the experiments had the pre- and post-scour conditions from the 2-dimensional numerical model (2) to analyze the effect of scour on the flow field. Experiments 1b, 2b, 3b, 4b, 5b, and 6b have a small scale flume experiment (S) to ensure that as long as the degree of streamwise blockage (L/B) remains the same, the scour does not change significantly between the experiments with

the different orientations (α) and the same degrees submergence (Y/H) so that the same scour morphology can be used for the orientations where no physical model experiments exist ($\alpha = 30^\circ$ and 60°). Experiments 1b and 2b had a 3-dimensional model component to compare areas where the 2-dimensional model was lacking.

The different submergence ratios ($Y/H = 1.25$ and 2.0) were performed to determine how scour, as well as the flow field changed under a range of design flow depths. When $Y/H = 1.25$ the flow was just over the crest of the BW and when $Y/H = 2.0$ the flow was double the depth of the BW.

The degree of streamwise blockage (L/B) was held constant at 0.5 for all experiments to maximize the amount of scour for each degree of submergence.

The values of flow were determined based on selected flow depths ($Y = 0.8$ m, 2.5 ft and 1.2 m, 4.0 ft) and were found using the ratio of bed shear stress to critical shear stress (see Section 3.1 for details).

Table 6. The experimental program of the physical and numerical models. Note that in the Test ID, (2) denotes the use of the 2-dimensional numerical model, (3) denotes the use of the 3-dimensional numerical model, (L) denotes the use of the large scale flume, and (S) denotes the use of the small flume

Test ID	<i>L/B</i>	<i>Y/H</i>	<i>Q</i> (cms, cfs)	α (°)	Scour Condition
1a (2)	0.5	1.25	2.46, 87	90	Pre-Scour
1b (2)	0.5	1.25	2.46, 87	90	Post-Scour
1b (3)	0.5	1.25	2.46, 87	90	Post-Scour
1b (L)	0.5	1.25	2.46, 87	90	Post-Scour
1b (S)	0.5	1.25	0.002, 0.08	90	Post-Scour
2a (2)	0.5	2.00	3.62, 128	90	Pre-Scour
2b (2)	0.5	2.00	3.62, 128	90	Post-Scour
2b (3)	0.5	2.00	3.62, 128	90	Post-Scour
2b (L)	0.5	2.00	3.62, 128	90	Post-Scour
2b (S)	0.5	2.00	0.004, 0.13	90	Post-Scour
3a (2)	0.5	1.25	2.46, 87	60	Pre-Scour
3b (2)	0.5	1.25	2.46, 87	60	Post-Scour
3b (S)	0.5	1.25	0.002, 0.08	60	Post-Scour
4a (2)	0.5	2.00	3.62, 128	60	Pre-Scour
4b (2)	0.5	2.00	3.62, 128	60	Post-Scour
4b (S)	0.5	2.00	0.004, 0.13	60	Post-Scour
5a (2)	0.5	1.25	2.46, 87	30	Pre-Scour
5b (2)	0.5	2	2.46, 87	30	Post-Scour
5b (S)	0.5	2	0.002, 0.08	30	Post-Scour
6a (2)	0.5	1.25	3.62, 128	30	Pre-Scour
6b (2)	0.5	1.25	3.62, 128	30	Pre-Scour
6b (S)	0.5	2	0.004, 0.13	30	Post-Scour

CHAPTER 4: RESULTS & ANALYSIS

This chapter presents the results from the research approaches taken. The main research focused on the flow field at a BW before and after scour. Also included here are the findings from the plate experiment briefly investigating the effects of plate angle on maximum scour depth. A substantial part of the experiments compared values of flow velocity obtained using FLOW-3D to velocities from SRH-2D. This effort sought to determine where the strengths and weaknesses of SRH-2D in simulating flow velocities at a BW. Depth-average velocity values were compared at specific cross sections for pre- and post-scour conditions. The location of the maximum depth average velocity was also compared between the two scour conditions.

4.1 Small Scale Flume

The small scale flume experiment, performed so that the scour from $\alpha = 90^\circ$ could be applied to $\alpha = 30^\circ$ and $\alpha = 60^\circ$, for both $Y/H = 1.25$ and 2.0 in the 2-D model, analyzed the effects of the degree of streamwise blockage (L/B); on the maximum scour depth, the flow field, and scour geometry.

4.1.1 Effects of Degree of Streamwise Blockage on the Flow Field and Scour

The maximum scour depth for the flow condition $Y/H = 1.25$ exceeded that for $Y/H = 2.0$ (Fig. 37). Also shown in Fig. 37, the plate (or BW) orientation for constant transverse blockage did not affect that maximum scour, which was the same conclusion reached by Ettema et al. (2010). Further, the scour geometry did not change significantly between the angles of the two flow depths, with all scour-hole lengths being within a variation of 0.30 m (12 in) to 0.23 m (9 in) as shown in Fig. 38 and the maximum scour depth occurred around the tip of each plate. Observations from the flow field showed flow contraction around the tip of each plate. The

shallower flow, $Y/H = 1.25$, resulted in the greater contraction of the flow because of the plate's lesser degree of submergence and therefore more blockage. Also, a vertical, clockwise vortex formed along the upstream side of the plate and scoured sand from the front of the plate and a lateral eddy in the downstream side of the plate caused by flow separation, which caused scour at the tip and deposition just downstream of the plate, creating the start of the dunes.

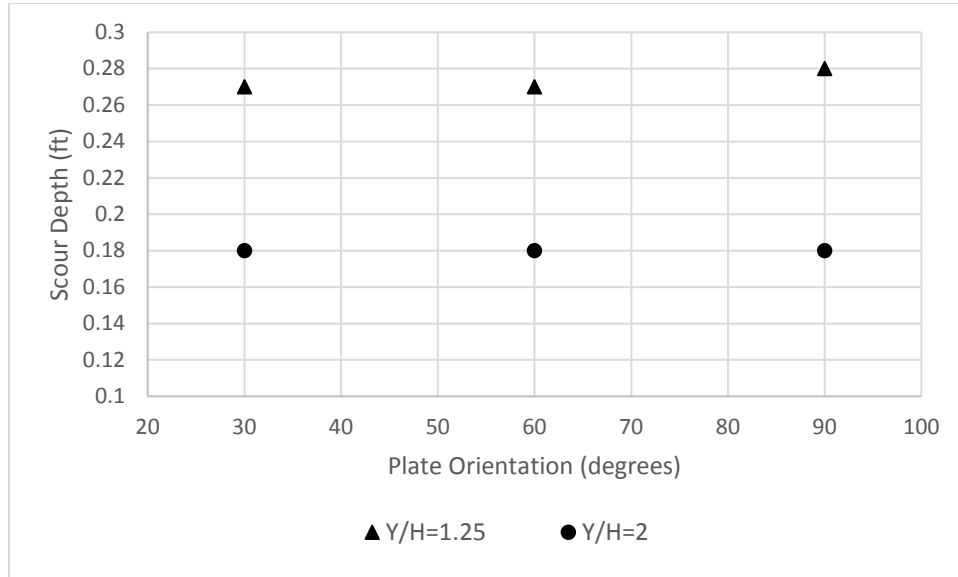
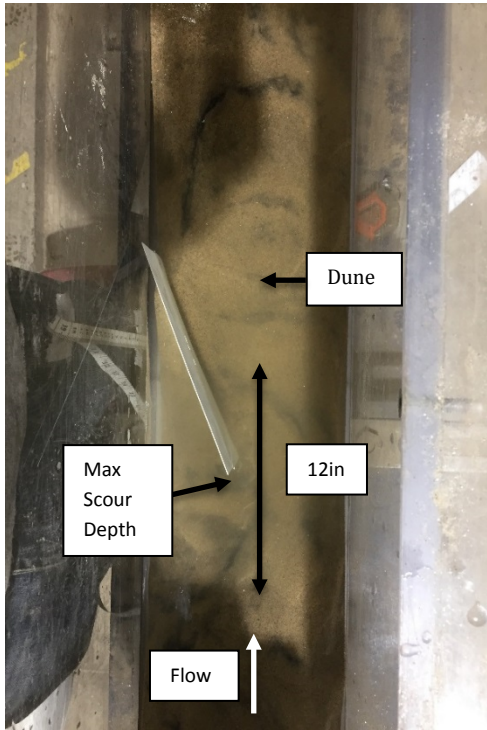
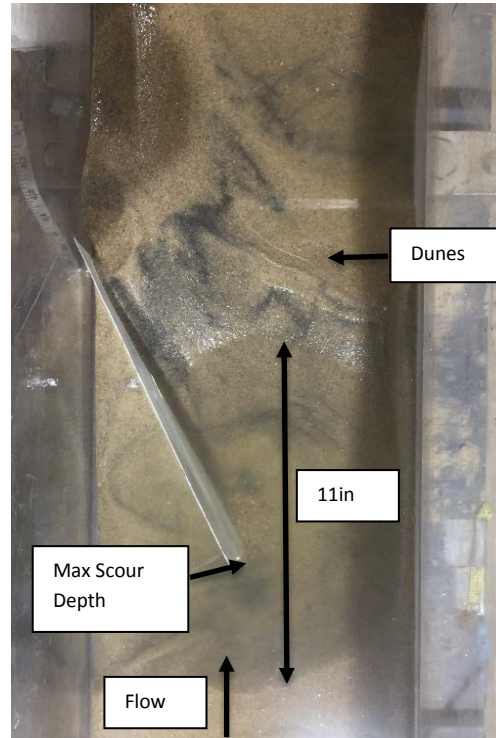


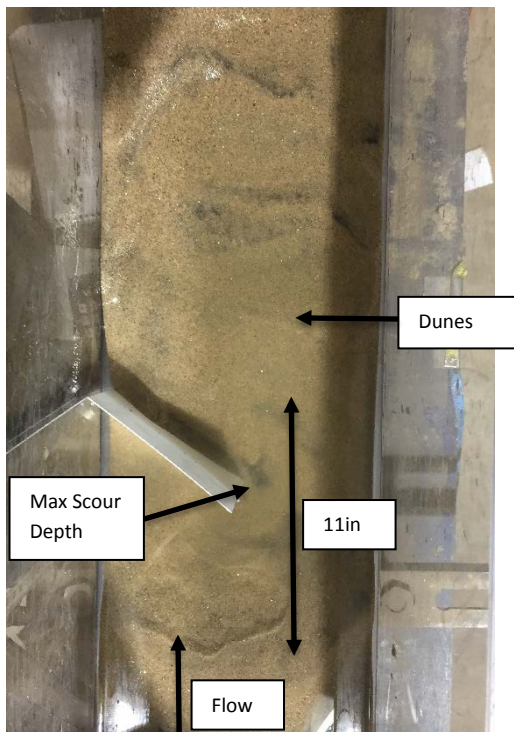
Fig. 37. The scour depth at each plate (BW) for varying orientation when $Y/H = 1.25$ and 2.0 . The bed thickness was 0.10 m (0.33 ft)



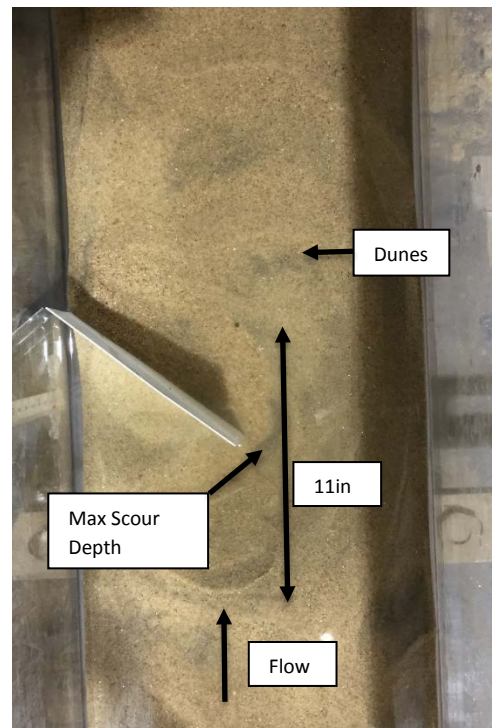
(a)



(b)



(c)



(d)

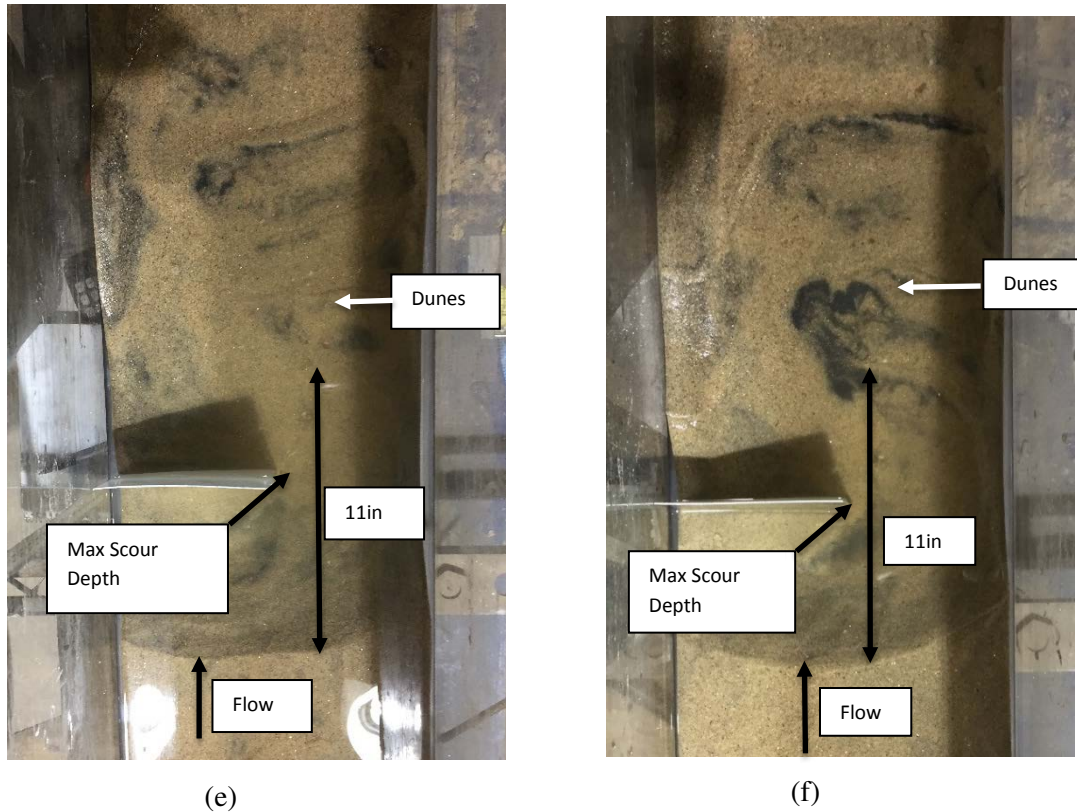


Fig. 38. Overhead views of scour at the plates used to simulate (approximately) bendway weirs: (a) $Y/H = 1.25$, $\alpha = 30^\circ$; (b) $Y/H = 2.0$, $\alpha = 30^\circ$; (c) $Y/H = 1.25$, $\alpha = 60^\circ$; (d) $Y/H = 2.0$, $\alpha = 60^\circ$; (e) $Y/H = 1.25$, $\alpha = 90^\circ$; and, (f) $Y/H = 2.0$, $\alpha = 90^\circ$. The black sand is magnetite (denser and finer than the main sand), and indicator of locations of greater shear stress on the bed

4.1.2 Effects of a flood hydrograph on a BW's stability

Useful insight was obtained from the experiments with the flat plates to show qualitatively the effects of unsteady flow (similar to a flood hydrograph) on the scour behind the plate and subsequent instability caused by it. These effects were magnified by the thinness of the plates (strengthened vortices) and provided insight into the important overtopping case of BWs. The overtopping provided qualitative illustrations of the scouring mechanisms due to the blockage caused by the plate which could be related to the BW. To perform this experiment, the flow depth was adjusted until it was approximately just over the crest of the plate to simulate base flow levels of a BW. A small plate ($H = 2.5$ cm, 1 in, $L = 6.8$ cm, 2.67 in) was then set into

place. The flow was then increased steadily so that the effects of overtopping due to high celerity flow could be observed. Fig. 39 displays the scour over time as the flow was increased.

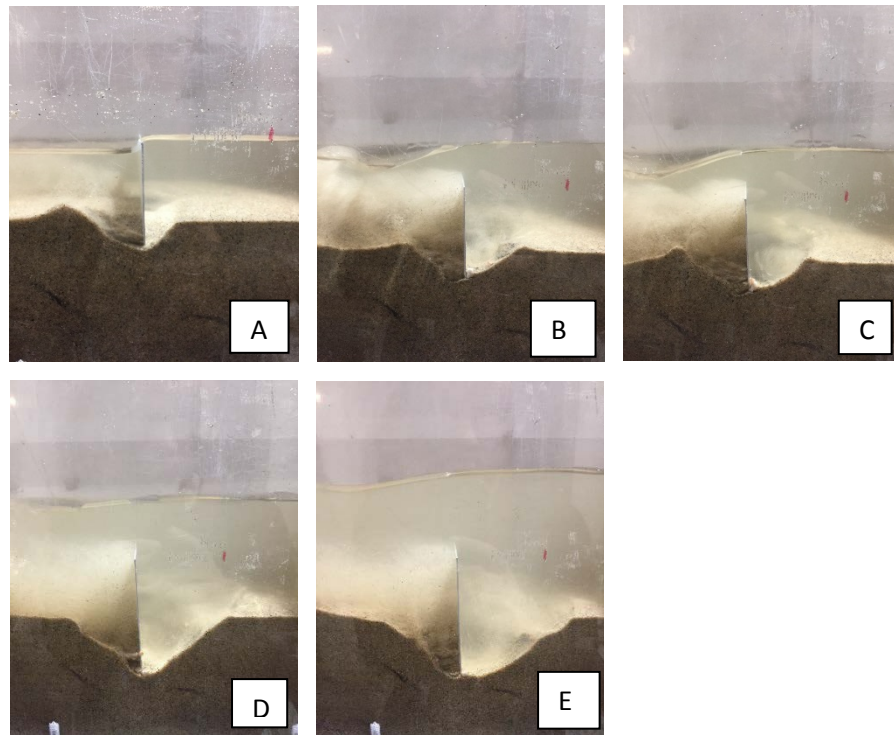


Fig. 39. Shown here is the time development of scour at a plate ($\alpha = 90^\circ$) as the flow stage increased from essentially a baseflow state to a deeper flow associated with the rising limb of a flow hydrograph. The series (a) through (e) show the scour development. The level of turbulence was greater on the downstream side of the plate, and the depth of scour is only slightly less on the downstream side of the plate

4.1.3 Discussion of Plate Experiments

These experiments showed that, with constant transverse blockage, the maximum scour depth and geometry did not change significantly between the plate orientations. Therefore, the same Lidar data obtained from the large-scale experiments in the Tarbela Flume (6.1 m wide) for BW set at $\alpha = 90^\circ$ could be used for the numerical simulations of BWs set at $\alpha = 30^\circ$ and 60° .

The demonstration experiment of a BW exposed to the rising limb of a flood wave emphasizes that the riskiest period for rock forming a BW was on the rising limb of a hydrograph, when the flow condition changes from baseline (Y/H starts to exceed 1) to larger

flows when $Y/H \approx 1.5-1.6$; i.e., Fig. 39a-e. For $Y/H > 1.5-1.6$, flows near the BW back-slope and near the BW front-slope calm somewhat, as flow blockage decreases.

4.2 Flow 3-D

Two experiments were performed using FLOW-3D; $Y/H = 1.25$ and 2.0 , using the post-scour bed geometry, so that the results could be compared to SRH-2D. First the results of FLOW-3D were compared to the hydraulic-model results, to ensure that the model was accurate before comparing the results to results obtained using SRH-2D.

4.2.1 Comparison of FLOW-3D Results to the Hydraulic Model

It is important to note that FLOW-3D takes into consideration the velocity in the z direction in its depth averaged velocity calculations, although in many instances the velocity magnitude was dominated by the x - and y - velocity components, there were areas where the velocity field was dominated by the z -velocity component such as in the wake of the BW and on the side slopes of the BW.

FLOW-3D velocity magnitude values were compared first to the ADV values of velocity magnitude from the hydraulic model. The latter values were taken at the locations indicated in Fig. 40. The comparison in Fig. 41a&b shows that the percent error, estimated between the 3-D model and the hydraulic model, has substantially lower values in the contracted region for $Y/H = 1.25$ and 2.0 than in the wake region of the BW. The highest percent error was in the wake of the BW for both $Y/H = 1.25$ and 2.0 with values of 32% and 88% , respectively. This high percent error when $Y/H = 2.0$ was located close to the wall where the velocities were very small. This was a region where the RNG turbulence model was known to provide substantial error, where the Reynolds number was small (Versteeg & Malalasekera 2007). However, it was expected that the larger percent error values would be within the wake of the BW due to the increased

turbulence caused by vertical and horizontal eddying. With a majority of low values of percent error (being less than 20%) when $Y/H = 1.25$ and 2.0 , the next check regarding the depth-average velocity compared to the depth-average velocity found in SRH-2D. The results of this comparison were couched in terms of the following relationship for velocity magnitude:

$$\text{Percentage Error} = \left(\frac{\text{FLOW-3D DAV} - \text{SRH-2D DAV}}{\text{FLOW-3D DAV}} \right) \left(\frac{100\%}{1} \right) \quad (4.1)$$

Also,

$$\text{Percentage Error} = \left(\frac{\text{physical model VM} - \text{FLOW-3D VM}}{\text{physical model VM}} \right) \left(\frac{100\%}{1} \right) \quad (4.2)$$

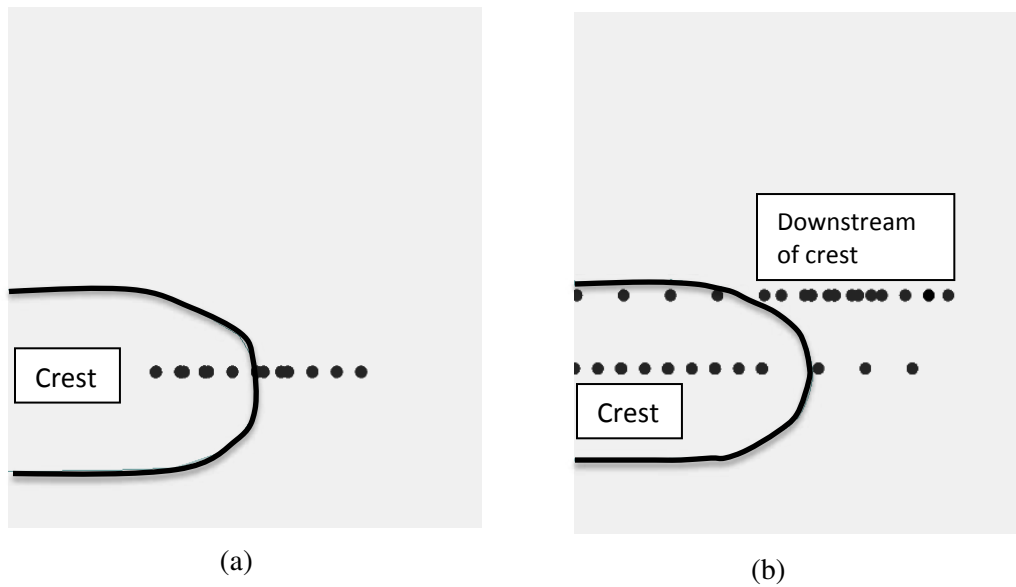
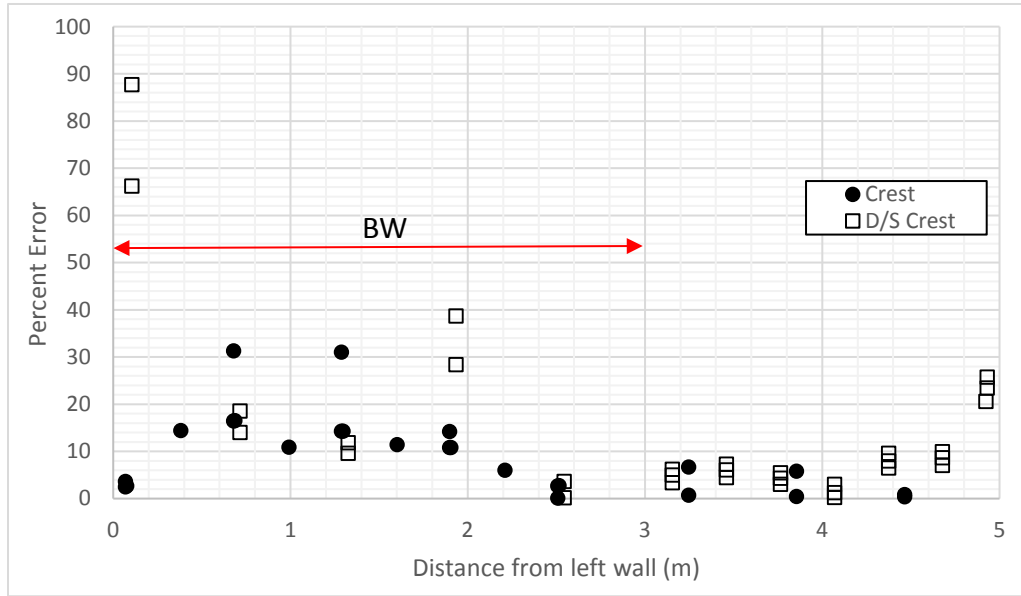
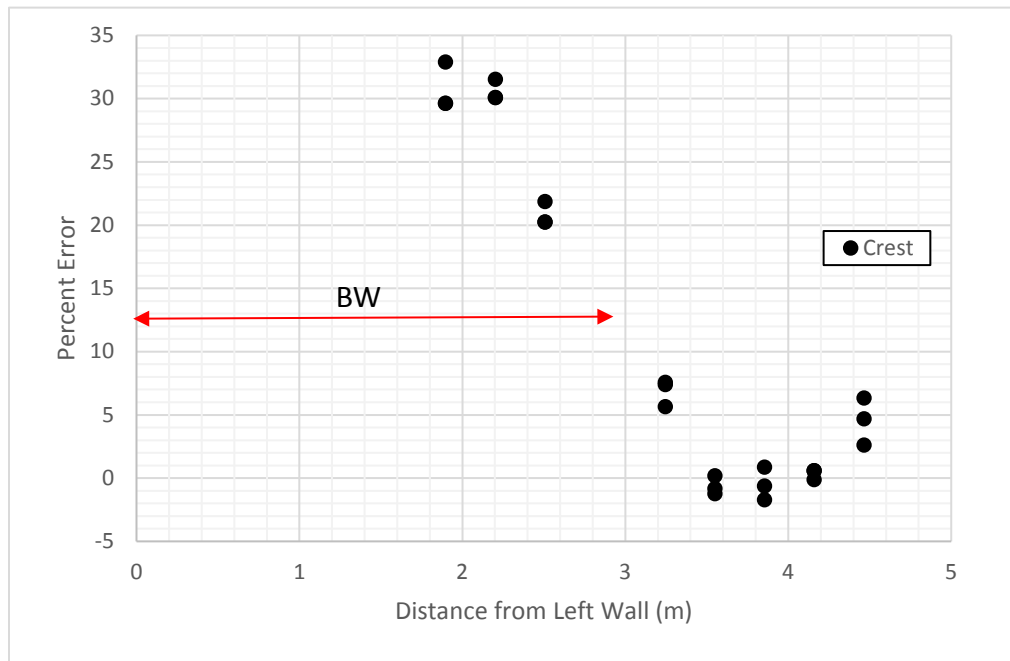


Fig. 40. The location of ADV velocity data that was compared to FLOW-3D velocity magnitude at multiple depth per point at: (a) $Y/H = 1.25$ and (b) $Y/H = 2.0$



(a)



(b)

Fig. 41. Comparison of FLOW-3D velocity magnitude to the velocity magnitude of the physical model data: (a) $Y/H = 1.25$, $\alpha = 90^\circ$; and, (b) $Y/H = 2.0$, $\alpha = 90^\circ$. Here, “Crest” and “D/S Crest” indicates the streamwise location of the comparison as indicated in Fig. 40

4.2.2 Comparison of FLOW-3D Depth Average Velocity to SRH-2D Depth Average Velocity

The FLOW-3D depth-average velocity values were compared to the SRH-2D depth-average velocity values obtained at the cross-sections indicated in Fig. 42. The location of the maximum depth average velocity for both models was determined and displayed in Fig. 46a&b. Also, qualitative figures were used to provide insight into the regions where SRH-2D excelled or lacked (Fig. 43 and Fig. 44). Fig. 45a&b show that percent error, estimated between the 3-D model and the 2-D model, was lower to the right of the BW, or the contracted region, for $Y/H = 1.25$ and 2.0 . The highest percent error was in the wake of the BW for $Y/H = 1.25$ and 2.0 with values of 85% and 26%, respectively. The vertical turbulence on the downstream side of the BW was higher for $Y/H = 1.25$ than for $Y/H = 2.0$ (Fig. 44a&b).

Fig. 43a&b show that there was significantly more turbulence in the wake of the BW when $Y/H = 1.25$ than when $Y/H = 2.0$. Therefore the flow contraction, which is a dominant flow feature, weakens as Y/H increases.

The location and magnitude of the maximum velocity for SRH-2D and Flow-3D (Fig. 46a&b) were significantly closer when $Y/H = 1.25$ than when $Y/H = 2.0$. This outcome occurred because there was more vertical velocity over the BW, when $Y/H = 2.0$, shown in Fig. 47, leading SRH-2D to have a different flow distribution around the BW than actually occurred. When $Y/H = 1.25$, a majority of the flow was directed around the BW due to the increase in submergence and therefore increase in blockage, leading to less flow going over the top of the BW and more realistic results.

The 3-D and 2-D numerical models agree relatively well to the left of the BW, within the contracted region. Fig. 45a&b shows a max percent error of 3% and -13% for $Y/H = 1.25$ and 2.0

respectively within the contraction sub cross-section) due to the likely logarithmic, and low turbulent velocity profile within this section as displayed in Fig. 43a&b.

The 3-D and 2-D models disagree behind the BW, where there were pronounced unsteady turbulence structures (Fig. 43a&b and Fig. 44a&b). Particularly, $Y/H = 1.25$ displayed significantly higher percent differences (max. percent error = 85%) than for $Y/H = 2.0$ (max. percent error = 26%) on the downstream end of the BW (Fig. 45a&b). This likely occurred because of the increased blockage due to the lower flow depth of $Y/H = 1.25$, leading to more turbulence caused by more flow separation as Fig. 43a indicates.

FLOW-3D proved to be a useful tool to validate the SRH-2D results and to display where confidence in its simulations can be assumed and where it was lacking.

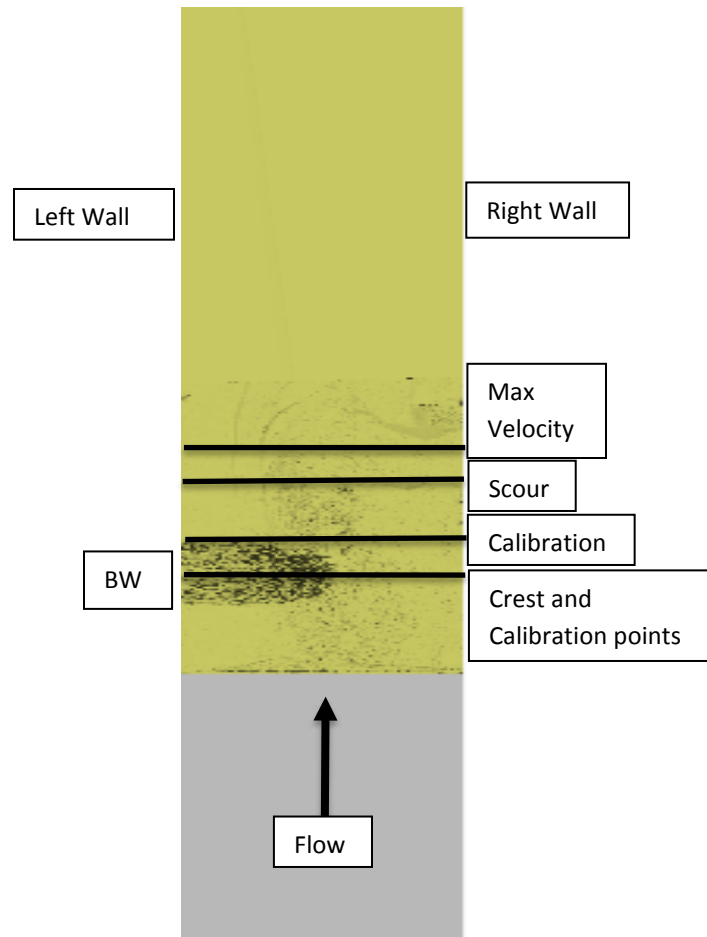


Fig. 42. The flume layout used in the 2D and 3D numerical models, and for the large flume. Indicated are the flow direction, the locations of the left and right walls and the BW. The transects labeled “Crest,” “Calibration Points,” “Scour Hole,” and “Max Velocity” are the locations of comparison of difference between 3-D and 2-D numerical models and the physical model

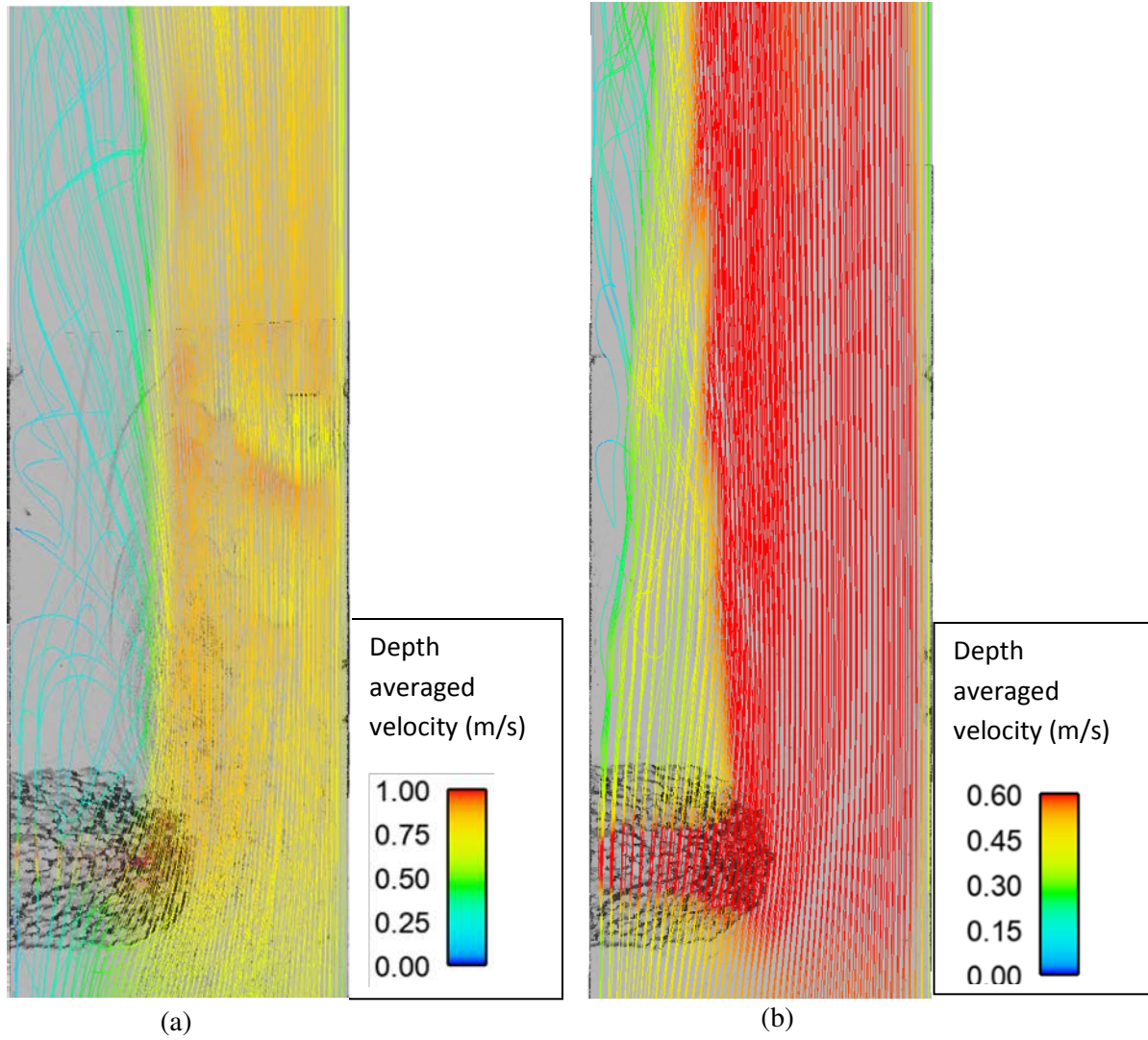
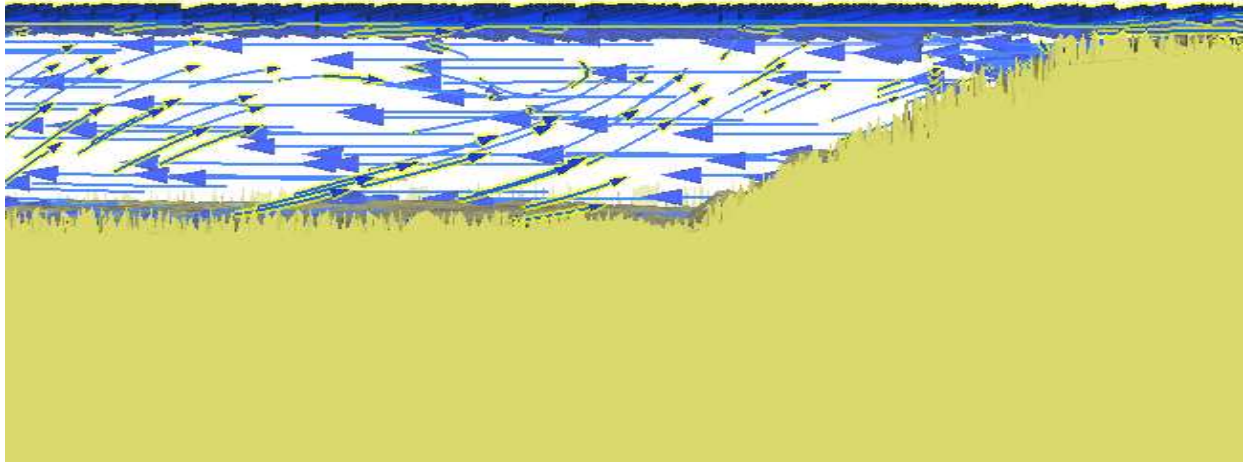
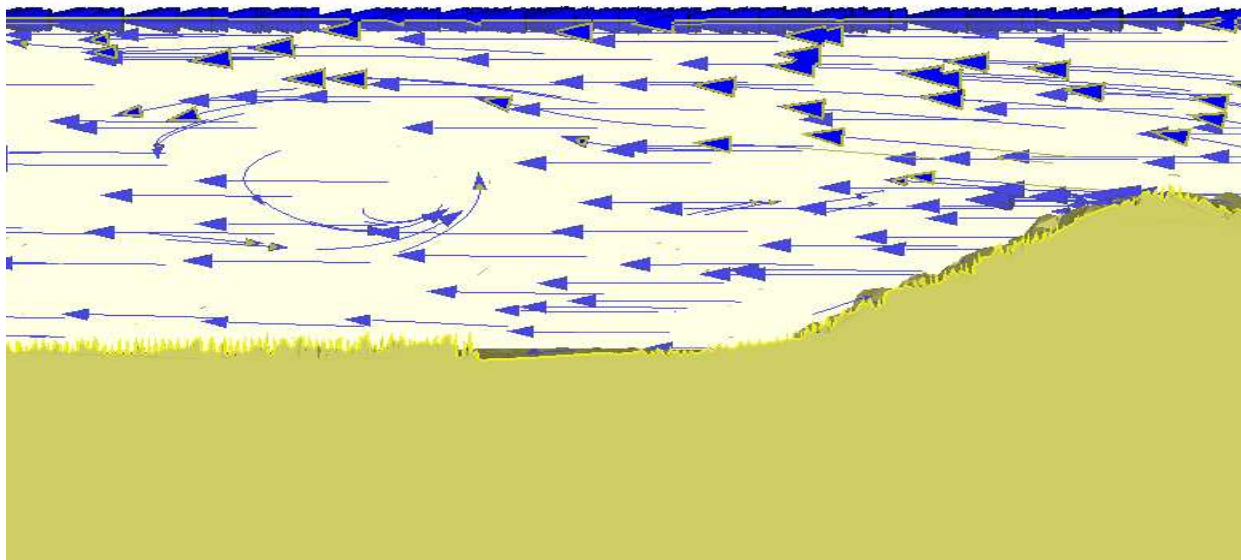


Fig. 43. Flow lines (with velocity contours) at and below the water surface using FLOW-3D: (a) $Y/H = 1.25$, $\alpha = 90^\circ$; and, (b) $Y/H = 2$, $\alpha = 90^\circ$



(a)

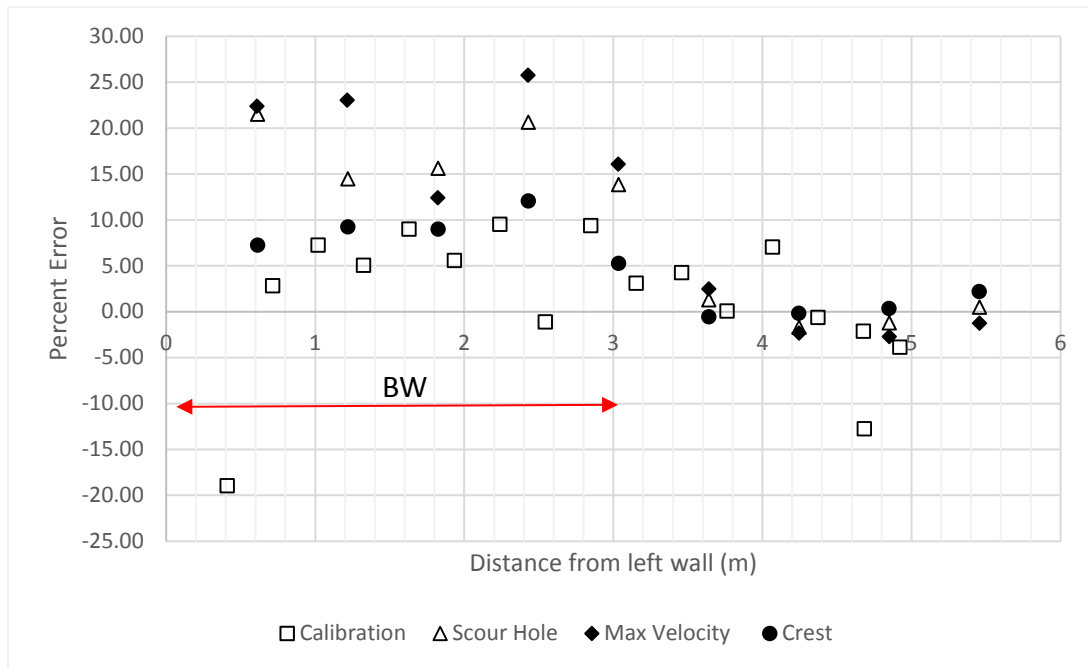


(b)

Fig. 44. FLOW-3D generated velocity vectors in profile view (over vertical plane) at the downstream end of the BW: (a) $Y/H = 1.25$, $\alpha = 90^\circ$; and, b) $Y/H = 2$, $\alpha = 90^\circ$



(a)



(b)

Fig. 45. Comparison of FLOW-3D depth-averaged velocity to SRH-2D depth averaged velocity with “BW” indicating the lateral location of the BW, “calibration points” indicating the location of where SRH-2D depth-averaged velocity was calibrated, “scour hole” indicating the velocity cross section at the max depth of the scour hole, “max velocity” indicating the velocity cross section across the maximum velocity, and “crest” indicating the velocity across the crest: (a) $Y/H = 1.25$, $\alpha = 90^\circ$; and, (b) $Y/H = 2$, $\alpha = 90^\circ$

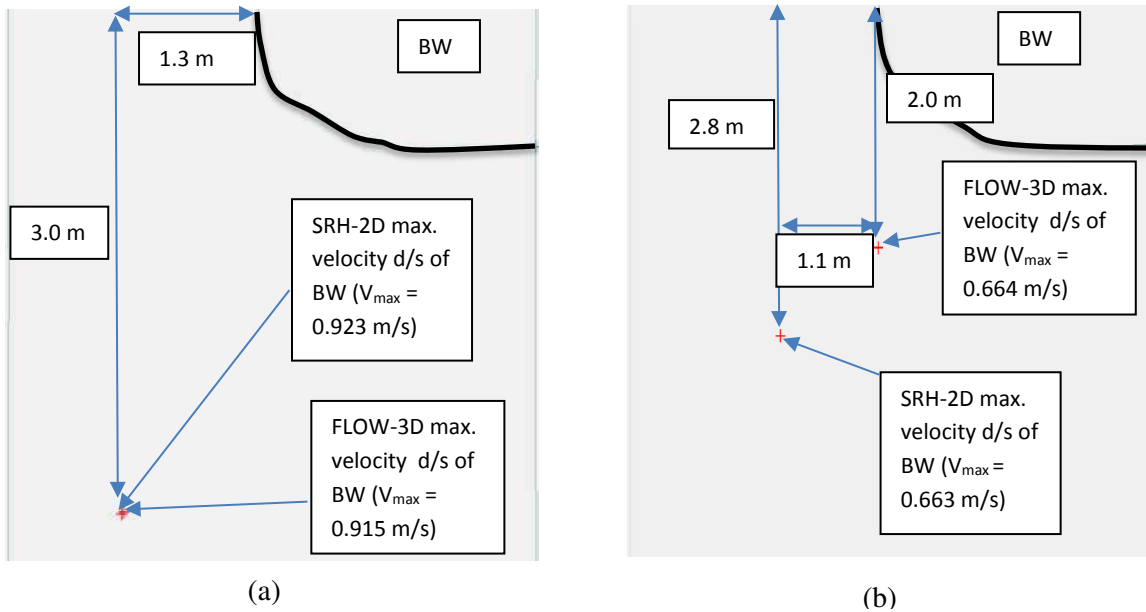


Fig. 46. The locations of the maximum depth averaged velocities from SRH-2D and FLOW-3D: (a) $Y/H = 1.25$, $\alpha = 90^\circ$; and, (b) $Y/H = 2.0$, $\alpha = 90^\circ$

4.2.2 Vertical Velocity Component

Another key insight from FLOW-3D were the regions where the vertical component of velocity was high. This insight could not be obtained using SRH-2D, which gives a depth-averaged simulation of flow. The main region where vertical component was significant was before the crest of the BW, as the flow there began to rise up the slide slope of the BW, as circled in red in Fig. 47a&b. This region was a source of error for SRH-2D, causing a misrepresentation of the flow field. The flow lines were an indicator of this, where when $Y/H = 1.25$, the flow lines were loosely spaced over the crest of the BW and when $Y/H = 2.0$, the flow lines were more tightly spaced, indicating that a higher portion of the flow field was flowing over the BW, which was likely not captured using the 2-D model. This was shown in the roughness sensitivity analysis performed in Section 3.2.5 Manning's n Sensitivity Analysis where the calibrated roughness values found for $Y/H = 2.0$ were larger than when $Y/H = 1.25$,

which one would expect to be smaller because of the lesser effects of resistance to flow due to a deeper flow depth. Therefore, this large vertical velocity is likely to misrepresent the flow field, as obtained using the 2-D model.

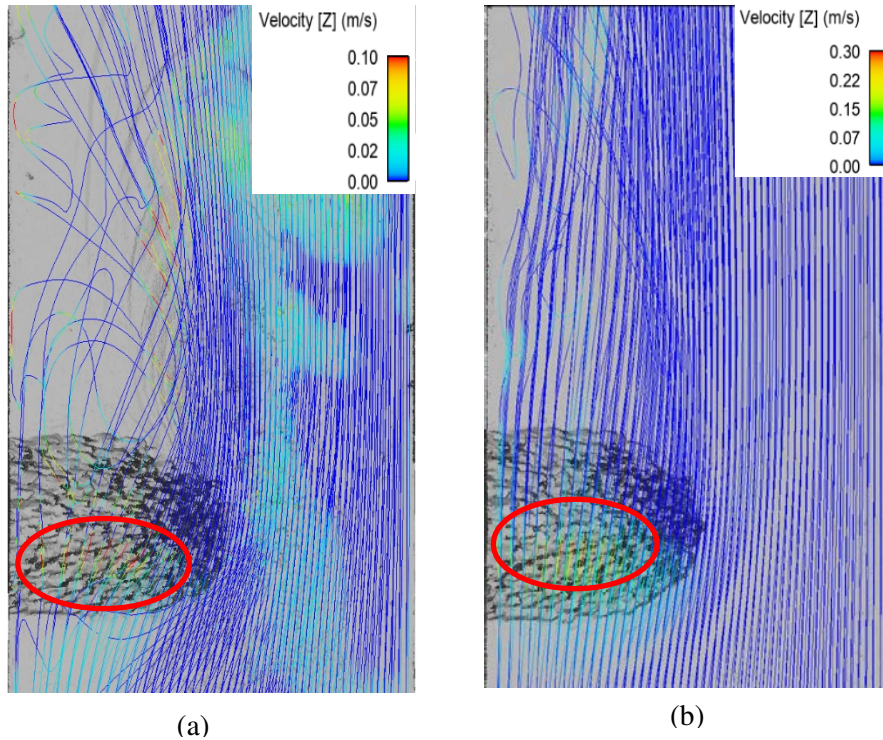


Fig. 47. Equally distributed streamlines with z-velocity contours when $\alpha = 90^\circ$: (a) $Y/H = 1.25$ and (b) $Y/H = 2.0$. Note the larger velocity upstream of the crest, indicated with the red oval and relatedly, the wider spacing of the streamlines between $Y/H = 1.25$ than $Y/H = 2.0$

4.3 Effects of Scour on Flow Parameters when $\alpha = 30^\circ, 60^\circ,$ and 90°

To determine the effects of scour on the velocity field at a BW, experiments were performed at two submergence ratios ($Y/H = 1.25$ and 2.0) and at three different angles ($\alpha = 30^\circ, 60^\circ$ and 90°) the left flume wall (Fig. 49, Fig. 55, and Fig. 61) using SRH-2D for simulations. As the recommended angle for BW deployment varies from $\alpha = 50^\circ$ (Julien & Duncan 2003) to $\alpha = 80^\circ$ (Lagasse et al. 2009), it was deemed important to understand the

effects of scour encompassing these values of BW angle. Values of α (30° , 60° and 90°) extended between the BW crest and the adjoining or left bank.

It should be mentioned that in reality, there are many different values of parameters that can be used in the field. The bend radius, BW side slope, BW height, BW angle, and degree of blockage will all play a role on the flow field (Julien & Duncan 2003). Therefore the results of the effect of scour on the flow field are preliminary to determine if there is an effect of scour on the flow field, holding these parameters, except the BW angle, constant.

The experiments compared the pre-scour versus post-scour depth-average velocity and unit discharge at the specified cross sections shown in Fig. 48 to obtain a better understanding of the effects of scour on the general flow field.

The location and magnitude of the maximum velocity close to the BW were determined as they are useful variables for understanding the effects of scour on the flow field at a BW. The maximum velocity is indicative of the location of the channel thalweg position near the BW. This variable indicates the effectiveness of the BW in defining the thalweg location and (to some extent) decreasing bank erosion. Over time, scour causes the thalweg to shift.

The X_{\max} , or the distance of the maximum velocity magnitude from the tip of the BW in the lateral direction, quantifies the effects of scour on the thalweg location, whereas Y_{\max} , or the distance of the maximum velocity magnitude from the tip of the BW in the streamwise direction was a simple indicator of the physical effects of the scour on the flow field. As Fig. 48 indicates, the location of the maximum velocity was controlled by the formation of a vena contracta, where the flow lines were the narrowest. This location is slightly downstream of the BW, rather than at the BW tip. It is also important to note that V_{\max} is the velocity within the sand bed, not the maximum velocity in the channel. In the experiments, except for $Y/H = 2.0$, $\alpha = 30^\circ$ the

maximum velocity occurred in the crest region of the BW, where the flow is substantially contracted vertically, which also occurred in the study previously mentioned by Abad et al (2008) during the medium and high stage of the flow over a series of BWs.

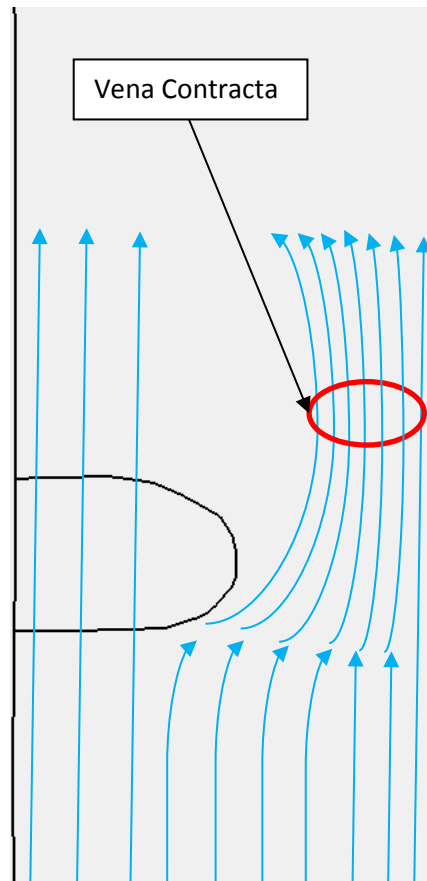


Fig. 48. A schematic of the flow around the BW, where the vena contracta indicates the region of maximum velocity. Note that this schematic doesn't account for the turbulence in the wake of the BW

The transverse variation of unit discharge was also investigated, as this variable takes into consideration the depth and the velocity, which can be indicative of regions that will experience more scour, where the velocity and depth increase.

4.3.1 Effect of Scour on Velocity Field when $Y/H = 1.25$ and 2.0 , $\alpha = 30^\circ$

It is important to mention first that, for both submergence ratios of BW, the numerically simulated BW had to be moved marginally closer to the left wall, thus affecting the degree of blockage (L/B , for a give flow depth of approach flow). This is to ensure that the BWs were

adjusted within the scour hole region appropriately, so that the BW did not stick out into the scour hole region unrealistically far. When $Y/H = 1.25$, $L/B = 0.48$, and when $Y/H = 2.0$, $L/B = 0.45$ for both the pre-scour and post-scour experiments.

The scour experiment when $Y/H = 1.25$ had a larger effect on the flow field and velocity around the BW than when $Y/H = 2.0$. This trend was due to the larger amount of scour when $Y/H = 1.25$ (about 0.18 m, 7.0 in), and relatedly the greater blockage of the approach flow. Refer to Appendix A for an in depth look at the velocity field.

For $Y/H = 1.25$ and 2.0, Table 7 and Table 8 show that the scour does not affect the approach flow upstream of the BW. The difference between the pre- and post-scour average sub cross section velocity when $Y/H = 1.25$ was 0.78% and when $Y/H = 2.0$ was 0.16%. Therefore, most changes in the flow field occur downstream of the BW, where scour-depth is greatest.

The scour location and depth affected equilibrium flow-field velocity. When $Y/H = 1.25$, a 11% and 15% decrease in velocity between the bed to the crest (going horizontal to the flow) for the pre- and post-scour condition occurred, respectively (Fig. 50). When $Y/H = 2.0$ both the pre- and post-scour conditions saw a minimal change in velocity from the bed to the crest (going horizontal to the flow) with a 3% increase in average velocity for both pre-scour and post-scour (Fig. 51). As Table 7 and Table 8 indicate, there was a 5% and 0.6% increase between the crest pre-scour and post-scour average velocity, for $Y/H = 1.25$ and 2.0, respectively. Therefore, when $\alpha = 30^\circ$, scour had little effect on the crest region, although there was a slightly more significant change when $Y/H = 1.25$.

As indicated in Table 7, scour decreased the depth-average velocity at the BW tip when $Y/H = 1.25$ by about 8%. However, when $Y/H = 2.0$ (Table 8), there was only a 0.4% increase in velocity at the tip between the pre- and post-scour condition. The velocity at the tip of the BW

dictates the stability of it, so when $Y/H = 1.25$, the scour would create more stable conditions, but when $Y/H = 2.0$, there would not be a noticeable difference in stability.

Within the wake of the BW, SRH-2D did not simulate eddying as indicated in Fig. 67 and Fig. 68. However, there was a significant decrease in velocity between the crest and downstream of the BW when $Y/H = 1.25$ for the pre- and post-scour conditions. There was a 115% decrease for the pre- and post-scour conditions, based on Fig. 50. When $Y/H = 2.0$, the difference in depth average velocity between the crest of the BW and the wake of the BW was 18% and 20% for the pre-scour and post-scour conditions, respectively based on Fig. 51. The difference between the pre-scour and post-scour average velocity, in the wake of BW sub-cross section when $Y/H = 1.25$ decreased by 5% (Table 7). This small difference was likely attributable to more energy dissipation in the wake of the BW during the pre-scour experiment, due to higher velocity in the contracted region, thus causing a larger difference between the velocity of the wake and the contracted section, separated by the shear layer, and causing more mixing of momentum and therefore an increase of turbulence. When $Y/H = 2.0$, scour caused a 2% increase in velocity (Table 8). This insignificant change in velocity was due to the shallow scour hole and as the lower effect that the BWs blockage plays on the flow due to the deeper flow depth. Hence scour caused large changes in the wake of the BW when $Y/H = 1.25$.

The difference in average velocity magnitude across the contracted sub cross-sections for pre- and post-scour, when $Y/H = 1.25$ and 2.0, was an increase of 11% and 1%, respectively (Table 7 and Table 8). The larger difference in velocity between pre- and post-scour when $Y/H = 1.25$ was due to the shift in maximum velocity to the right when during the post-scour condition. This increase in velocity as well as shift in velocity magnitude in the contraction sub cross-section can be seen in Fig. 52, where the difference in velocity between pre-scour and post-

scour was found for the entire model domain. The largest difference in velocity was in the contracted region, towards the right wall more so for $Y/H = 1.25$, but it was still evident when $Y/H = 2.0$.

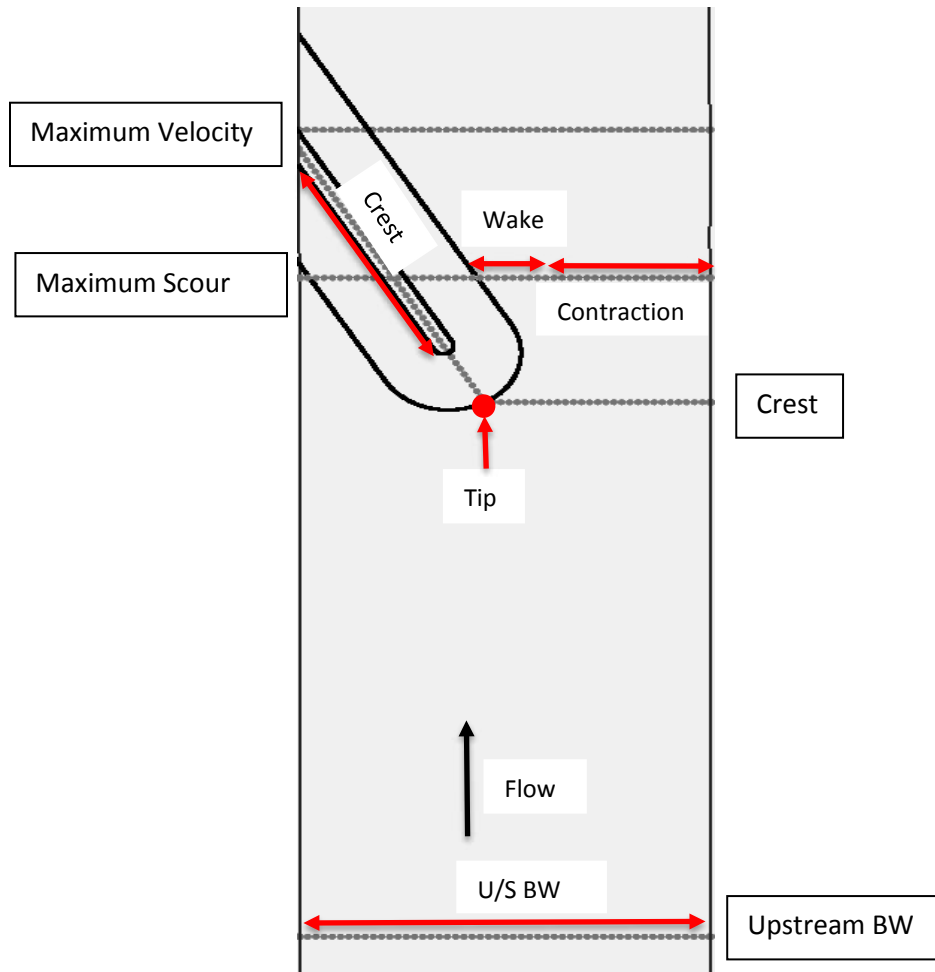
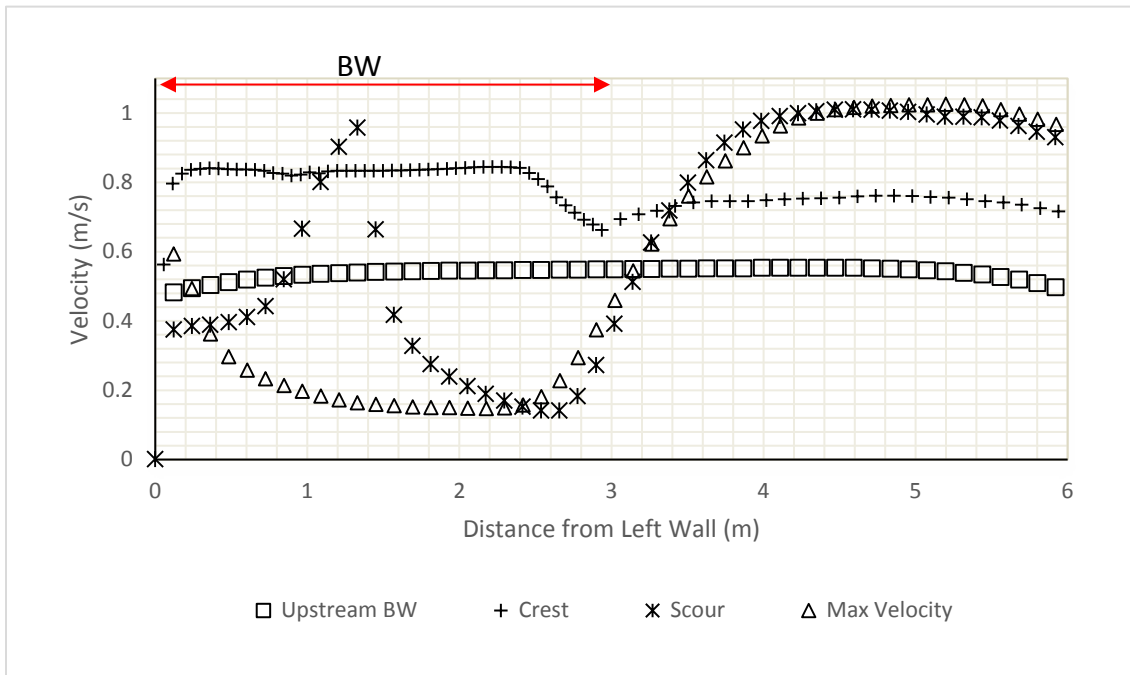


Fig. 49. The approximate locations of the cross sections where data was collected when $Y/H = 1.25$ and 2.0 . Shown here are the positions of the four cross-sections along which velocity and unit discharge distributions were determined. The max.-velocity section includes the region where flow velocity was greatest; the scour-hole section transected the max-depth of the scour hole, which extended downstream and upstream from the toe of the BW and the BW center transected the BW as opposed to the BW crest which only went along the BW crest. Note that the location of the maximum velocity cross section varied between $Y/H = 1.25$ and 2.0 .

The red arrows indicate the sub cross-sections that were analyzed for average velocity. The upstream BW sub-cross section included all of the values within the upstream BW cross section, the Contraction sub-cross section included the average velocity and unit discharge values from Maximum Scour cross section, the Crest sub-cross section included values from the Crest cross section, and the Wake of BW cross section included velocity values from the Maximum Velocity cross section



(a)



(b)

Fig. 50. Velocity distribution when $Y/H = 1.25$ experiment along the four cross-sections indicated in Fig. 49: (a) pre-scour; and; (b) post-scour. Notes: the cross-section labelled “Upstream of BW” is the “Section upstream of BW” cross-section; “Crest” is the “BW crest” cross-section, “BW” is the “BW center” cross-section; “max velocity” refers to the “max-velocity section” cross-section; and, “scour” refers to the “scour-hole section” cross-section in Fig. 49



(a)



(b)

Fig. 51. Velocity magnitude distribution when $Y/H = 2.0$ along the four cross-sections indicated in Fig. 49: (a) pre-scour; and; (b) post-scour

Table 7. The average velocity percent difference between pre-scour and post-scour at sub-cross sections, indicated in Fig. 49 when $Y/H = 1.25$ (a positive difference indicates a decrease between pre-scour and post scour conditions and vice versa)

Sub-Cross Section	% Difference
Upstream BW	0.78
Crest	4.47
Contraction	8.34
Wake of BW	10.80
Tip	4.59

Table 8. The average velocity percent difference between pre-scour and post-scour at sub-cross sections, indicated in Fig. 49 when $Y/H = 2.0$ (a positive difference indicates a decrease between pre-scour and post scour conditions and vice versa)

Sub-Cross Section	% Difference
Upstream BW	0.16
Crest	0.56
Tip	-0.40
Contraction	1.46
Wake of BW	2.13

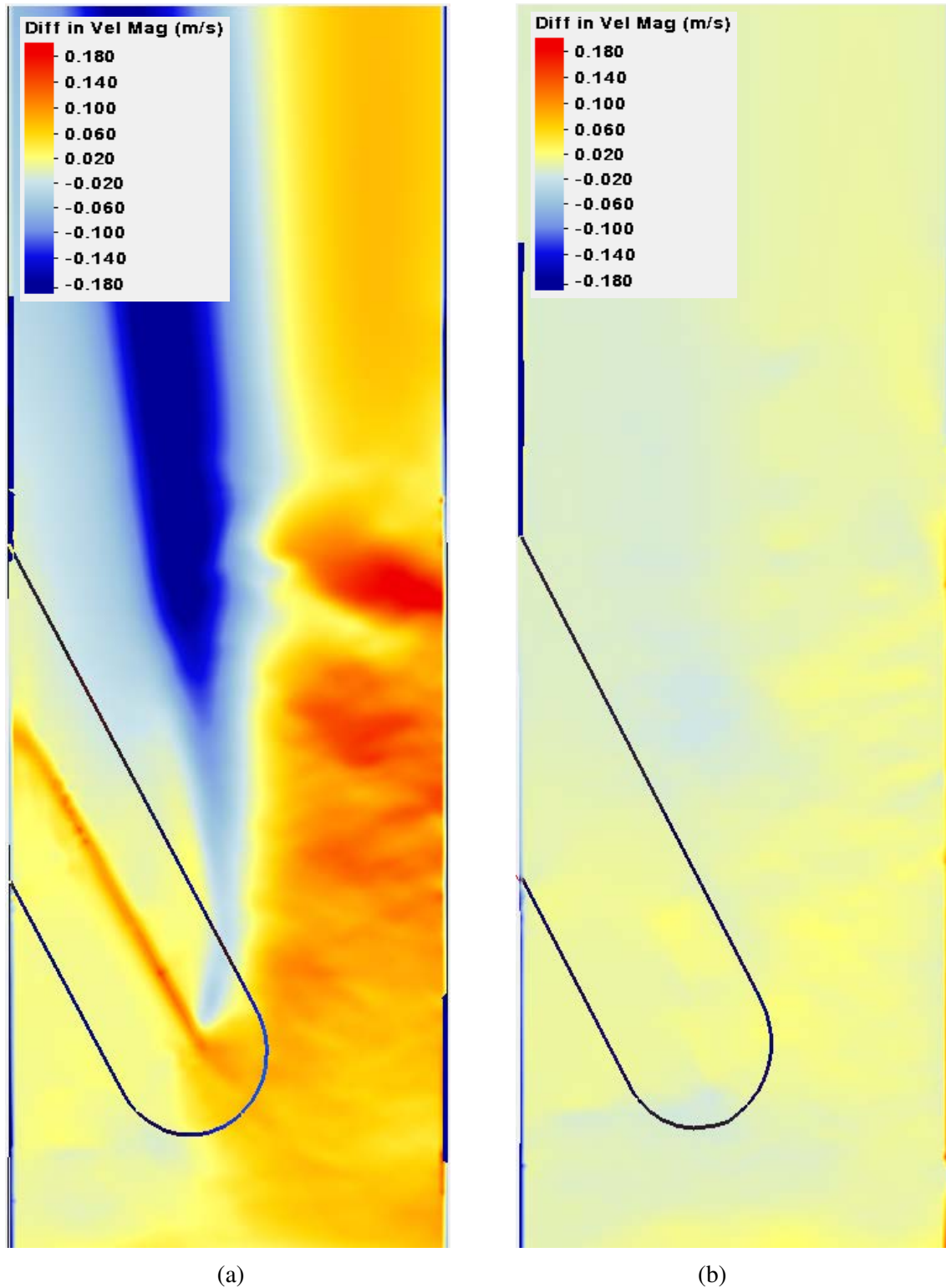


Fig. 52. Depth-average velocity magnitude difference between the pre-scour and post-scour conditions for: (a) $Y/H = 1.25$; and; (b) $Y/H = 2.0$. Red (positive) indicates a decrease between pre- and post-scour and blue (negative) indicates an increase between pre- and post-scour

4.3.2 Effect of Scour on Maximum Velocity when $Y/H = 1.25$ and 2.0 , $\alpha = 30^\circ$

The location and magnitude of the maximum velocity, V_{\max} near the BW during the pre-scour and post-scour conditions for $Y/H = 1.25$ and 2.0 were shown in Fig. 53a&b and Fig. 54a&b. The magnitude of the maximum velocity when $Y/H = 1.25$ decreased from 1.03 m/s (pre-scour) to 0.98 m/s (post-scour) which was a 5% decrease (Fig. 54a&b). The maximum velocity magnitude when $Y/H = 2.0$ remained relatively constant between the pre- and post-scour conditions, with values of 0.68 m/s (pre-scour) and 0.67 m/s (post-scour) or a 1.5% decrease in the velocity magnitude (Fig. 54). Therefore, scour caused a larger decrease in maximum velocity between the pre- and post-scour conditions when $Y/H = 1.25$. This change was due to the about 6 in (0.150 m) increase in maximum scour depth between the $Y/H = 1.25$ and $Y/H = 2.0$. This increase when $\alpha = 30^\circ$ caused the BW to have a more significant effect on the shallower flow field. Though the difference between the pre-scour and post-scour velocity was not largely significant when $Y/H = 1.25$.

The maximum velocity when $Y/H = 1.25$ (Fig. 53a&b) was farther downstream for both the pre- and post-scour conditions, where $Y_{\max} = 5.09$ m and 6.28 m respectively than when $Y/H = 2.0$ (Fig. 54a&b) where $Y_{\max} = 5.1$ m and 4.0 m, respectively. This result was likely due to the lesser effects of blockage when $Y/H = 2.0$. With similar degrees of blockage (L/B) the blockage and roughness of the angled BW should have a more substantial effect on the velocity, when $Y/H = 1.25$ where flow can accelerate more readily out of the contraction when $Y/H = 2.0$ than when $Y/H = 1.25$, thus leading to the maximum velocity being farther downstream of the BW when $Y/H = 2.0$. It was also seen that the post-scour conditions when $Y/H = 1.25$ causes the flow to reach its maximum velocity farther downstream than the pre-scour conditions, which was likely due to the deeper flow depth caused by the scour, meaning that the degree of blockage

decreases for the post scour condition and the flow can more readily accelerate out of the BW tip region. However, when $Y/H = 2.0$, the scour causes the location of the maximum velocity to be farther upstream than the pre-scour condition.

The location of the maximum velocity when $Y/H = 1.25$ for pre-scour and post-scour ($X_{\max} = 2.30$ m and 1.90 m, respectively) and when $Y/H = 2.0$ for pre-scour and post scour ($X_{\max} = 2.13$ m and 1.80 m respectively) shifted closer to the flume's left wall for the post-scour condition (Fig. 53 & Fig. 54). This was likely because flow generally converges at the deepest location, in accordance with the old adage "Depth attracts flow!" The opposite result occurred when $\alpha = 60^\circ$ and 90° , which indicates that this orientation does not obstruct the flow as substantially as these experiments and thus it does not force the vena contracta farther to the flume's right wall. Instead the flow was pulled closer to the scour hole, indicating that this orientation is likely less effective at preventing outer bank erosion.

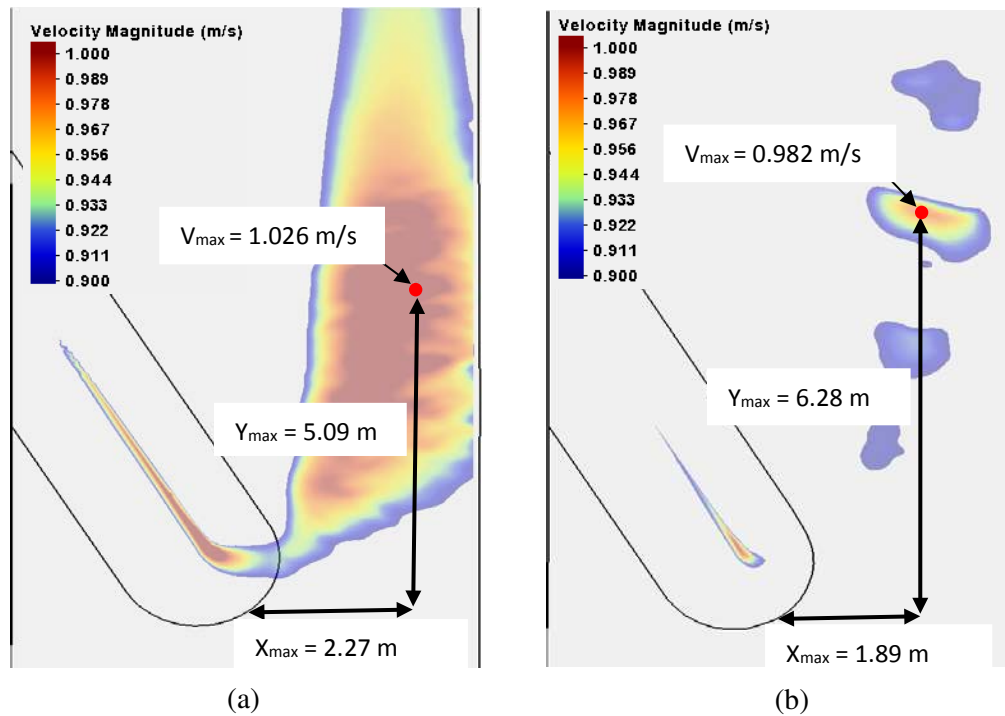


Fig. 53. The location (X_{\max} and Y_{\max}) and magnitude of the maximum velocity (V_{\max}) for $Y/H = 1.25$; (a) pre-scour, (b) post-scour

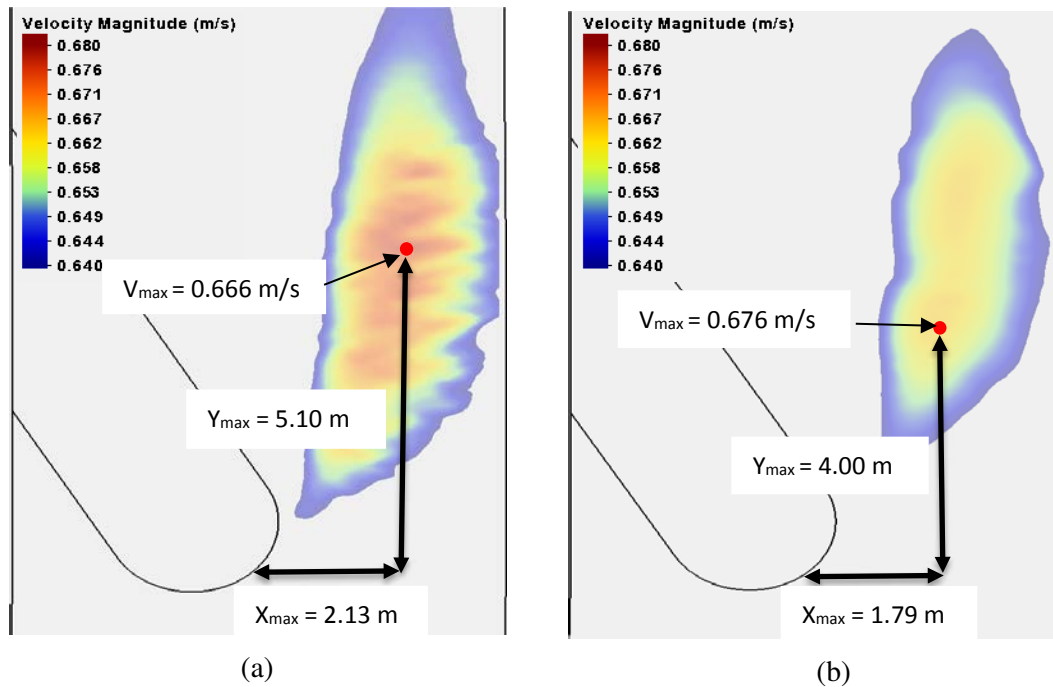


Fig. 54. The location (X_{max} and Y_{max}) and magnitude of the maximum velocity (V_{max}) for $Y/H = 2.0$; (a) pre-scour, (b) post-scour

4.3.3 Effect of Scour on Unit Discharge when $Y/H = 1.25$ and 2.0 , $\alpha = 30^\circ$

Fig. 73 & Fig. 74 (Appendix A) indicate that there was not a significant difference between the pre-scour and post-scour unit discharges when $Y/H = 1.25$ and 2.0 . When $Y/H = 1.25$ there was a larger difference between the pre-scour and post-scour, but not significantly. When $Y/H = 1.25$, the Upstream BW sub cross section saw an increase in average unit discharge of 0.77% and 0.44% when $Y/H = 1.25$ (Table 9) and 2.0 (Table 10), respectively, which was an almost identical increase to the velocity, meaning that the depth increased similarly to the velocity between the pre-scour and post-scour conditions.

The difference in the Crest sub-cross section average unit discharge was a decrease of 2% and an increase of 0.95% when $Y/H = 1.25$ (Table 9) and 2.0 (Table 10) respectively. The lower change in unit discharge between the pre-scour and post-scour when $Y/H = 1.25$ than when $Y/H = 2.0$ was likely because, although there was an increase in velocity over the crest between the

pre-scour condition, there was a deeper flow depth over the crest during the post-scour condition, thus balancing out its lower velocity. This can be seen using the specific energy diagram, where when subcritical flow goes over a hump (such as a BW) the flow loses energy, and therefore decreases in flow depth, and the decrease will be larger when the velocity was higher, where in this case it would be the pre-scour condition.

The contraction sub cross section average unit discharge saw an decrease between the pre-scour and post-scour conditions of 2% and 1% for $Y/H = 1.25$ (Table 9) and 2.0 (Table 10) respectively. Therefore, within this region, the depth increased fairly proportionally to the velocity from the pre-scour to the post-scour experiments, which caused an insignificant increase in unit discharge.

In the wake of BW sub-cross section, the average unit discharge decreased by 1% when $Y/H = 1.25$ (Table 9) between the pre-scour and post-scour whereas the unit discharge increased between the pre- and post-scour by 0.4% when $Y/H = 2.0$ (Table 10). This increase in unit discharge when $Y/H = 2.0$ was due to the significant decrease in velocity between the pre-scour and post-scour conditions, which was discussed previously in section 4.3.1.

Appendix B contains an in-depth analysis of the unit discharge at several cross sections close to the BW.

Table 9. The average unit discharge percent difference between pre- and post-scour conditions at sub-cross sections indicated in Fig. 49 when $Y/H = 1.25$ (a positive difference indicates a decrease between pre-scour and post scour conditions and vice versa)

Location	% difference
Upstream BW	0.77
Crest	2.08
Contraction	1.97
Wake of BW	1.09

Table 10. The average unit discharge percent difference between pre- and post-scour conditions at sub-cross sections indicated in Fig. 49 when $Y/H = 1.25$ (a positive difference indicates a decrease between pre-scour and post scour conditions and vice versa)

Location	% difference
Upstream BW	0.44
Crest	-0.95
Contraction	1.15
Wake of BW	-0.41

4.3.4 Effect of Scour on Velocity Field when $Y/H = 1.25$ and 2.0 , $\alpha = 60^\circ$

Similar to when $\alpha = 30^\circ$, scour for the condition $Y/H = 1.25$ had a larger effect on the flow field and velocity than scour when $Y/H = 2.0$. This trend was due to the deeper scour when $Y/H=1.25$ (about 0.18 m, 7.0 in), and relatedly the greater blockage of the approach flow. The differences in the flow fields can be seen in Appendix A.

For $Y/H = 1.25$ and 2.0 , it is evident from Table 11 and Table 12, that the scour does not affect upstream of the BW velocity in the Upstream sub cross-sections where Fig. 55 indicates the location of each sub-cross section. The difference between the pre-scour and post scour average sub cross section velocity when $Y/H = 1.25$ was 1.8% and when $Y/H = 2.0$ was 0.65%. Therefore, the scour had an insignificant effect on this region which was 10m from the crest of the BW.

Fig. 55 indicates the locations of the four cross-sections where velocity comparisons were made in Fig. 56 and Fig. 57. The scour and flow depth affected flow velocity. When $Y/H = 1.25$, a 8% and 23% decrease in velocity between the bed and the crest (going horizontal to the flow) for the pre- and post-scour condition occurred, respectively (Fig. 56). When $Y/H = 2.0$ both the pre- and post-scour conditions saw a minimal change in velocity from the bed to the crest with a 11% decrease in average velocity for pre-scour and post-scour (Fig. 57a&b). As Table 12 displays, there was a 0.5% and 1% decrease between the crest pre-scour and post-scour average

velocity magnitude, for the $Y/H = 1.25$ and 2.0 , respectively. Therefore, when $\alpha = 30^\circ$, as when $\alpha = 60^\circ$, scour had little effect on the crest cross section, although there was a slightly more significant change when $Y/H = 1.25$.

Table 11 and Table 12 show that scour decreased the depth-average velocity at the BW tip when $Y/H = 1.25$ (Fig. 56a&b) by about 16%. However, when $Y/H = 2.0$ (Fig. 57a&b), there was only a 0.3% decrease in velocity at the tip between the pre- and post-scour condition. Consequently, for design purposes, the stability of the BW would actually increase during post-scour conditions because the BWs will likely fail by the rocks toppling into the scour hole. To be sure, monitoring and maintenance would be needed to repair the BW and restore its function.

Within the wake of the BW, SRH-2D only picked up a modicum of eddy formation when $Y/H = 1.25$ during the pre-scour condition (Fig. 56a&b). However, there was a significant decrease in velocity between the crest and the wake of the BW when $Y/H = 1.25$ for the pre-scour and post scour conditions. There was a 150% and 143% decrease for the pre-scour and post-scour conditions, respectively, as Fig. 56a&b suggests. When $Y/H = 2.0$, the difference in depth average velocity between the crest of the BW and the wake of the BW was 73% and 58% for the pre-scour and post-scour conditions, respectively (Fig. 57a&b). The difference between the pre-scour and post-scour average velocity, in the Wake of BW sub-cross section when $Y/H = 1.25$ was found to be increased by 13% (Table 11). This was likely due to more dissipation in the wake of the BW, due to more turbulence fueled by the increase in velocity in the pre-scour experiment. When $Y/H = 2.0$, the scour was found to cause a 16% increase in velocity (Table 12). Therefore, scour causes large changes in velocity in the wake of the BW when $Y/H = 1.25$ and $Y/H = 2.0$.

The difference in average velocity magnitude across the contraction sub cross-sections for pre-scour and post-scour, when $Y/H = 1.25$ and 2.0 was a decrease of 19% and 2%, respectively (Table 11 and Table 12). The larger difference in velocity between pre-scour and post-scour when $Y.H = 1.25$ was due to the deeper scour depth, causing a shift in the velocity magnitude distribution, pushing the contracted region maximum velocity towards the outer wall, and away from the scour hole. This larger increase in velocity within the contraction sub section can be seen in Fig. 58a&b, where the difference in velocity between pre-scour and post-scour was found for the entire model domain. The figure shows a large increase in velocity difference when $Y/H = 1.25$ and to a lesser extent when $Y/H = 2.0$ close to the right wall due to the scour hole pushing the maximum velocity distribution away from it.

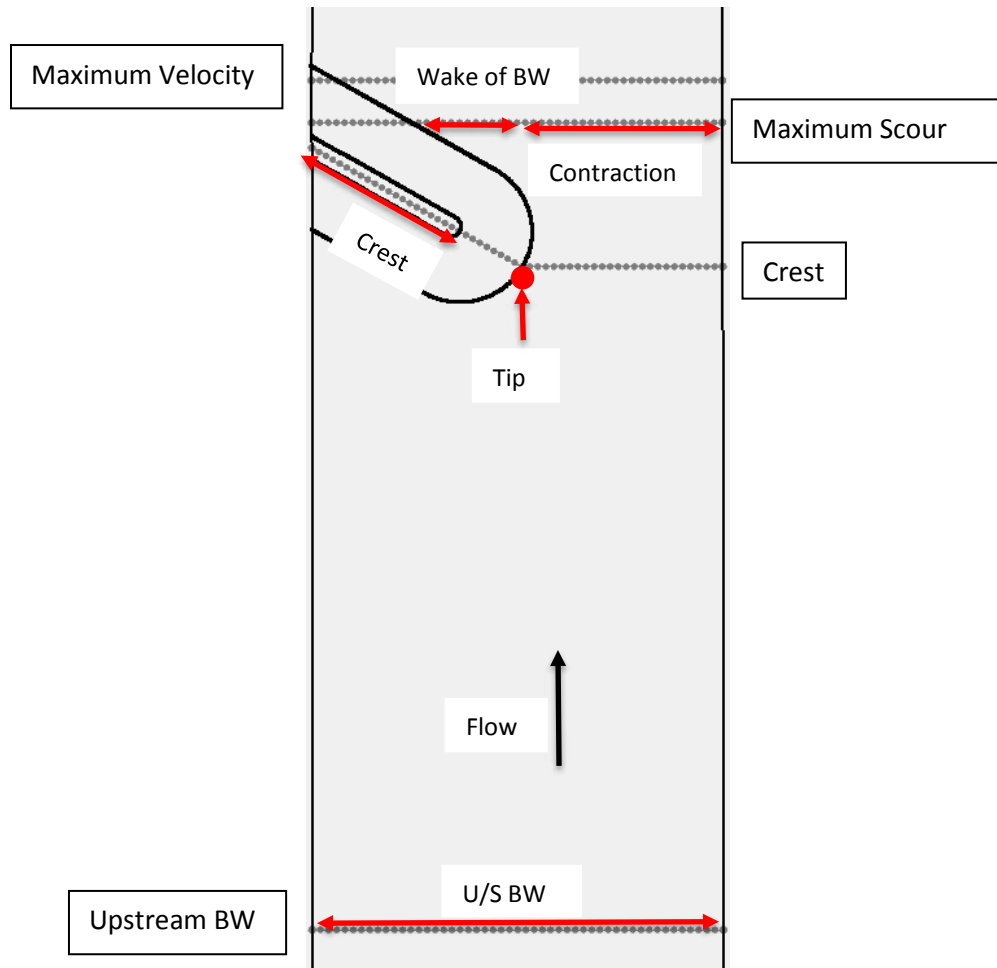
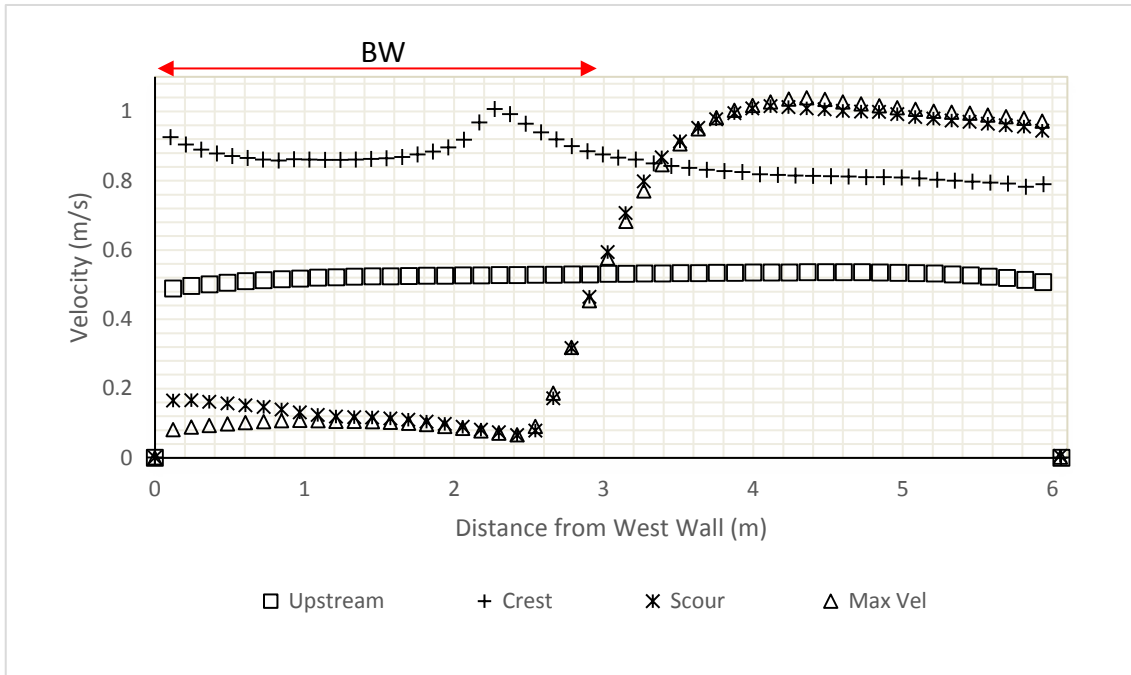
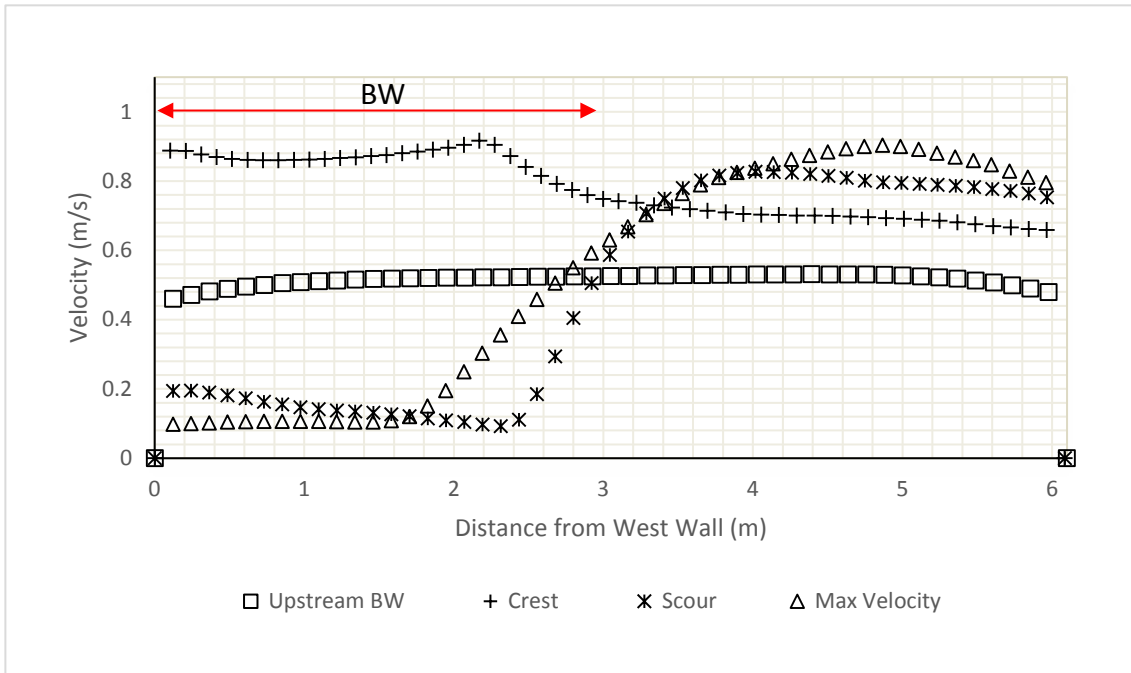


Fig. 55. The approximate locations of the cross sections where data were collected when $Y/H = 1.25$ and 2.0 . Shown here are the positions of the four cross-sections along which velocity and unit discharge distributions were determined. The max.-velocity section includes the region where flow velocity was greatest; the scour-hole section transected the max-depth of the scour hole, which extended downstream and upstream from the toe of the BW and the BW center transected the BW as opposed to the BW crest which only went along the BW crest. Note that the location of the maximum velocity cross section varied between $Y/H = 1.25$ and 2.0 .

The red arrows indicate the sub-sections that were analyzed for average velocity. The upstream BW sub-cross section included all of the values within the upstream BW cross section, the Contraction sub-cross section included the average velocity and unit discharge values from Maximum Scour cross section, the Crest sub-cross section included values from the Crest cross section, and the Wake of BW cross section included velocity values from the Maximum Velocity Cross section.



(a)

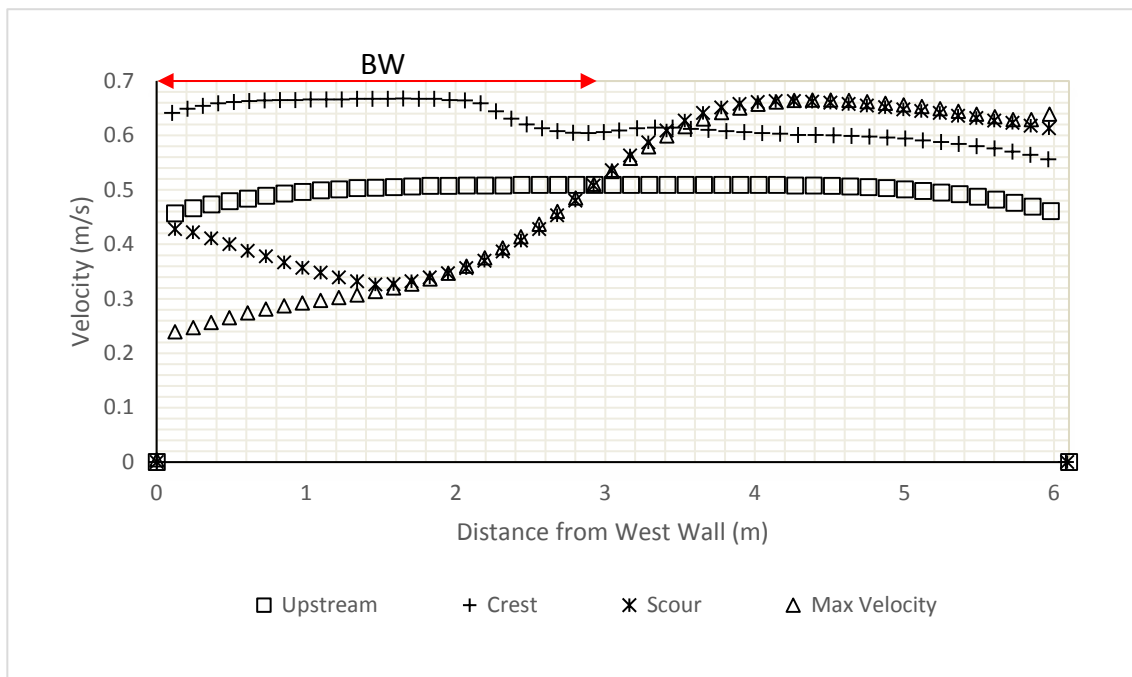


(b)

Fig. 56. Depth average velocity distribution when $Y/H = 1.25$ along the four cross-sections indicated in Fig. 55: (a) pre-scour; and; (b) post-scour



(a)



(b)

Fig. 57. Depth average velocity distribution when $Y/H = 2.0$ along the four cross-sections indicated in Fig. 55: (a) pre-scour; and; (b) post-scour

Table 11. The average velocity percent difference between pre- and post-scour at sub-cross sections with locations indicated in Fig. 55 conditions when $Y/H = 1.25$ (a positive difference indicates a decrease between pre-scour and post scour conditions and vice versa)

Sub-Cross Section	% Difference
Upstream BW	1.80
Crest	0.51
Tip	15.54
Contraction	19.24
Wake of BW	-12.86

Table 12. The average velocity percent difference between pre- and post-scour at sub-cross sections with locations indicated in Fig. 55 conditions when $Y/H = 2.0$ (a positive difference indicates a decrease between pre-scour and post scour conditions and vice versa)

Sub-Cross Section	% Difference
Upstream BW	-0.65
Crest	0.97
Tip	0.33
Contraction	1.82
Wake of BW	-16.11

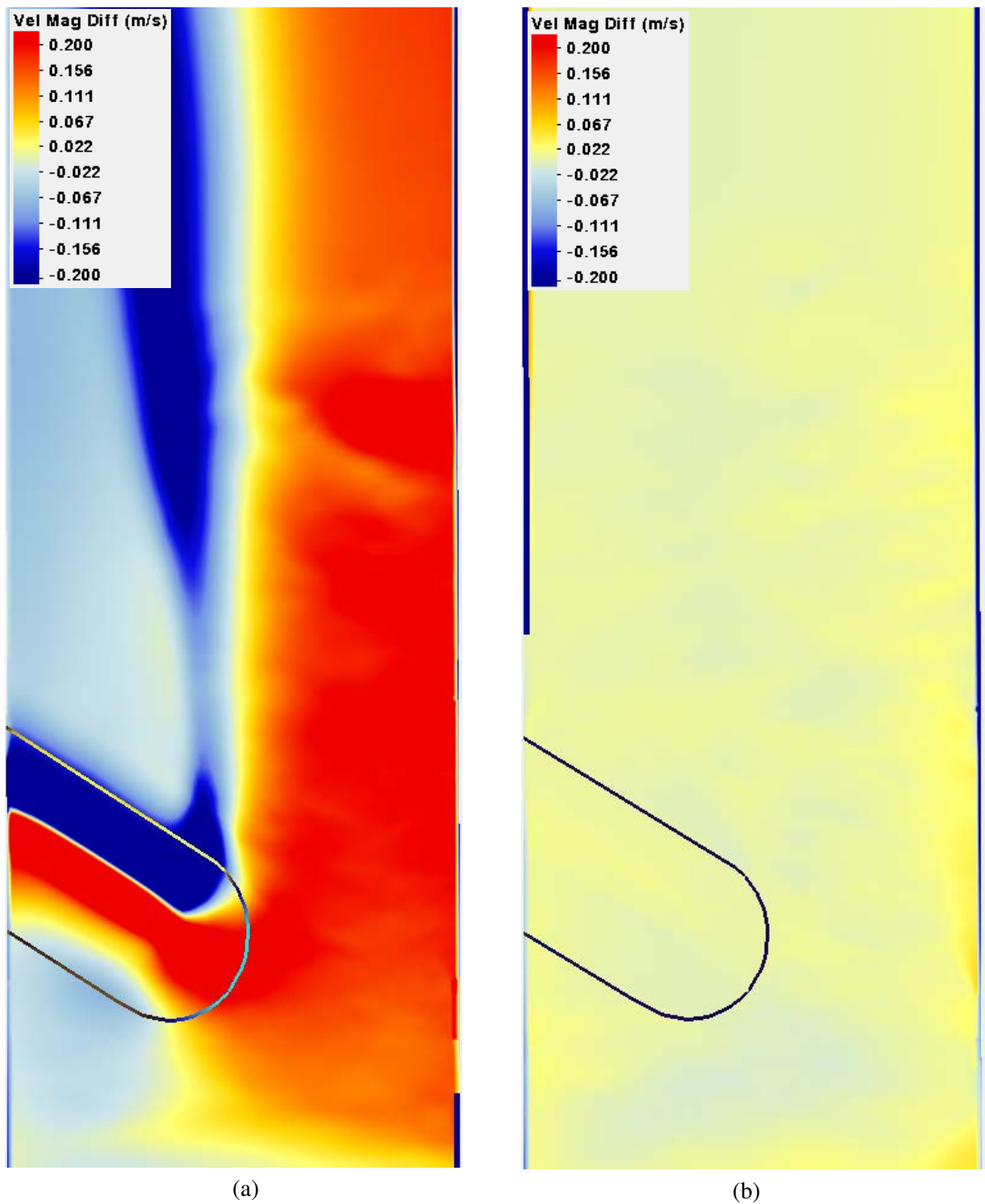


Fig. 58. Depth-average velocity magnitude difference between the pre-scour and post-scour conditions for: (a) $Y/H = 1.25$; and; (b) $Y/H = 2.0$. Red (positive) indicates a decrease between pre- and post-scour and blue (negative) indicates an increase between pre- and post-scour

4.3.5 Effect of Scour on Maximum Velocity when $Y/H = 1.25$ and 2.0 , $\alpha = 60^\circ$

The location and magnitude of the maximum velocity, V_{\max} , near the BW during the pre-scour and post-scour conditions for $Y/H = 1.25$ and 2.0 are shown in Fig. 59 and Fig. 60. The magnitude of the maximum velocity when $Y/H = 1.25$ decreased from 1.04 m/s (pre-scour) to 0.90 m/s (post-scour), a 14% decrease (Fig. 59). The maximum velocity magnitude when $Y/H = 2.0$ remained relatively constant between the pre- and post-scour conditions, with values of 0.68 m/s (pre-scour) and 0.67 m/s (post-scour) or a 1.5% decrease in the velocity magnitude (Fig. 60). Therefore, scour caused a larger decrease in maximum velocity between the pre- and post-scour conditions when $Y/H=1.25$. This change was due to the about 0.15 m (6 in) increase in maximum scour depth between the $Y/H = 1.25$ and $Y/H = 2.0$ causing the 60° -angled BW to have a more significant effect on the shallower flow field.

The maximum velocity when $Y/H = 1.25$ (Fig. 59) was the same distance downstream from the BW tip as when $Y/H = 2.0$, where $Y_{\max} = 2.8$ m for both degrees of blockage. When $Y/H = 1.25$ during the post-scour condition the maximum velocity was farther downstream than when $Y/H = 2.0$ for the post-scour condition, where Y_{\max} when $Y/H = 1.25$ was 5.5 m and Y_{\max} when $Y/H = 2.0$ was 3.30 m. It was also seen that for both $Y/H = 1.25$ and 2.0 , the scour caused the flow to reach its maximum velocity farther downstream than the pre-scour conditions. This was likely due to the deeper flow depth caused by the scour, meaning that the degree of blockage decreases for the post scour condition, and therefore creates less resistance to flow and allows the flow to more readily accelerate through the contracted region.

The lateral distance from the crest of the maximum velocity when $Y/H = 1.25$ (Fig. 59) for pre-scour and post-scour ($X_{\max} = 1.2$ m and 1.8 m, respectively) and when $Y/H = 2.0$ for pre-scour and post scour ($X_{\max} = 1.31$ m and 1.34 m, respectively) was shifted closer to the right wall

for the post-scour condition (Fig. 53 & Fig. 54). This result occurred because the scour hole created a section of slow moving velocity within the wake of the BW and farther towards the center of the channel, which pushed the location of the contracted region farther towards the right wall. This shift can be seen in Fig. 58 where the largest difference between the pre-scour and post-scour velocity was closer to the right wall. Accordingly, the deeper scour hole ($Y/H = 1.25$) shifted the maximum velocity farther to the right wall than did the shallower scour hole ($Y/H = 2.0$), indicating that the post-scour condition when $Y/H = 1.25$ provides better bank protection than when $Y/H = 2.0$. This result is reported in the study by Abad et al. (2008), who found that the maximum velocity in a bend with a series of BWs shifted more to the outer bank as the flow depth increased, thus decreasing the effectiveness by the BWs.

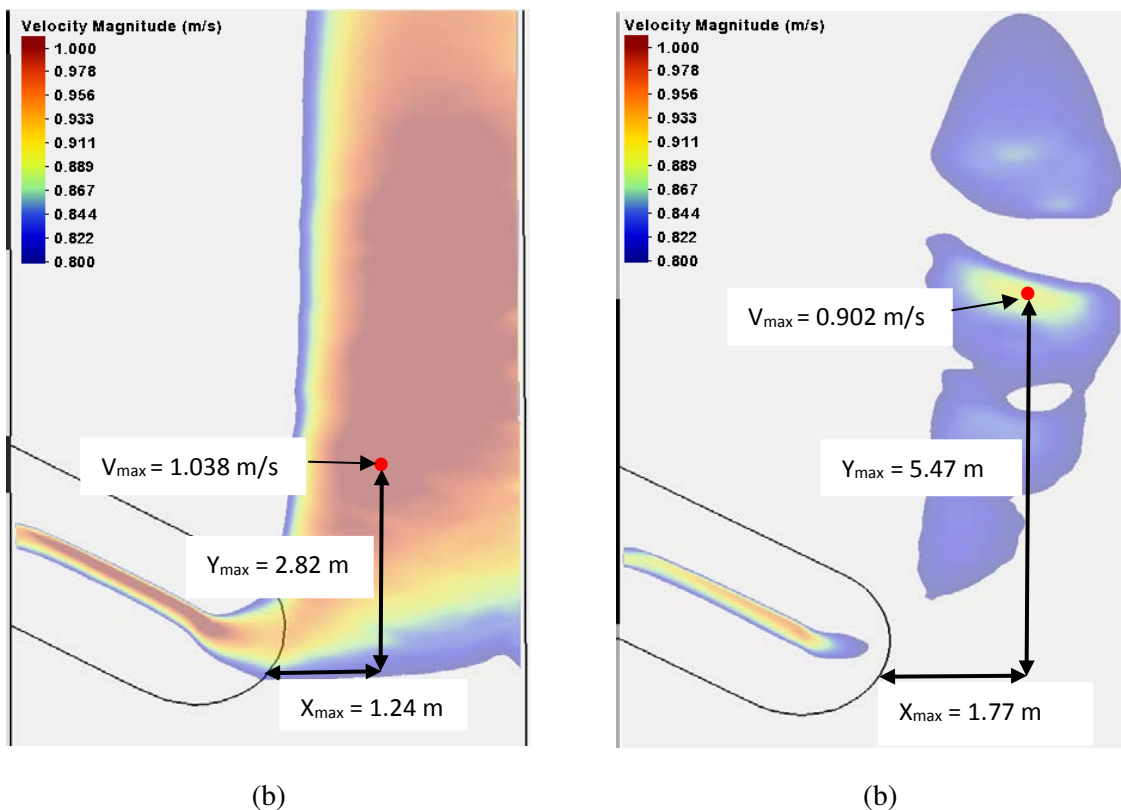


Fig. 59. The location (X_{max} and Y_{max}) and magnitude of the maximum velocity (V_{max}) for $Y/H = 1.25$; (a) pre-scour, (b) post-scour

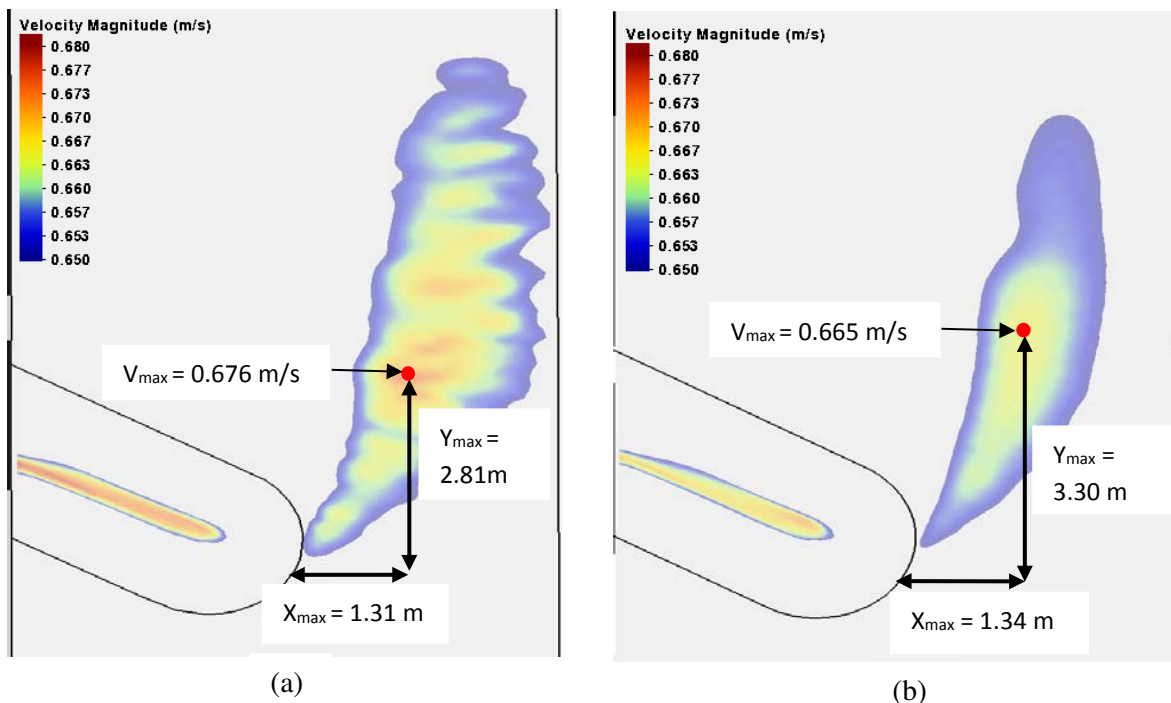


Fig. 60. The location (X_{max} and Y_{max}) and magnitude of the maximum velocity (V_{max}) for $Y/H = 2.0$; (a) pre-scour, (b) post-scour

4.3.6 Effect of Scour on Unit Discharge when $Y/H = 1.25$ and 2.0 , $\alpha = 60^\circ$

Fig. 75 and Fig. 76 indicate that there was not a significant difference between the pre-scour and post-scour unit discharges when $Y/H = 1.25$ and 2.0 for most of the cross-sections. When $Y/H = 1.25$ there was a larger difference between the pre-scour and post-scour unit discharge, but not significantly. The Upstream BW sub cross section saw a decrease in average unit discharge between the pre- and post-scour of 0.54% when $Y/H = 1.25$ (Table 13) and an increase of 0.65% when $Y/H = 2.0$ (Table 14). Therefore, the depth and velocity increased almost linearly for both degrees of blockage so that there essentially was no change in unit discharge. Also, the scour hole did not cause the contraction to have a larger backwater effect than for the pre-scour condition.

The difference in the Crest sub-cross section average unit discharge was an increase of 17% and a decrease of 1% between the pre-scour and post-scour when $Y/H = 1.25$ (Table 13) and 2.0 (Table 14), respectively. The increase in unit discharge between the pre-scour and post-scour when $Y/H = 1.25$, was likely caused by an increase in flow depth over the crest between the pre-scour and post-scour experiment. This can be seen using the specific energy diagram, where when subcritical flow goes over a hump (such as a BW) the flow loses energy, and therefore decreases in flow depth, and the decrease will be larger when the velocity was higher, where in this case it would be the pre-scour condition, thus increasing the unit discharge.

The contraction sub cross section average unit discharge decreased between the pre-scour and post-scour conditions by 5% and 1% for $Y/H = 1.25$ (Table 13) and 2.0 (Table 14), respectively. The slightly larger increase in unit discharge when $Y/H = 1.25$ was likely because the velocity significantly increases (Table 11) between the pre-scour and the post-scour conditions, but the depth, likely must decrease due to the contraction.

The wake of the BW sub cross section average unit discharge increased between pre-scour and post-scour average unit discharge of 17% when $Y/H = 1.25$ (Table 13) whereas the unit discharge stayed about the same between the pre and post scour with a slight increase of 0.4% when $Y/H = 2.0$ (Table 14). This large increase in unit discharge between pre- and post-scour when $Y/H = 1.25$ was due to the increase in velocity between pre- and post-scour, caused by the significant amount of turbulent mixing during the pre-scour conditions as Fig. 69 displays. For a detailed analysis of unit discharges at several cross sections refer to Appendix B.

Table 13. The average unit discharge percent difference between pre-scour and post-scour conditions at sub-cross sections with locations indicated in Fig. 55 when $Y/H = 1.25$ (a positive difference indicates a decrease between pre-scour and post scour conditions and vice versa)

Sub-Cross Section	% Difference
Upstream BW	0.54
Crest	-17.34
Contraction	5.38
Wake of BW	-17.45

Table 14. The average unit discharge percent difference between pre-scour and post-scour conditions at sub-cross sections with locations indicated in Fig. 55 when $Y/H = 2.0$ (a positive difference indicates a decrease between pre-scour and post scour conditions and vice versa)

Sub-Cross Section	% Difference
Upstream BW	0.60
Crest	1.28
Contraction	0.65
Wake of BW	-0.37

4.3.7 Effect of Scour on Velocity Field when $Y/H = 1.25$ and 2.0 , $\alpha = 90^\circ$

Similar to $\alpha = 30^\circ$ and 60° , the scour experiment when $Y/H = 1.25$ (Fig. 71b) had a larger effect on the flow field and velocity near the end of the BW than when $Y/H = 2.0$ (Fig. 72b). This trend was due to the larger amount of scour when $Y/H = 1.25$ (about 0.18 m, 7.0 in.), and relatedly the greater blockage due to lesser submergence of the BW by the approach flow. The differences in flow field are located in Appendix A.

For $Y/H = 1.25$ and 2.0 , Table 15 and Table 16 show that the scour did not affect the approach flow upstream of the BW. The difference between the pre- and post-scour average sub cross section velocity when $Y/H = 1.25$ was -0.8% and when $Y/H = 2.0$ was -1.0% . Therefore, the scour did not affect the depth at this sub cross section which was 10m upstream of the BW.

The scour and depth affected flow velocity. When $Y/H = 1.25$, a 7% and 3% decrease in velocity between the bed to the crest (going horizontal to the flow) for the pre- and post-scour

condition occurred, respectively (Fig. 62). When $Y/H = 2.0$ both the pre- and post-scour conditions encountered minimal change in velocity from the bed to the crest (going horizontal to the flow), with a 0.2% increase in average velocity both pre-scour and an increase of 0.3% for post-scour (Fig. 63). As Table 15 and Table 16 display, at the crest sub cross-section there was a 12% and 0.3% decrease between the crest pre- and post-scour average velocity, for $Y/H = 1.25$ and 2.0, respectively. Therefore, as when $\alpha = 30^\circ$ and $\alpha = 60^\circ$ when $\alpha = 90^\circ$, scour had little effect on the crest region when $Y/H = 2.0$, and a significant effect when $Y/H = 1.25$.

Table 15 shows that scour decreased the depth-average velocity at the BW tip when $Y/H = 1.25$ by about 9%. However, when $Y/H = 2.0$ (Table 3), there was only a 0.2% decrease in velocity at the tip between the pre- and post-scour condition. The velocity at the tip of the BW dictated the stability of the BW, so when $Y/H = 1.25$, the scour would create more stable conditions, but when $Y/H = 2.0$, there would not be a noticeable difference in stability.

Within the wake of the BW, SRH-2D simulated eddying due to boundary layer separation as indicated in Fig. 71 and Fig. 72 in Appendix A. Accordingly, the decrease in nominal average velocity behind the BW was quite large. There was a 167% and 165% decrease between the crest and the wake of the BW for the pre- and post-scour conditions, respectively, based on Fig. 62. When $Y/H = 2.0$, the difference in depth average velocity between the crest of the BW and the wake of the BW was 67% and 65% for the pre-scour and post-scour conditions, respectively based on Fig. 63. The difference between the pre-scour and post-scour average velocity, in the wake of the BW sub-cross section when $Y/H = 1.25$ decreased by 6% (Table 15). When $Y/H = 2.0$, scour caused a 2% increase in velocity (Table 16). Therefore, scour decreased the velocity a fairly insignificant amount in this region for both $Y/H = 1.25$ and 2.0, likely because of the turbulent structures controlling the flow in this region for both pre- and post-scour.

The difference in average velocity magnitude across the contraction sub cross-sections for pre- and post-scour, when $Y/H = 1.25$ and 2.0 , was marked by a decrease of 10% and an increase of 1%, respectively (Table 15 and Table 16). The larger difference in velocity between pre- and post-scour when $Y/H = 1.25$ was due to the shift in maximum velocity to the right flume wall during the post-scour condition. This increase in velocity as well as shift in the location of the velocity magnitude in the contracted region can be seen in Fig. 64, where the difference in velocity between pre-scour and post-scour was found for the entire model domain. The largest difference in velocity is in the contracted region, towards the right wall more so for $Y/H = 1.25$, but it is still evident when $Y/H = 2.0$.

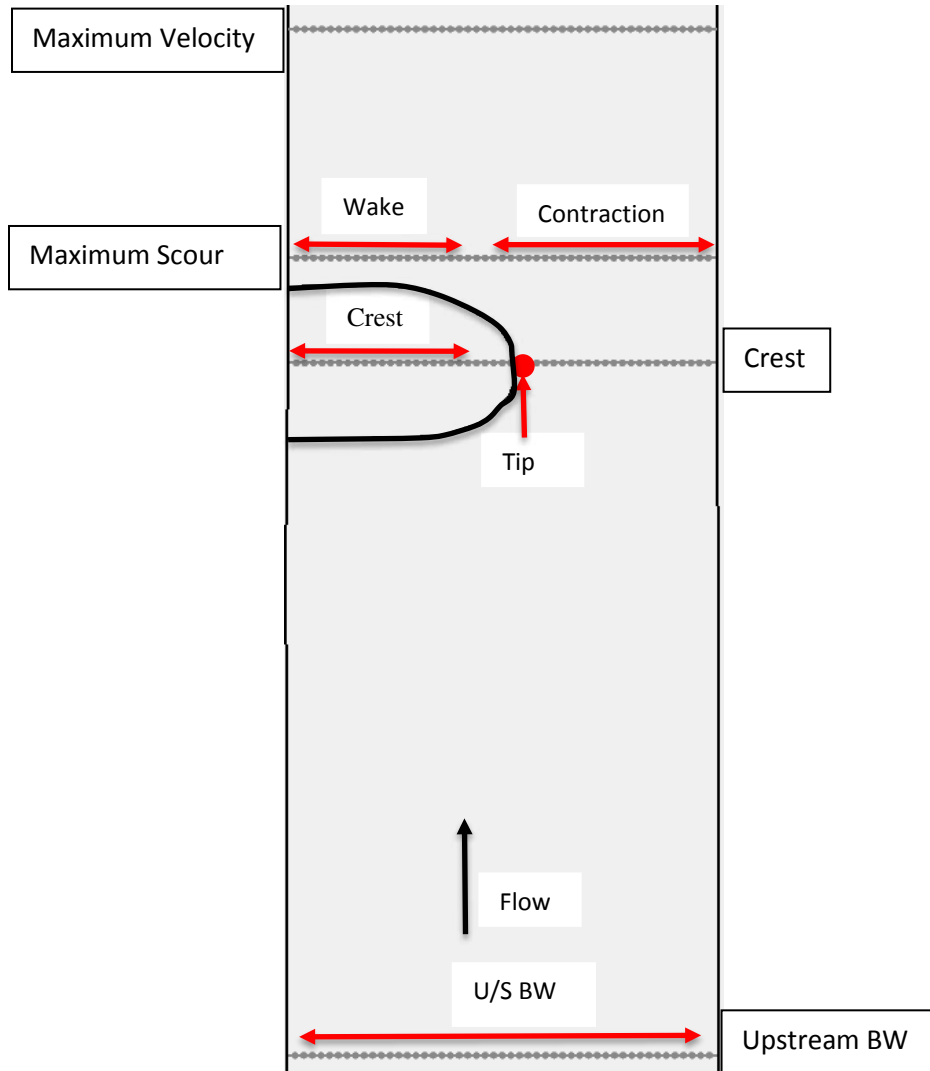
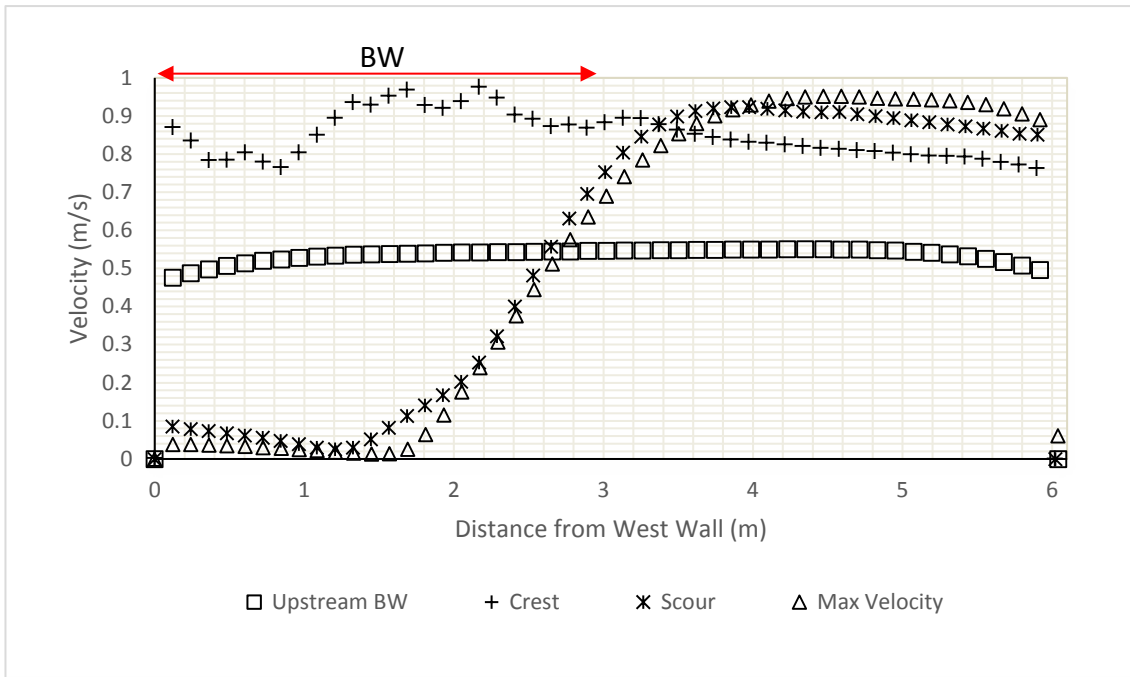
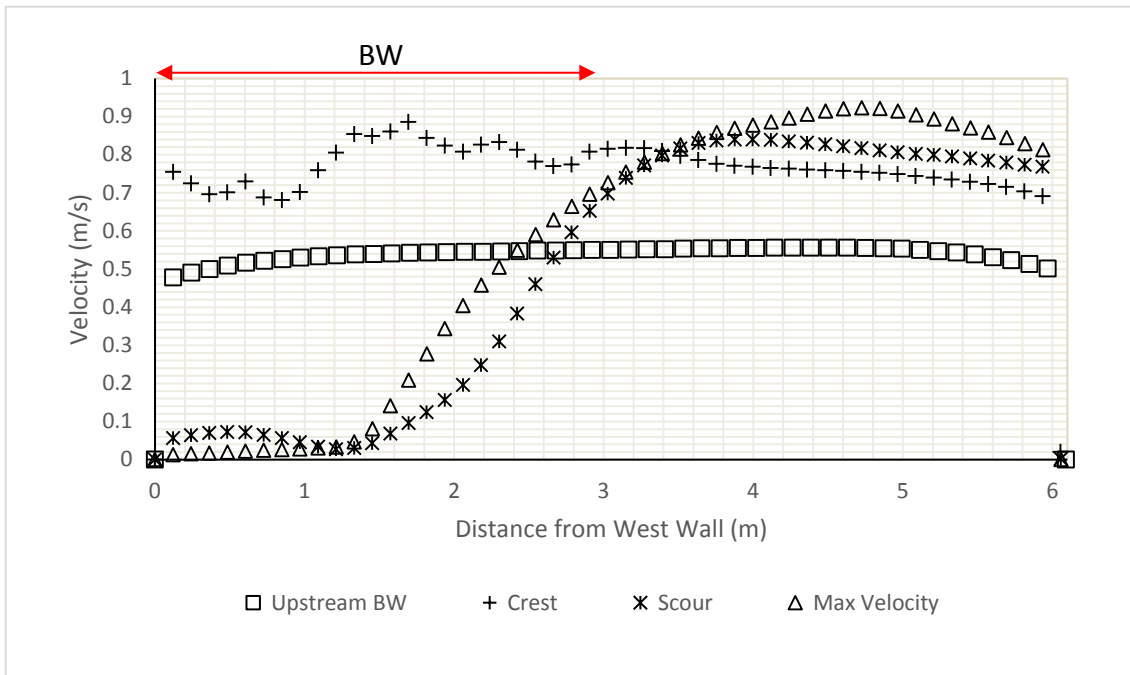


Fig. 61. The approximate locations of the cross sections where data was collected when $Y/H = 1.25$ and 2.0 . Shown here are the positions of the four cross-sections along which velocity and unit discharge distributions were determined. The max.-velocity section includes the region where flow velocity was greatest; the scour-hole section transected the max-depth of the scour hole, which extended downstream and upstream from the toe of the BW and the BW center transected the BW as opposed to the BW crest which only went along the BW crest. Note that the location of the maximum velocity cross section varied between $Y/H = 1.25$ and 2.0 .

The red arrows indicate the sub-sections that were analyzed for average velocity. The upstream BW sub-cross section included all of the values within the upstream BW cross section, the Contraction sub-cross section included the average velocity and unit discharge values from Maximum Scour cross section, the Crest sub-cross section included values from the Crest cross section, and the Wake of BW cross section included velocity values from the Maximum Velocity Cross section.



(a)

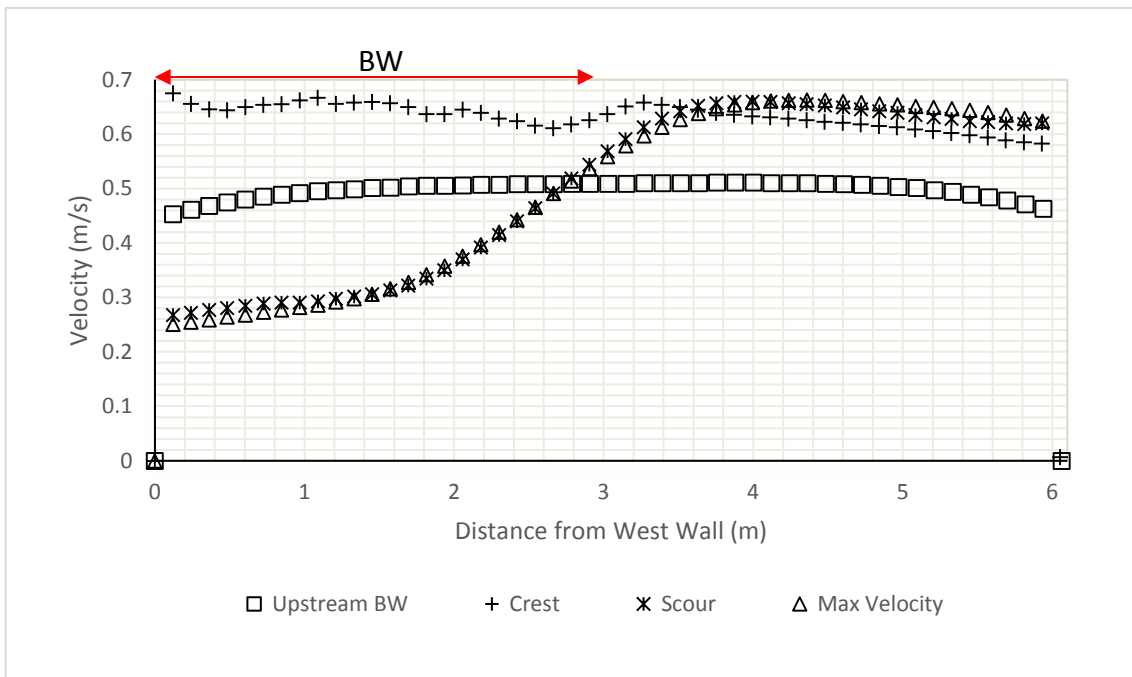


(b)

Fig. 62. Depth average velocity distribution when $Y/H = 1.25$ along the four cross-sections indicated in Fig. 61: (a) pre-scour; and; (b) post-scour



(a)



(b)

Fig. 63. Depth average velocity distribution when $Y/H = 2.0$ along the four cross-sections indicated in Fig. 61: (a) pre-scour; and; (b) post-scour

Table 15. The average velocity percent difference between the pre- and post-scour conditions at sub-cross sections indicated in Fig. 61 when $Y/H = 1.25$ (a positive increase indicates the decrease in post-scour conditions and vice versa)

Sub-Cross Section	% Difference
Upstream BW	-0.74
Crest	11.46
Tip	9.10
Contraction	9.73
Wake of BW	6.31

Table 16. The average velocity percent difference between the pre- and post-scour conditions at sub-cross sections indicated in Fig. 61 when $Y/H = 2.0$ (a positive increase indicates the decrease in post-scour conditions and vice versa)

Sub-Cross Section	% Difference
Upstream BW	-0.96
Crest	0.26
Tip	0.15
Contraction	-1.41
Wake of BW	-1.97

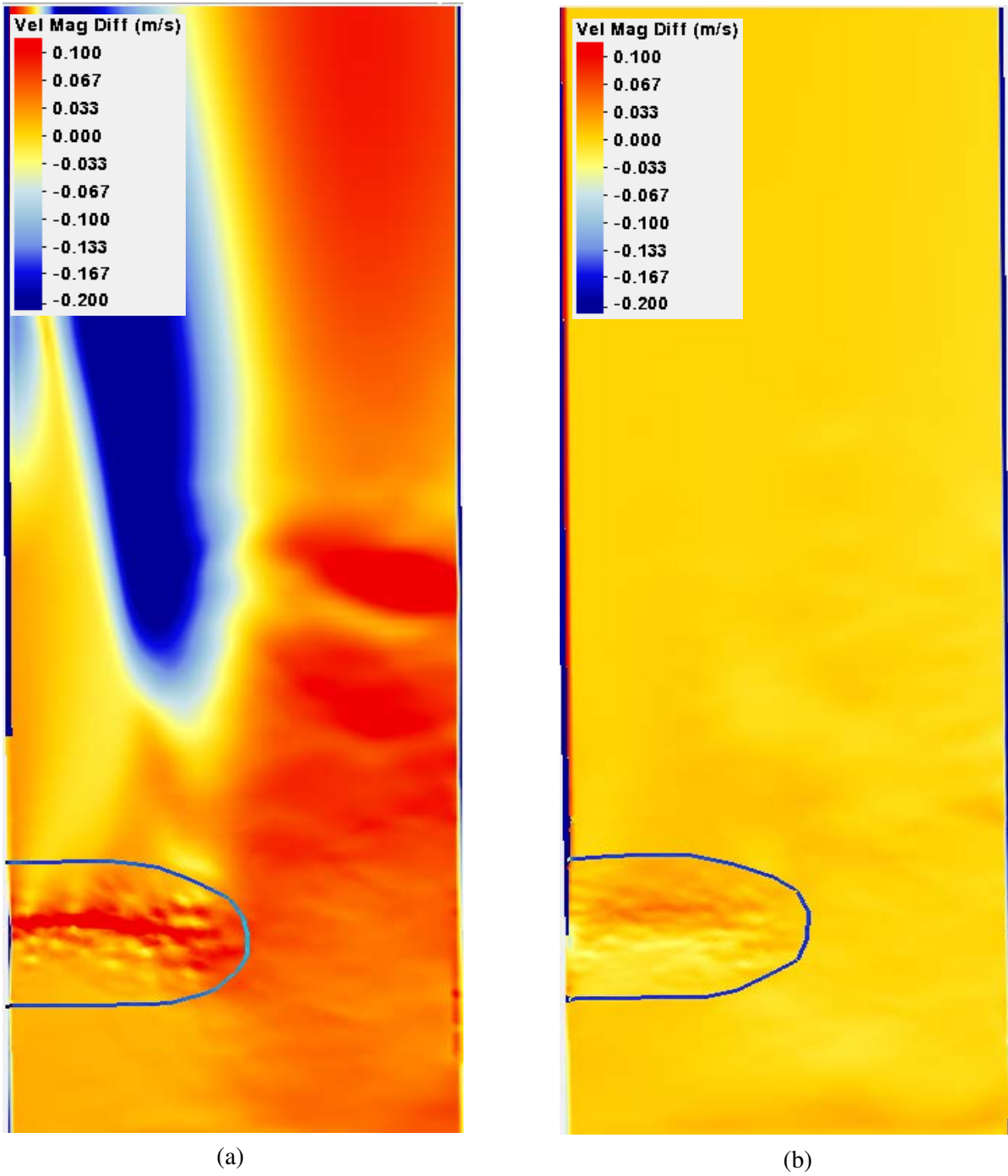


Fig. 64. Depth-average velocity magnitude difference between the pre-scour and post-scour conditions for: (a) $Y/H = 1.25$; and; (b) $Y/H = 2.0$. Red (positive) indicates a decrease between pre- and post-scour and blue (negative) indicates an increase between pre- and post-scour

4.3.8 Effects of Scour on the Maximum Velocity when $Y/H = 1.25$ and 2.0 , $\alpha = 90^\circ$

The location and magnitude of the maximum velocity, V_{\max} , near the BW during the pre-scour and post-scour conditions for $Y/H = 1.25$ and 2.0 were shown in Fig. 65a&b and Fig. 66a&b. The magnitude of the maximum velocity when $Y/H = 1.25$ decreased from 0.952 m/s (pre-scour) to 0.922 m/s (post-scour) which was a 3% decrease (Fig. 54a&b). The maximum velocity magnitude when $Y/H = 2.0$ remained relatively constant between the pre- and post-scour conditions, with values of 0.666 m/s (pre-scour) and 0.662 m/s (post-scour) or a 0.6% decrease in the velocity magnitude (Fig. 54a&b). Therefore, scour caused a larger decrease in maximum velocity between the pre- and post-scour conditions when $Y/H = 1.25$. This change was attributable to the about 6 in (0.150 m) increase in maximum scour depth between the $Y/H = 1.25$ and $Y/H = 2.0$. The change caused the $\alpha = 90^\circ$ BW to have a more significant effect on the shallower flow field. However, the difference between the pre-scour and post-scour velocity was not largely significant when $Y/H = 1.25$.

The max velocity when $Y/H = 1.25$ (Fig. 53a&b) was farther downstream for both the pre- and post-scour conditions, where $Y_{\max} = 4.5$ m and 4.8 m respectively than when $Y/H = 2.0$ (Fig. 54a&b) where $Y_{\max} = 1.3$ m and 2.8 m, respectively. This result was due to a likely narrower vena contracta farther downstream when $Y/H = 1.25$ than when $Y/H = 2.0$, so the flow was able to persist through the contraction near the BW, where the effects of blockage affected the flow when $Y/H = 1.25$ for $\alpha = 60^\circ$ and the opposite occurred where the maximum velocity for $Y/H = 1.25$ was upstream of the maximum velocity when $Y/H = 2.0$. It was also seen that for both $Y/H = 1.25$ and 2.0 , similar to $\alpha = 60^\circ$ the scour causes the flow to reach its maximum velocity farther downstream than the pre-scour conditions, which was likely due to the deeper flow depth caused by the scour, meaning that the degree of blockage decreases for the post scour

condition, and therefore creates less resistance to flow and allows the flow to more readily accelerate through the contracted region.

The location of the maximum velocity when $Y/H = 1.25$ for pre- and post-scour ($X_{\max} = 1.30$ m and 1.60 m respectively) and when $Y/H = 2.0$ for pre-scour and post scour ($X_{\max} = 0.8$ m and 1.14 m respectively) was shifted closer to the left wall for the post-scour condition (Fig. 53 & Fig. 66). This was likely because the scour hole created a region of relatively slow-moving velocity within the wake of the BW and farther towards the center of the channel, which pushed the location of the contraction section farther towards the right wall. This can be seen in Fig. 58, where the largest difference between the pre-scour and post-scour velocity was closer to the right wall. Thus, the deeper scour hole ($Y/H = 1.25$) shifts the maximum velocity farther to the right wall than did the shallower scour hole ($Y/H = 2.0$).

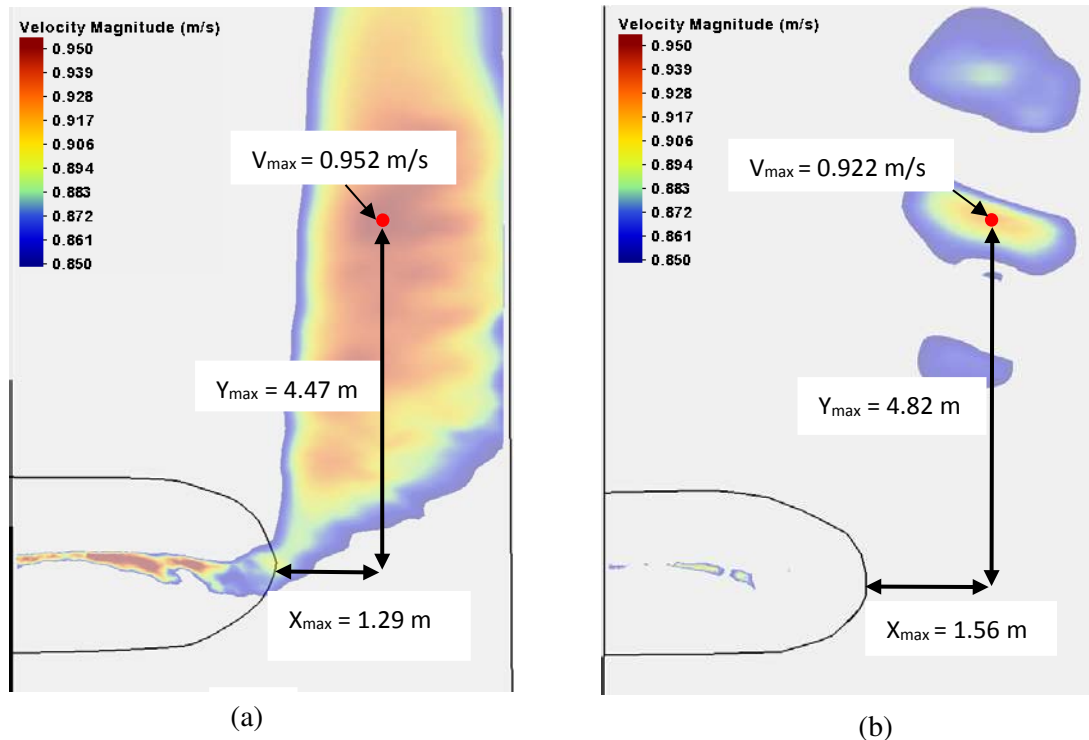


Fig. 65. The location (X_{\max} and Y_{\max}) and magnitude of the maximum velocity (V_{\max}) for $Y/H = 1.25$; (a) pre-scour, (b) post-scour

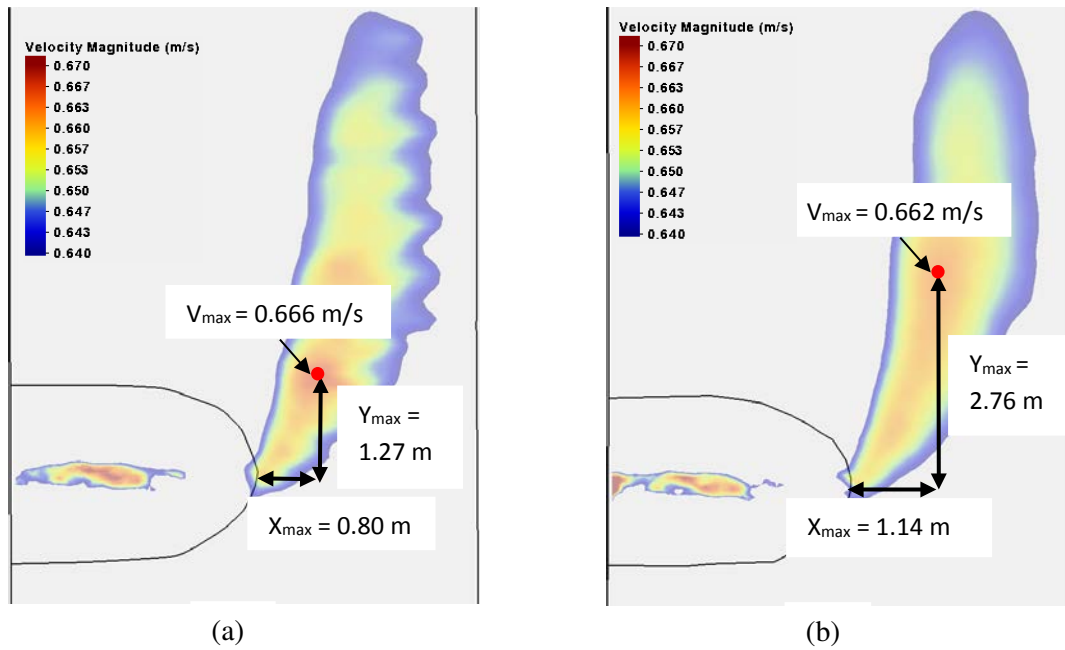


Fig. 66. The location (X_{\max} and Y_{\max}) and magnitude of the maximum velocity (V_{\max}) for $Y/H = 2.0$; (a) pre-scour, (b) post-scour

4.3.9 Effect of Scour on Unit Discharge when $Y/H = 1.25$ and 2.0 , $\alpha = 90^\circ$

Fig. 73 & Fig. 74 show that there was not a significant difference between the pre- and post-scour unit discharges when $Y/H = 1.25$ and 2.0 . When $Y/H = 1.25$ there was a slightly larger difference between the pre- and post-scour. When $Y/H = 1.25$, the upstream BW sub cross-section experienced a decrease in average unit discharge between the pre- and post-scour conditions of 0.7% and 0.4% when $Y/H = 2.0$ (Table 17) and 2.0 (Table 18), respectively. For these cross-sections, the flow velocity slightly increased between pre- and post-scour velocity for both experiments. This result arose because the flow-depth increased between the pre-scour and post scour conditions, and there was a minimal backwater effect caused by the scour.

The difference in the crest sub-cross section average unit discharge was an increase of 7% and 1% when $Y/H = 1.25$ (Table 17) and 2.0 (Table 18), respectively. The larger change in

unit discharge between the pre-scour and post-scour when $Y/H = 1.25$ than when $Y/H = 2.0$ was likely because the velocity over the crest increased significantly (12%) between the pre-scour and post-scour conditions, thus decreasing the depth more significantly over the crest (in accordance with the specific energy diagram, as mentioned in Sections 4.3.3 and 4.3.6).

The average unit discharge through the contraction sub cross section decreased between the pre- and post-scour conditions by 0.6% and increased by 2% when $Y/H = 1.25$ (Table 17) and 2.0 (Table 18), respectively. Therefore, within this region, the depth increased between the pre- and post-scour conditions when $Y/H = 1.25$ because the velocity decreased by 10%.

The average unit discharge in the wake of the BW sub cross section decreased between pre- and post-scour by 9% when $Y/H = 1.25$ (Table 17) whereas the unit discharge increased between the pre and post scour by 0.3% when $Y/H = 2.0$ (Table 18). The increase in unit discharge when $Y/H = 1.25$ indicates that the depth during the post-scour condition increased because the velocity decreased by 6% between the pre- and post-scour condition. Appendix B displays detailed unit discharges along several cross sections.

Table 17. The average unit discharge percent difference between the pre- and post-scour conditions at sub-cross sections indicated in Fig. 61 when $Y/H = 1.25$ (a positive increase indicates the decrease in post-scour conditions and vice versa)

Sub-Cross Section	% Difference
Upstream BW	0.73
Crest	7.72
Contraction	0.61
Wake of BW	8.63

Table 18. The average unit discharge percent difference between the pre- and post-scour conditions at sub-cross sections indicated in Fig. 61 when $Y/H = 2.0$ (a positive increase indicates the decrease in post-scour conditions and vice versa)

Sub-Cross Section	% Difference
Upstream BW	0.37
Crest	1.32
Contraction	-1.74
Wake of BW	-0.26

4.3.10 Discussion of Scour Effects on Velocity Field

In general, it can be determined from Table 19 and Table 20 that, when $Y/H = 1.25$ the difference in velocity was the greatest between the pre- and post-scour conditions. The velocity at the upstream cross section shows an insignificant amount of change between the pre- and post-scour conditions when $Y/H = 1.25$ indicating that the scour has an insignificant backwater effect. The scour also displays a small effect on the crest, except for $\alpha = 90^\circ$ where the velocity increases between the pre- and post-scour by 12% when $Y/H = 1.25$. This larger change was likely because of the orientation of the BW, where the scour decreases the velocity farther upstream than when $\alpha = 30^\circ$ and 60° . The contraction displayed the largest overall difference between the pre- and post-scour velocity when $Y/H = 1.25$, likely due to the shift in the vena contracta in response to the large scour hole. The velocity at the tip also decreased significantly when $Y/H = 1.25$, but not as significantly as the contraction due to the scour hole being located closer to the contraction sub cross-section. The velocity difference in the wake of the BW did not change significantly between the pre-scour and post-scour when $Y/H = 1.25$, except when $\alpha = 60^\circ$, where there was an increase in velocity between the pre- and post-scour conditions, likely due to an increase of energy dissipation in the wake of the BW between the pre-scour condition.

The difference in velocity magnitude did not change significantly between the pre-scour and post-scour conditions as shown in Table 20. The only region where the velocity change was

substantial was when $Y/H = 1.25$ and $\alpha = 60^\circ$ in the wake of the BW sub cross section. The large difference, where the velocity increase between the pre-scour and post scour was due to an increase of energy dissipation in this region in the pre-scour experiments, similar to when $Y/H = 1.25$.

Table 19. The percent difference in average velocity across the sub cross sections between the pre-scour and post scour when $Y/H = 1.25$ for $\alpha = 30^\circ, 60^\circ,$ and 90°

Location	$\alpha = 30^\circ$	$\alpha = 60^\circ$	$\alpha = 90^\circ$
Upstream BW	0.78	1.80	-0.74
Crest	4.47	0.51	11.74
Tip	8.34	15.54	9.10
Contraction	10.80	19.24	9.73
Wake of BW	4.59	-12.86	6.31

Table 20. Summary of the percent difference in average velocity across the sub cross sections when $Y/H = 2.0$ for $\alpha = 30^\circ, 60^\circ,$ and 90°

Location	$\alpha = 30^\circ$	$\alpha = 60^\circ$	$\alpha = 90^\circ$
Upstream BW	0.16	-0.65	-0.96
Crest	0.56	0.97	0.26
Tip	-0.40	0.33	0.15
Contraction	1.46	1.82	-1.41
Wake of BW	2.13	-16.11	-1.97

As displayed in Table 21 and Table 22 the unit discharge did not change significantly between the pre-and post-scour conditions. When flow velocities increased, flow depth typically decreased, and vice versa.

Table 21. Summary of the difference in unit discharge between the pre- and post-scour conditions across the sub cross sections for $Y/H = 1.25$ when $\alpha = 30^\circ, 60^\circ,$ and 90° (a positive difference indicates that the pre-scour was larger and vice versa)

Location	$\alpha = 30^\circ$	$\alpha = 60^\circ$	$\alpha = 90^\circ$
Upstream BW	0.77	0.54	0.73
Crest	2.08	-17.34	7.72
Contraction	1.97	5.38	0.61
Wake of BW	1.09	-17.45	8.63

Table 22. Summary of the difference in unit discharge between the pre- and post-scour conditions across the sub cross sections for $Y/H = 2.0$ when $\alpha = 30^\circ, 60^\circ,$ and 90° (a positive difference indicates that the pre-scour was larger and vice versa)

Location	$\alpha = 30^\circ$	$\alpha = 60^\circ$	$\alpha = 90^\circ$
Upstream BW	0.44	0.60	0.37
Crest	-0.95	1.28	1.32
Contraction	1.15	0.65	-1.74
Wake of BW	-0.41	-0.37	-0.26

Table 23 and Table 24 indicate that the difference in maximum velocity (V_{max}) between the pre- and post-scour condition was larger when $Y/H = 1.25$ than when $Y/H = 2.0$. However, the difference between pre-scour and post scour when $Y/H = 1.25$ was not large ($< 20\%$). When $Y/H = 1.25$ and 2.0 , in every BW orientation except for $\alpha = 30^\circ$, the lateral distance of the maximum velocity from the crest (X_{max}) at the post-scour condition shifted away from the crest likely because of the scour hole creating a slow zone of velocity, downstream of the tip thus pushing the vena contracta away from this zone. When $\alpha = 30^\circ$ X_{max} shifted farther towards the left wall during the post-scour condition than during the pre-scour condition because this BW orientation enabled the flow to be more heavily influenced by scour, thus allowing the flow to be forced more to the scour hole as flow typically was attracted to the deepest point. Therefore, for all orientations and flow depths, the scour would likely influence the location of the thalweg, more so for when $Y/H = 1.25$

Scour also effected the location of the streamwise distance of the maximum velocity from the tip of the BW (Y_{max}). The location of Y_{max} was shifted farther downstream during the post-scour condition than the pre-scour condition except for when $Y/H = 2.0$, $\alpha = 30^\circ$ (Table 23 and Table 24). This trend of the maximum velocity shifting downstream during the post-scour condition was likely because the blockage and roughness of the BW have a more substantial

effect on the flow pre-scour. During post-scour the blockage slightly decreased due to the scour hole and thereby caused flow to accelerate more readily away from the BW.

Table 23. The percent difference in maximum velocity (V_{max}), maximum velocity lateral distance from the crest (Y_{max}), and maximum velocity stream wise distance from the crest (X_{max}) between the pre- and post-scour when $Y/H = 1.25$ (a positive value indicates pre-scour was larger and vice versa)

α	V_{max}	X_{max}	Y_{max}
30°	4.38	18.27	-20.93
60°	14.02	-35.22	-64.25
90°	3.20	-18.95	-7.53

Table 24. The percent difference in maximum velocity (V_{max}), maximum velocity lateral distance from the crest (Y_{max}), and maximum velocity stream wise distance from the crest (X_{max}) between the pre- and post-scour when $Y/H = 2.0$ (a positive value indicates that pre-scour was larger and vice versa)

α	V_{max}	X_{max}	Y_{max}
30°	1.5	17.3	24.2
60°	1.6	-2.3	-16.0
90°	0.6	-35.1	-73.9

Overall the most important findings from this study were that scour displayed a significant effect on the velocity field when $Y/H = 1.25$ and scour displayed an effect on the location of the maximum velocity when $Y/H = 1.25$ and 2.0 . Therefore a design coefficient can be created after studies analyzing the effects of scour in bends with a set of BWs using a 3-D model and a physical model are performed.

4.3.11 Sources of Error

The main source of uncertainty occurs from the assumption that the scour morphology from $\alpha = 90^\circ$ could be applied to $\alpha = 30^\circ$ and $\alpha = 60^\circ$. In reality the scour depth will be slightly different for each BW orientation, as shown by Hemmati et al. (2016). Another source of uncertainty is the use of “smooth” BWs created in AutoCAD. Although as shown in Section 3.2.11, the difference in velocity values between the smooth and rough BWs is not dramatic, there is still a difference, and more so for $Y/H = 1.25$.

CHAPTER 5. CONCLUSIONS AND RECOMMENDATIONS

This study used multiple approaches to determine how bed scour influenced the velocity field around a BW. Part of this effort involved comparing the flow fields and velocities obtained using a 2-D numerical model (SRH-2D) and a 3-D numerical model (FLOW-3D). The main conclusions drawn from the study are listed below. A series of recommendations for topics of additional research also is given.

5.1 Conclusions

The Following main conclusions were obtained from this study:

1. The 2-D model proved useful in determining the effects of scour on the location of maximum velocity and its magnitude around a BW;
2. There was a more significant difference between pre- and post-scour velocity field when $Y/H = 1.25$ than when $Y/H = 2.0$ due to the increased scour depth;
3. Flow contraction at the BW tip is a dominant flow feature. It weakens as a flow feature when Y/H increases. Subsequently the effects of the flow blockage are more severe when $Y/H = 1.25$ than 2.0 . This was shown by the significantly larger turbulent structures in the 3-D model when $Y/H = 1.25$ than when $Y/H = 2.0$.
4. The difference in maximum velocity between the pre- and post-scour condition was larger when $Y/H = 1.25$ than when $Y/H = 2.0$, because the shallower submergence condition led to a deeper scour. The largest percent difference in maximum velocity was 14.0% and 1.5% difference when $Y/H = 1.25$ and 2.0 , respectively, both at $\alpha = 60^\circ$ indicating that this orientation may be the most effective at reducing bank erosion;

5. The maximum velocity in the sand bed for the post-scour condition shifted downstream of the pre-scour condition for all experiments except for when $\alpha = 30^\circ$ and $Y/H = 2.0$. This finding indicates that scour decreases the resistance of the flow due to the BW and draws more flow away from the BW region;
6. The maximum velocity in the sand bed during the post-scour condition shifted farther away from the BW except for when $\alpha = 30^\circ$ and $Y/H = 1.25$ and 2.0 . This finding indicates that scour at a BW may shift thalweg location away from the tip of a BW;
7. The contraction sub-cross section displayed the largest overall percent difference between the pre-and post-scour velocity when $Y/H = 1.25$, likely due to the shift in the vena contracta in response to the relatively large scour hole, which caused a commensurate decrease in velocity (Fig. 64a);
8. By comparing the 3-D model to the 2-D model it was determined that the results from $Y/H = 1.25$ matched the results of the 2-D model better than when $Y/H = 2.0$ because the decreased flow depth and subsequent increased blockage pushed a larger portion of the flow around the BW laterally than when $Y/H = 2.0$. When $Y/H = 2.0$ a large portion of the flow went over the top of the BW in the 3-D model which can be seen by the tighter spaced flow lines in Fig. 47b than when $Y/H = 1.25$ where the vertical velocity increases, thus the 2-D model will provide more inaccurate results than when $Y/H = 1.25$, because of the 2-dimensional nature of this shallow water model. The value of Manning's n had to be adjusted for this error in the flow field. The larger Manning's n given to the sand and BW when $Y/H = 2.0$ than when $Y/H = 1.25$ reflected this fact, so that less of the flow would be forced around the BW;

9. The small-scale flume testing indicated that the angle to the wall (α) did not affect the maximum scour depth, provided the degree of streamwise blockage was kept constant for the BW; and,
10. The scour morphology that wrapped around the end of the BW and the pre-test location of maximum velocity magnitude being downstream from the scour region in post-scour test indicated that the scour was caused by the combined effects of flow contraction and turbulence structures formed by the BW, similar to scour at a bridge abutment.

The effects of scour on the flow field do not yet appear to be sufficiently well understood, especially for BWs, so it is important for engineers to better determine its impacts on the flow field as well as stability of the structure to aid in the design of BWs and other instream rock structures.

5.2 Recommendations

The insights from the scour data obtained from the large-scale flume and from SRH-2D comparing pre- and post-scour conditions are useful as a preliminary study, strongly indicating that scour will affect the flow field around a BW. However, this study is limited to the use of a straight flume and a single BW. It is recommended that future studies consider the following points:

1. Use this study as a jumping off point for quantifying the effects of scour to the flow field around BW so BWs can be more accurately designed by practicing engineers;
2. Perform more experiments within a bend with a single BW to determine how the effects of the curvature such as added centrifugal force affect the pre- and post-scour velocity,
3. Conduct more flume experiments within a bend fitted with a set of BWs to determine the effects of multiple BWs on the flow field pre- and post-scour;

4. Quantify the change in direction of velocity vectors pre- and post-scour for multiple BW orientations to determine which orientation effectively changes the flow field the greatest, post-scour;
5. Confirm that different BW orientations within a bend, while keeping the degree of blockage the same do not impact the scour morphology significantly;
6. Perform more 3-D modeling, validated with hydraulic model testing to confirm the accuracy of the 2-D model around complex structures such as a BW;
7. Capture field measurements of flow velocity and the thalweg location at multiple bend radii, before and after the installment of BWs to confirm the accuracy of the results obtained from a hydraulic model; and,
8. Determine the impact of scour on BW stability.

The effects of scour on the flow field do not yet appear to be sufficiently well understood, especially for BWs so it is important for engineers to better determine its impacts on the flow field as well as stability of the structure to aid in the design of BWs and other instream rock structures.

REFERENCES

- Abad Jorge D., Rhoads Bruce L., Güneralp İnci, & García Marcelo H. (2008). Flow Structure at Different Stages in a Meander-Bend with Bendway Weirs. *Journal of Hydraulic Engineering*, 134(8), 1052–1063. [https://doi.org/10.1061/\(ASCE\)0733-9429\(2008\)134:8\(1052\)](https://doi.org/10.1061/(ASCE)0733-9429(2008)134:8(1052))
- Ballio, F., Teruzzi, A., & Radice, A. (2009). Constriction Effects in Clear-Water Scour at Abutments. *Journal of Hydraulic Engineering*, 135(2), 140–145. [https://doi.org/10.1061/\(ASCE\)0733-9429\(2009\)135:2\(140\)](https://doi.org/10.1061/(ASCE)0733-9429(2009)135:2(140))
- Bates, P., Stewart, M., Siggers, G., Smith, C., Hervouet, J., & Sellin, R. (1998). Internal and external validation of a two-dimensional finite element code for river flood simulations. *Proceedings of The Institution of Civil Engineers-Water Maritime and Energy*, 130(3), 127–141.
- Bressan, F., Ballio, F., & Armenio, V. (2011). Turbulence around a scoured bridge abutment. *Journal of Turbulence*, 12, N3. <https://doi.org/10.1080/14685248.2010.534797>
- Bridge Scour and Stream Instability Countermeasures: Experience, and Design Guidance* (3rd ed., Vols. 1–2). (n.d.). FHWA.
- Bridge Scour and Stream Instability Countermeasures: Experience, Selection and Design Guidance*. (n.d.).
- Chow, V. T. (1959). *Open-channel hydraulics*. McGraw-Hill.
- Elhakeem, M., & Papanicolaou, T. (2016). Design Procedure Enhanced with Numerical Modeling to Mitigate River-Bank Erosion. *MATEC Web of Conferences*, 68, 08003. <https://doi.org/10.1051/matecconf/20166808003>

- Ettema, R., Nakato, T., & Muste, M. (2010). *ESTIMATION OF SCOUR DEPTH AT BRIDGE ABUTMENTS NCHRP 24-20*. 436.
- Fadaei-Kermani, E., & Barani, G. A. (2014). Numerical Simulation of Flow over Spillway Based on the CFD Method. *Scientia Iranica*, 21(1), 91–97.
- FLOW-3D Users Manual*. (2008). Flow Science Inc.
- Hemmati, M., Ghomeshi, M., Ahmadi, H., & Lanzoni, S. (2016). Scour depth around flat and sloped crest bendway weirs: a laboratory study. *International Journal of River Basin Management*, 14(1), 83–93. <https://doi.org/10.1080/15715124.2015.1085870>
- HIRT, C. J. (1985). A porosity technique for the definition obstacles in rectangular cell meshes. *Fourth International Conference on Numerical Ship Hydrodynamics*, 450–468.
- Hirt, C. W., & Nichols, B. D. (1981). Volume of fluid (VOF) method for the dynamics of free boundaries. *Journal of Computational Physics*, 39(1), 201–225. [https://doi.org/10.1016/0021-9991\(81\)90145-5](https://doi.org/10.1016/0021-9991(81)90145-5)
- Huang, S. L., & Ng, C.-O. (2007). Hydraulics of a submerged weir and applicability in navigational channels: basic flow structures. *International Journal for Numerical Methods in Engineering*, 69(11), 2264–2278. <https://doi.org/10.1002/nme.1849>
- Jamieson, E. C., Rennie, C. D., Jacobson, R. B., & Townsend, R. D. (2011). 3-D flow and scour near a submerged wing dike: ADCP measurements on the Missouri River: 3-D FLOW AND SCOUR NEAR A SUBMERGED WING DIKE. *Water Resources Research*, 47(7). <https://doi.org/10.1029/2010WR010043>
- Jia Y., Scott S., Xu Y., & Wang S. S. Y. (2009). Numerical Study of Flow Affected by Bendway Weirs in Victoria Bendway, the Mississippi River. *Journal of Hydraulic Engineering*, 135(11), 902–916. [https://doi.org/10.1061/\(ASCE\)0733-9429\(2009\)135:11\(902\)](https://doi.org/10.1061/(ASCE)0733-9429(2009)135:11(902))

Julien, P. Y. (2010, June). Erosion and Sedimentation.

<https://doi.org/10.1017/CBO9780511806049>

Julien, P. Y., & Duncan, J. R. (2003). *OPTIMAL DESIGN CRITERIA OF BENDWAY WEIRS FROM NUMERICAL SIMULATIONS AND PHYSICAL MODEL STUDIES*. 40.

Kinzli, K.-D., & Thornton, C. I. (2010). Predicting velocity in bendway weir eddy fields. *River Research and Applications*. 26: 823-834., 823–834.

Koken, M. (2011). Coherent structures around isolated spur dikes at various approach flow angles. *Journal of Hydraulic Research*, 49(6), 736–743.

<https://doi.org/10.1080/00221686.2011.616316>

Koken, M., & Constantinescu, G. (2008). An investigation of the flow and scour mechanisms around isolated spur dikes in a shallow open channel: 2. Conditions corresponding to the final stages of the erosion and deposition process. *Water Resources Research*, 44(8).

<https://doi.org/10.1029/2007WR006491>

Kuhnle, R. A., Alonso, C. V., & Shields, F. D. (2002). Local Scour Associated with Angled Spur Dikes. *Journal of Hydraulic Engineering*, 128(12), 1087–1093.

[https://doi.org/10.1061/\(ASCE\)0733-9429\(2002\)128:12\(1087\)](https://doi.org/10.1061/(ASCE)0733-9429(2002)128:12(1087))

Lagasse, P. F., Clopper, P. E., Pagan-Ortiz, J. E., Zevenbergen, L. W., Arneson, L. A., Schall, J. D., & Girard, L. G. (2009). *Bridge Scour and Stream Instability Countermeasures: Experience, and Design Guidance, Volume 2, Third Edition* (No. FHWA NHI HEC-23). Arlington, Virginia: Federal Highway Administration.

Lai, Y.G. (2008). SRH-2D Version 2: Theory and User's Manual. *U.S. Department of the Interior Bureau of Reclamation Technical Service Center*.

- Lai, Yong G. (2010). Two-Dimensional Depth-Averaged Flow Modeling with an Unstructured Hybrid Mesh. *Journal of Hydraulic Engineering*, 136(1), 12–23.
[https://doi.org/10.1061/\(ASCE\)HY.1943-7900.0000134](https://doi.org/10.1061/(ASCE)HY.1943-7900.0000134)
- Piotrowski, J. A. (2010). *Development of a high-resolution two-dimensional urban/rural flood simulation* (University of Iowa). Retrieved from <https://ir.uiowa.edu/etd/574>
- Scurlock, S., M., Baird, C., D., Cox, L., A., & Thornton, I., C. (2012, April). *Bendway weir design - Rio Grande Physical Model*. Bureau of Reclamation.
- Scurlock, S. M., Cox, A. L., Baird, C. L., Thornton, C. I., & Abt, R. de B. (2015). *HYBRID HYDRAULIC MODELING OF RIVER-TRAINING STRUCTURES IN SINUOUS CHANNELS*.
- Seifken, S. (2019). *Computational Fluid Dynamics Models of Rio Grande Bends Fitted with Rock Vanes or Bendway Weirs*. Colorado State University, Fort Collins, CO.
- Sturm, T. W. (2006). Scour around Bankline and Setback Abutments in Compound Channels. *Journal of Hydraulic Engineering*, 132(1), 21–32. [https://doi.org/10.1061/\(ASCE\)0733-9429\(2006\)132:1\(21\)](https://doi.org/10.1061/(ASCE)0733-9429(2006)132:1(21))
- Sturm, T. W., & Janjua, N. S. (1994). Clear-Water Scour around Abutments in Floodplains. *Journal of Hydraulic Engineering*, 120(8), 956–972.
[https://doi.org/10.1061/\(ASCE\)0733-9429\(1994\)120:8\(956\)](https://doi.org/10.1061/(ASCE)0733-9429(1994)120:8(956))
- Teruzzi Anna, Ballio Francesco, & Armenio Vincenzo. (2009). Turbulent Stresses at the Bottom Surface near an Abutment: Laboratory-Scale Numerical Experiment. *Journal of Hydraulic Engineering*, 135(2), 106–117. [https://doi.org/10.1061/\(ASCE\)0733-9429\(2009\)135:2\(106\)](https://doi.org/10.1061/(ASCE)0733-9429(2009)135:2(106))

- Thanos Papanicolaou A. N., Bressan Filippo, Fox James, Kramer Casey, & Kjos Lisa. (2018). Role of Structure Submergence on Scour Evolution in Gravel Bed Rivers: Application to Slope-Crested Structures. *Journal of Hydraulic Engineering*, 144(2), 03117008.
[https://doi.org/10.1061/\(ASCE\)HY.1943-7900.0001411](https://doi.org/10.1061/(ASCE)HY.1943-7900.0001411)
- Versteeg, H. K., & Malalasekera, W. (2007). *An Introduction to Computational Fluid Dynamics - The Finite Volume Method* (2nd ed.). Essex, England: Pearson Education Limited.
- Yakhot, V., & Smith, L. M. (1992). The renormalization group, the ε -expansion and derivation of turbulence models. *Journal of Scientific Computing*, 7(1), 35–61.
<https://doi.org/10.1007/BF01060210>
- Zey, S. S. (2017). *Department of Civil and Environmental Engineering*. Colorado State University.

APPENDIX A. VELOCITY VECTORS

This appendix displays the velocity vectors for $Y/H = 1.25$ and 2.0 for the pre- and post-scour conditions.

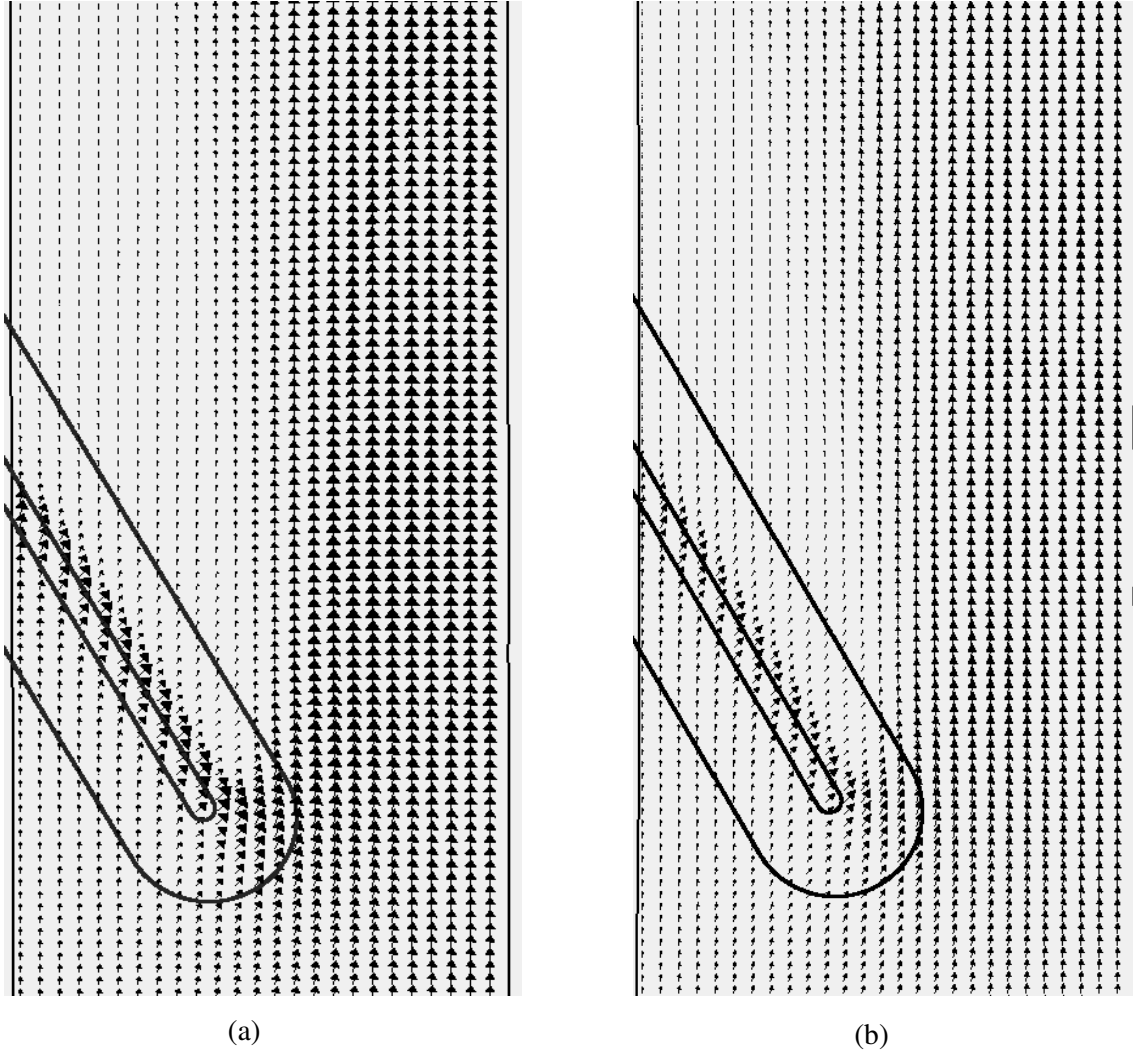


Fig. 67. Plan views of depth-averaged velocity vectors, $Y/H = 1.25$ and $\alpha = 90^\circ$: (a) pre-scour; and, (b) post-scour

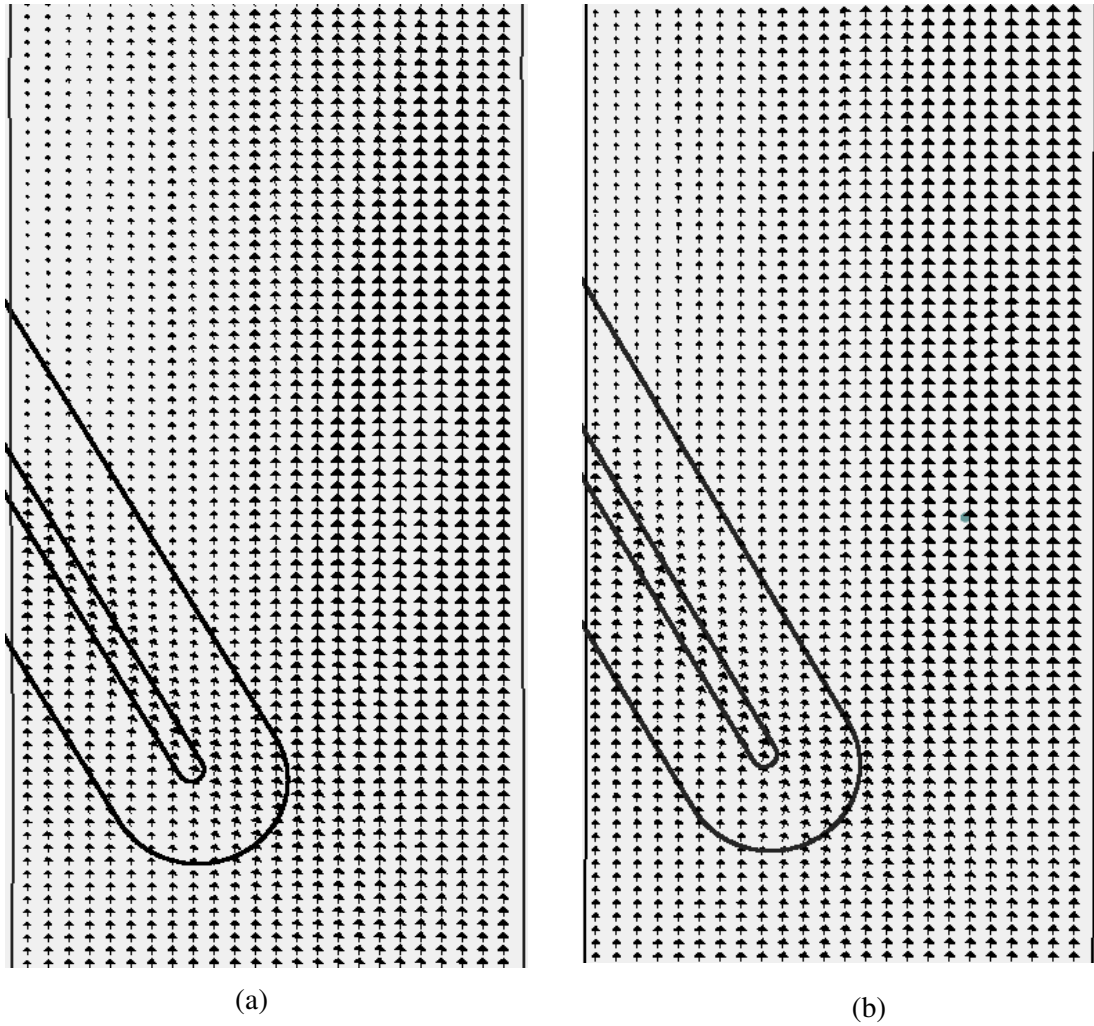


Fig. 68. Plan views of depth-averaged velocity vectors, $Y/H = 2.0$ and $\alpha = 90^\circ$: (a) pre-scour; and, (b) post-scour

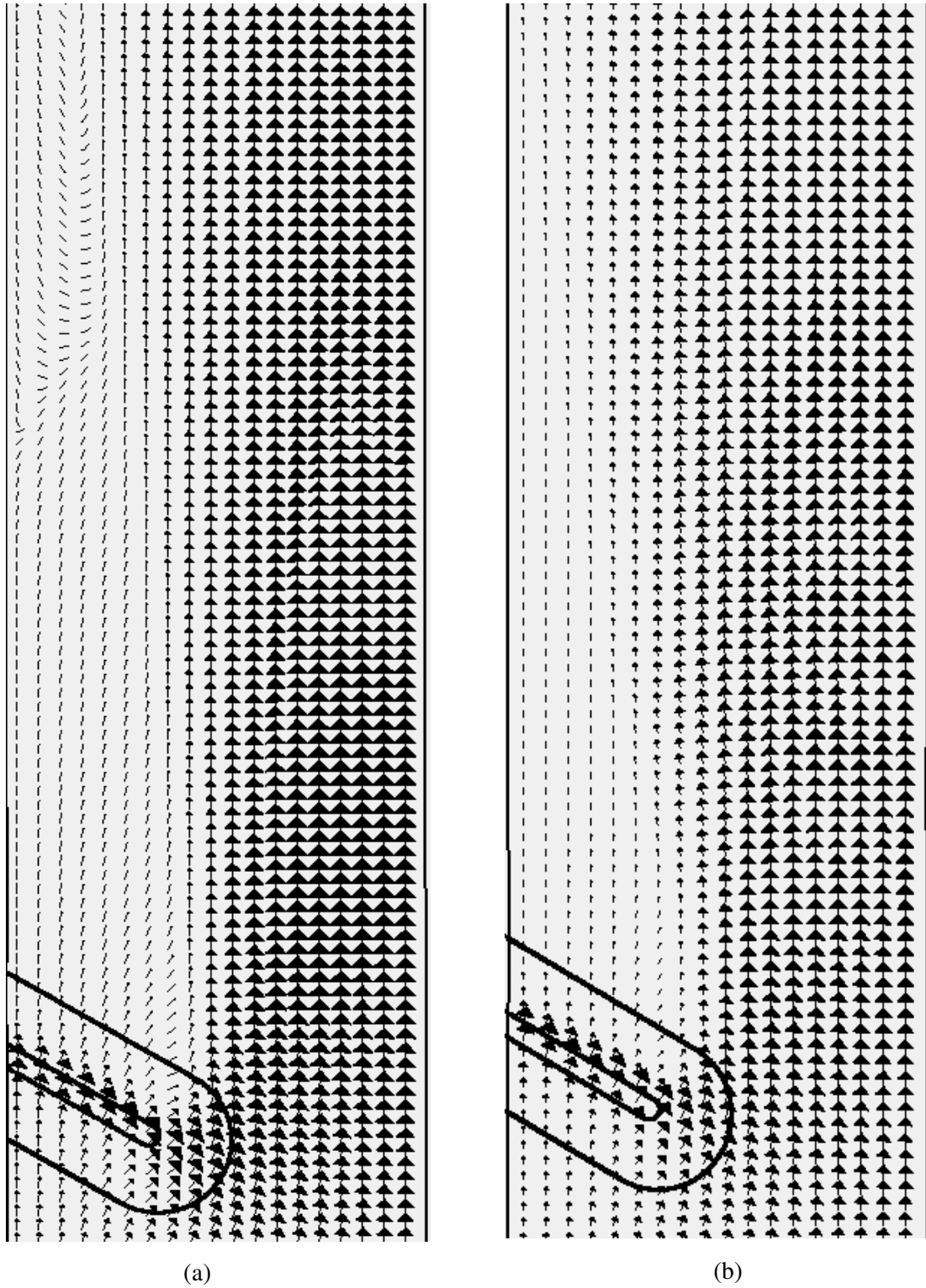


Fig. 69. Plan views of depth-averaged velocity vectors, $Y/H = 1.25$ and $\alpha = 60^\circ$: (a) pre-scour; and, (b) post-scour

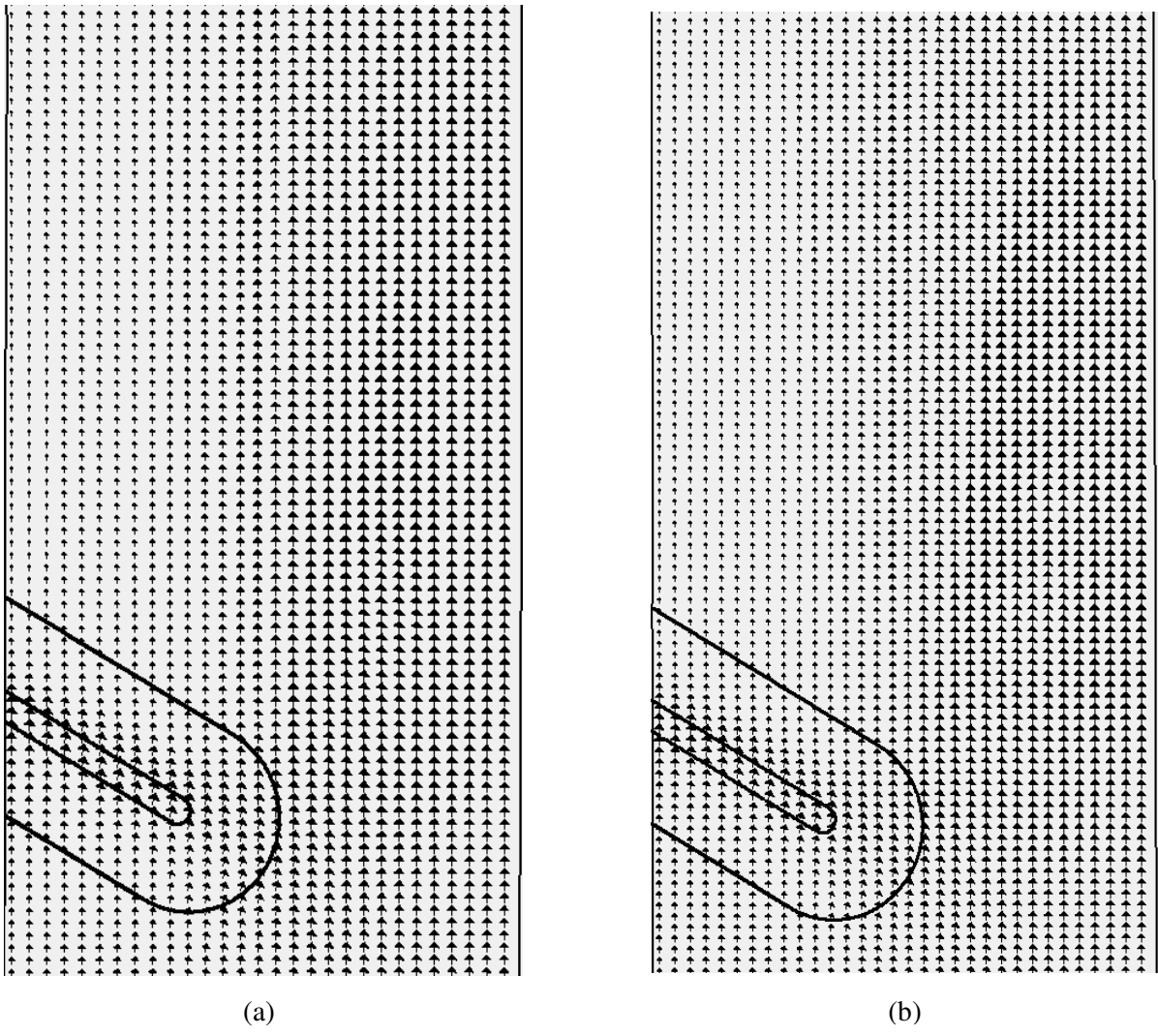


Fig. 70. Plan views of depth-averaged velocity vectors, $Y/H = 2.0$ and $\alpha = 60^\circ$: (a) pre-scour; and, (b) post-scour

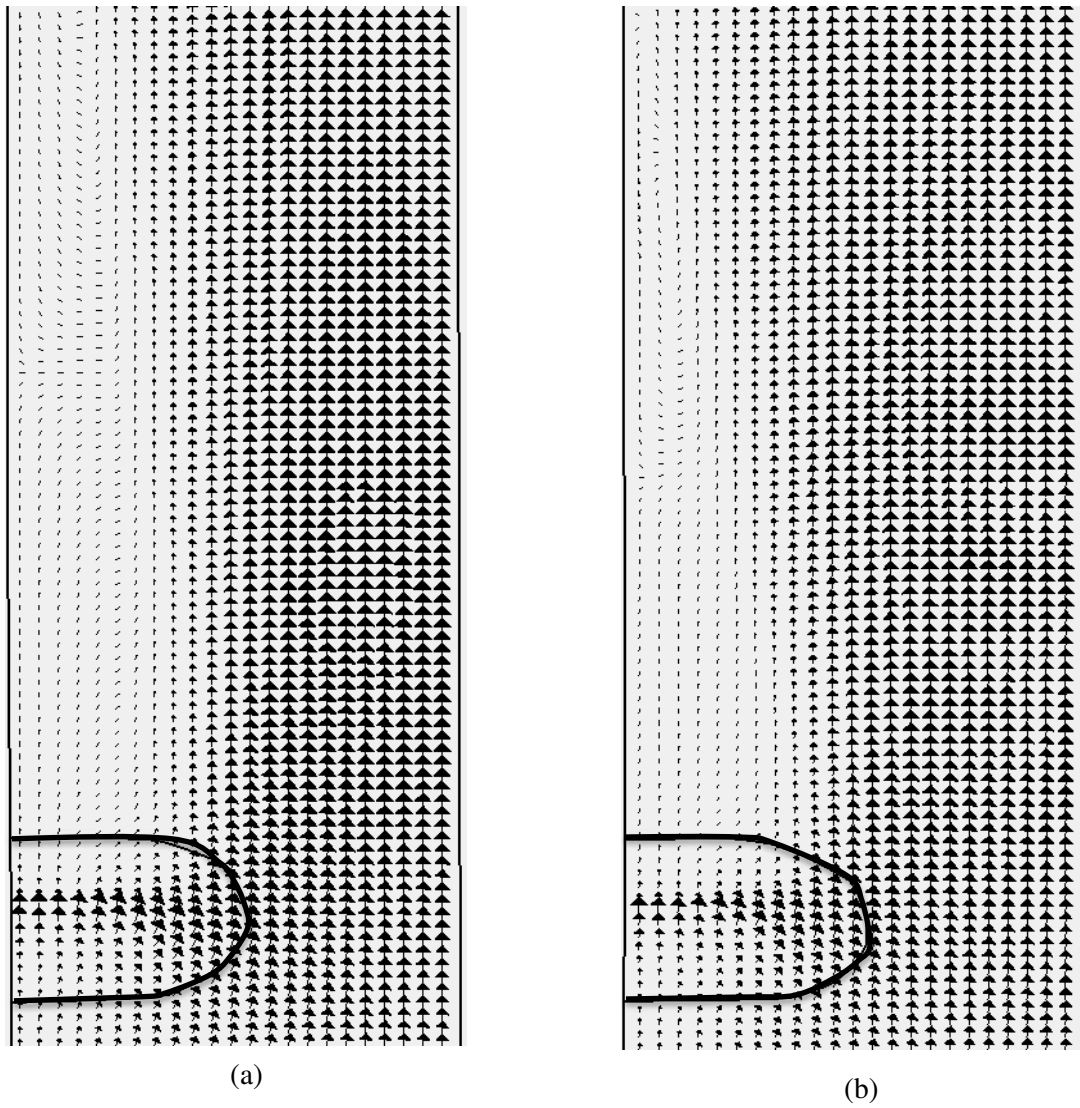


Fig. 71. Plan views of depth-averaged velocity vectors, $Y/H = 1.25$ and $\alpha = 90^\circ$: (a) pre-scour; and, (b) post-scour

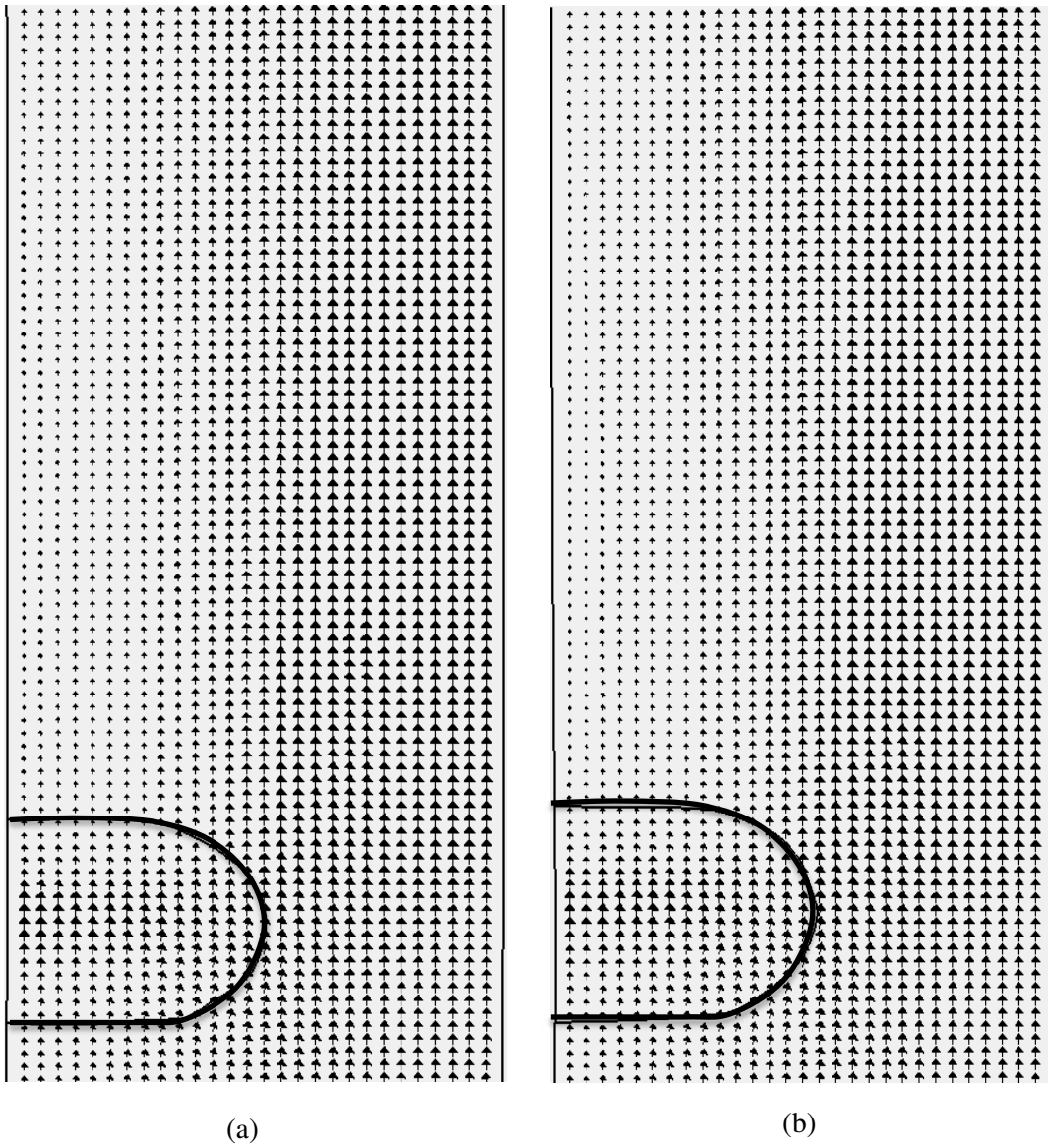
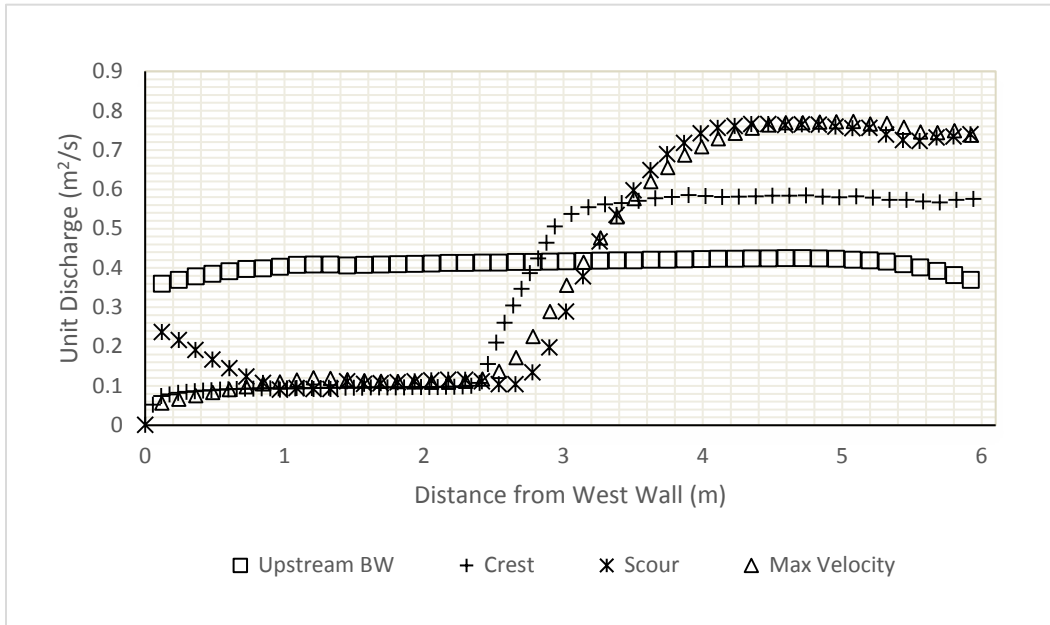


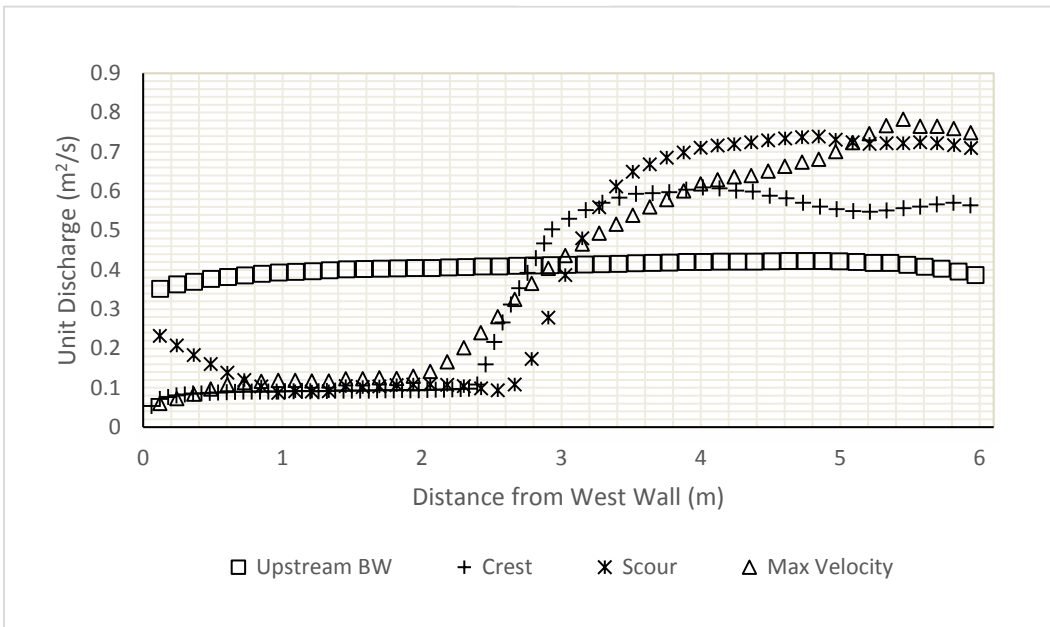
Fig. 72. Plan views of depth-averaged velocity vectors, $Y/H = 2.0$ and $\alpha = 90^\circ$: (a) pre-scour; and, (b) post-scour

APPENDIX B. UNIT DISCHARGE

This appendix displays the unit discharge distribution along the cross sections where the velocity distributions were found for pre- and post-scour, when $Y/H = 1.25$ and 2.0 .

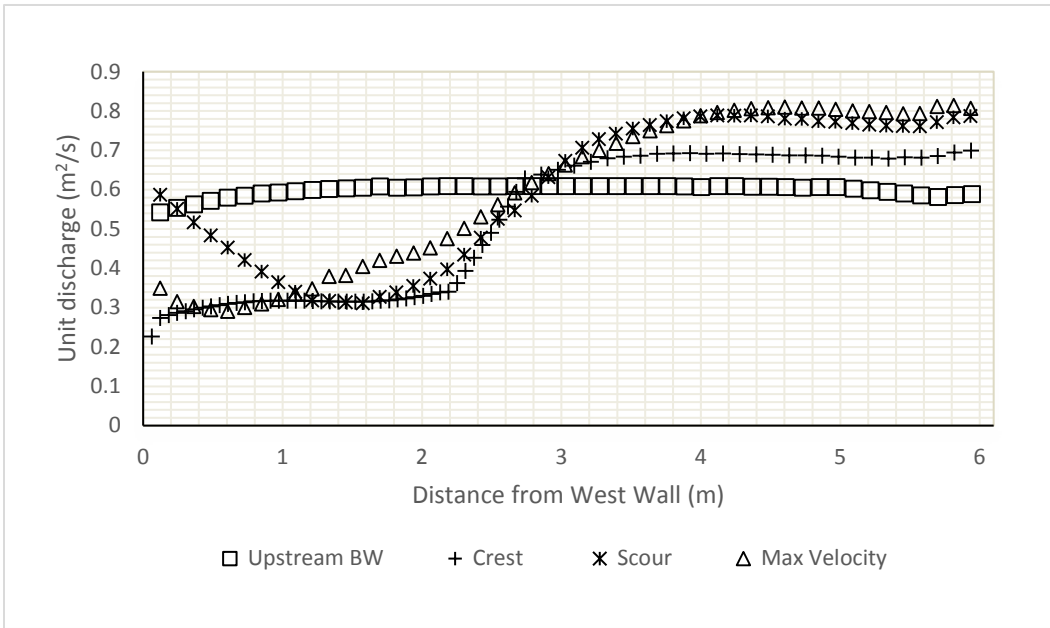


(a)

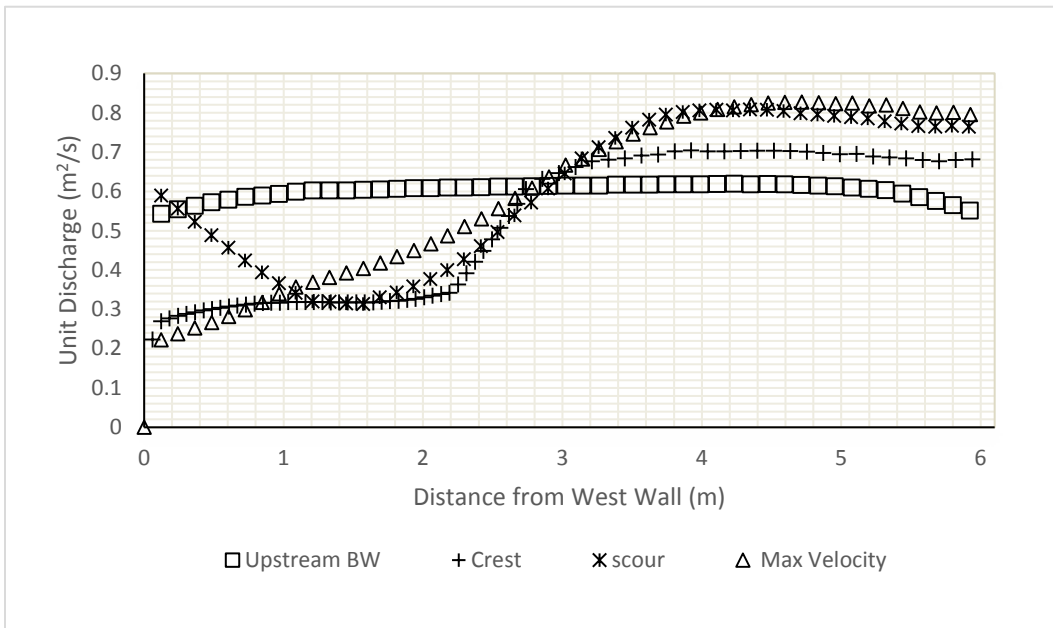


(b)

Fig. 73. Unit discharge distribution when $Y/H = 1.25$ and $\alpha = 30^\circ$ along the four cross-sections indicated in Fig. 49: (a) pre-scour; and; (b) post-scour

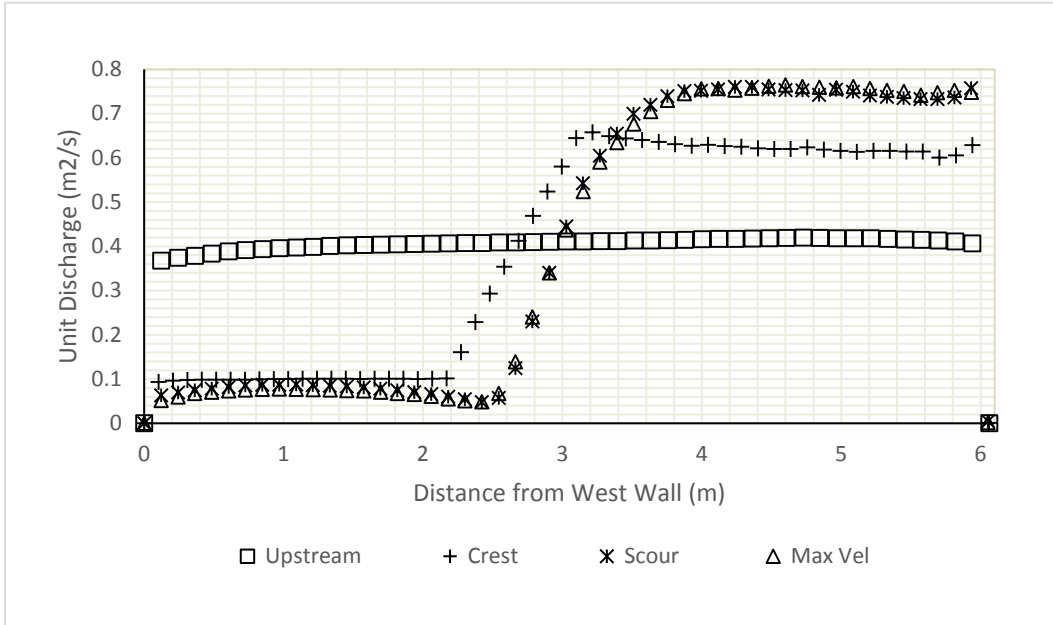


(a)

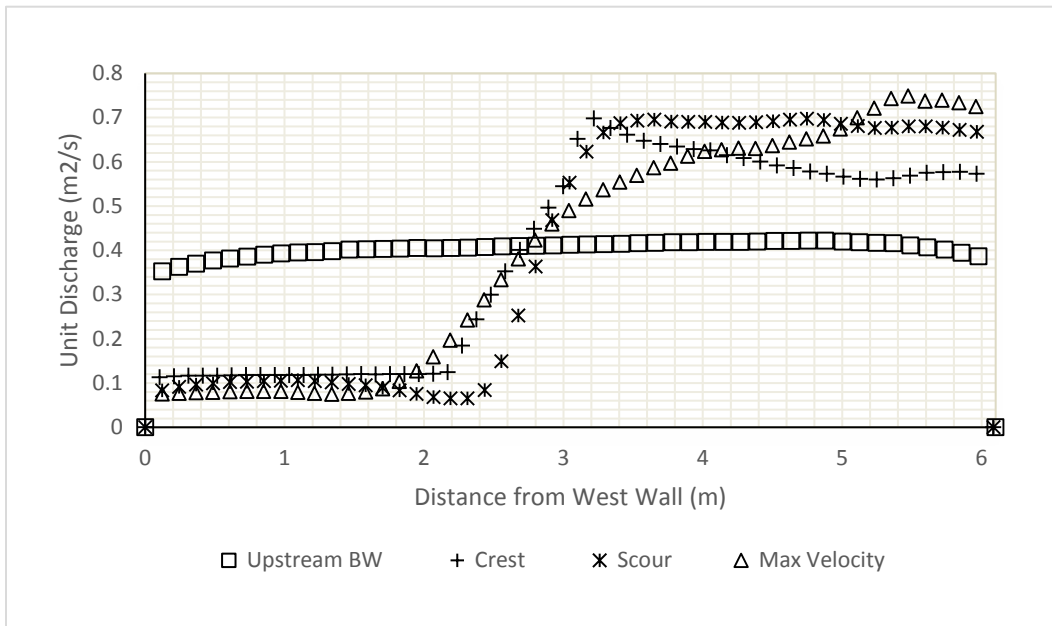


(b)

Fig. 74. Unit discharge distribution when $Y/H = 2.0$ and $\alpha = 30^\circ$ along the four cross-sections indicated in Fig. 49: (a) pre-scour; and; (b) post-scour

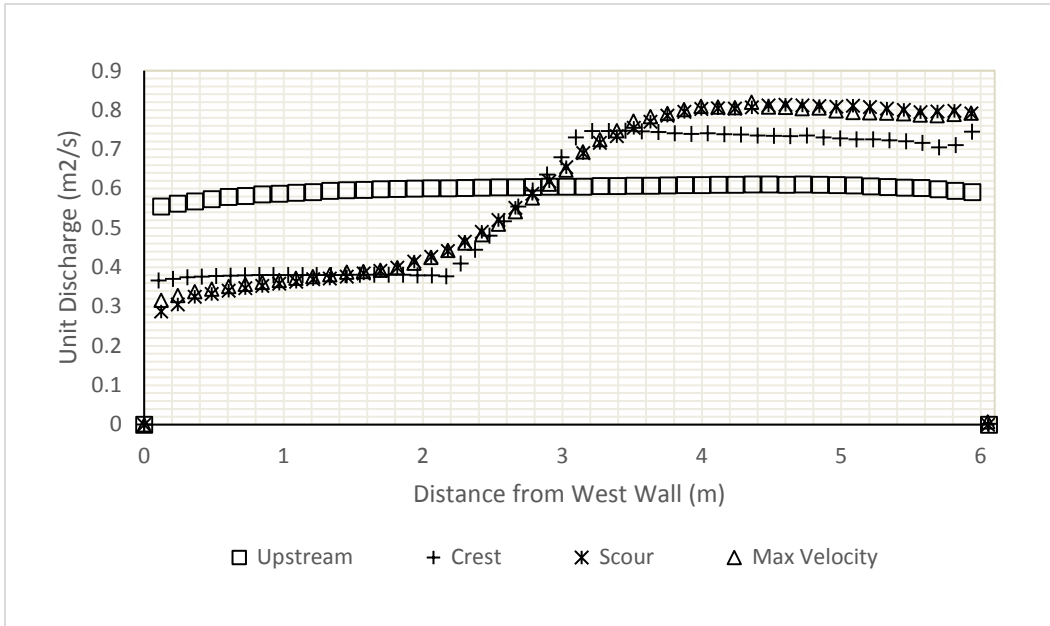


(a)

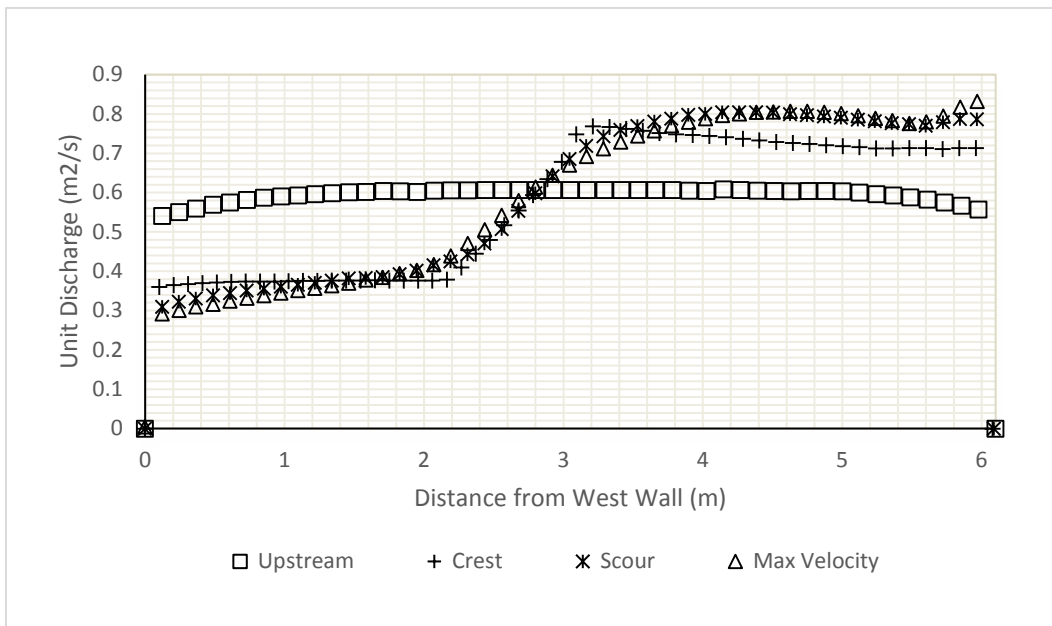


(b)

Fig. 75. Unit discharge distribution when $Y/H = 1.25$ and $\alpha = 60^\circ$ along the four cross-sections indicated in Fig. 55: (a) pre-scour; and; (b) post-scour

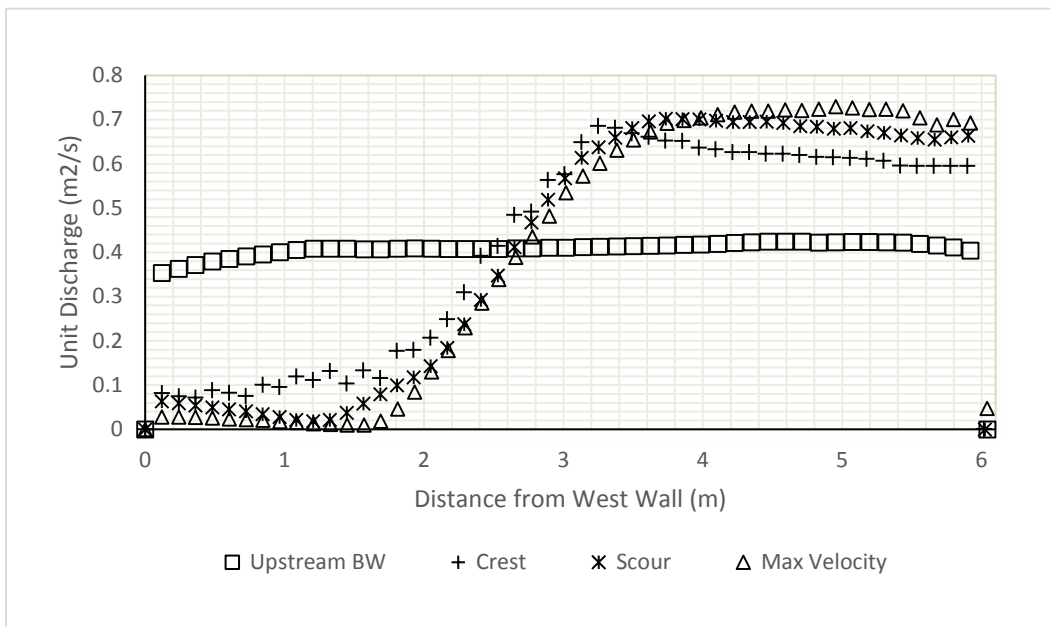


(a)

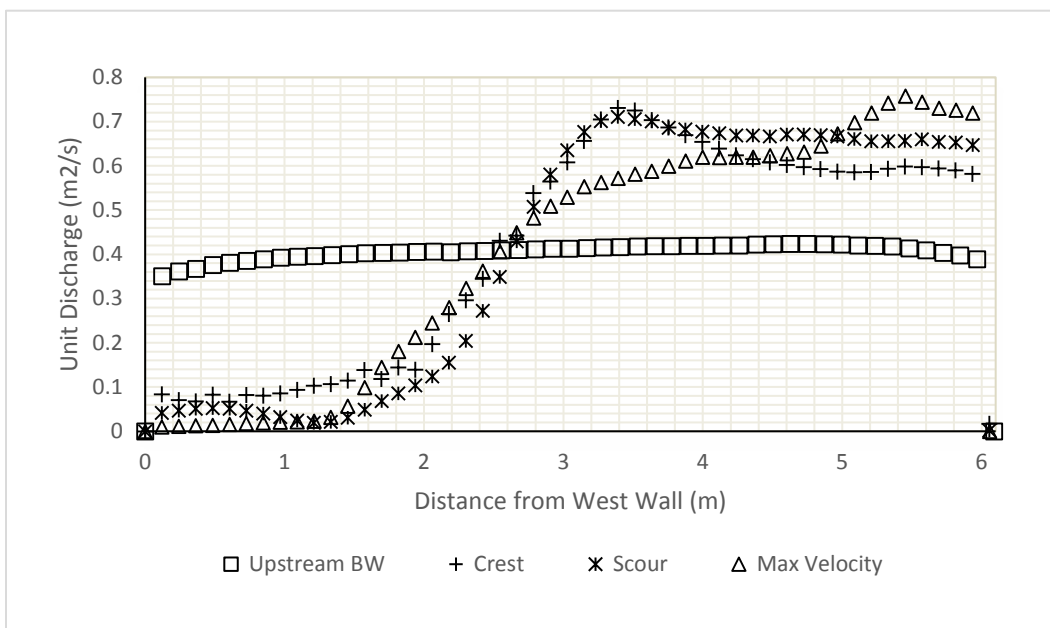


(b)

Fig. 76. Unit discharge distribution when $Y/H = 2.0$ and $\alpha = 60^\circ$ along the four cross-sections indicated in Fig. 55: (a) pre-scour; and; (b) post-scour

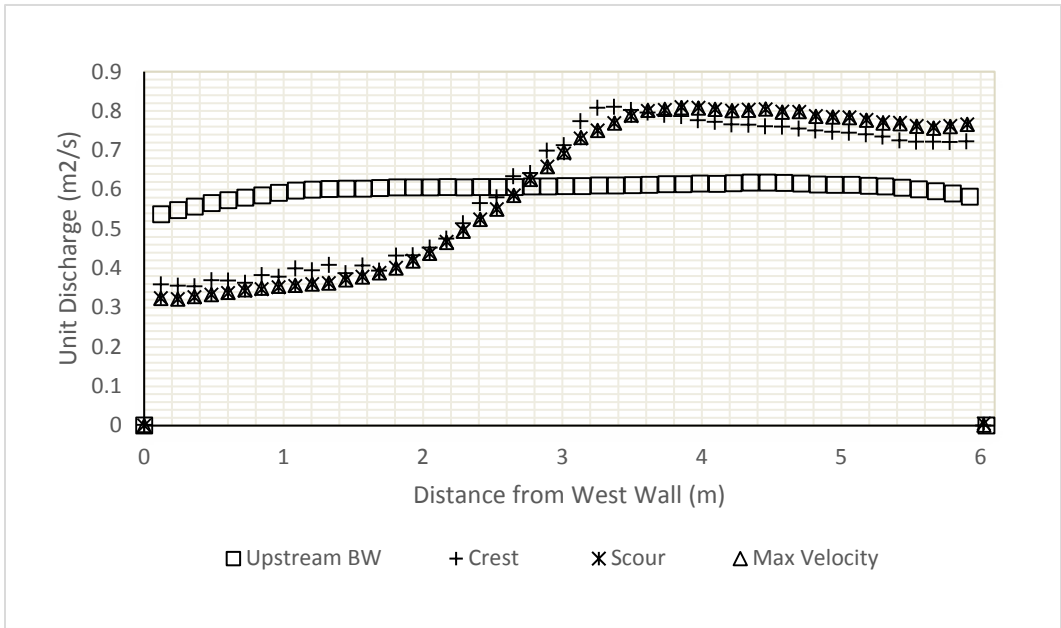


(a)



(b)

Fig. 77. Unit discharge distribution when $Y/H = 1.25$ and $\alpha = 90^\circ$ along the four cross-sections indicated in Fig. 61: (a) pre-scour; and; (b) post-scour



(a)



(b)

Fig. 78. Unit discharge distribution when $Y/H = 2.0$ and $\alpha = 90^\circ$ along the four cross-sections indicated in Fig. 61: (a) pre-scour; and; (b) post-scour